Low-dose CT Protocols for Accurate Proton Therapy Treatment Planning

Masoud Elhamiasl

KU Leuven
Biomedical Sciences Group
Faculty of Medicine
Department of Imaging and Pathology
Devision of Nuclear Medicine

KU LEUVEN
DOCTORAL SCHOOL
BIOMEDICAL SCIENCES

Low-Dose CT Protocols for Accurate Proton Therapy Treatment Planning

Masoud Elhamiasl

Dissertation presented in partial fulfilment of the requirements for the degree of Doctor in Biomedical Sciences

Examination committee:

Supervisor:	Prof. Dr. Johan Nuyts
Co-supervisors:	Prof. Dr. Edmond Sterpin Prof. Dr. Xavier Geets
Chair (examining committee):	Prof. Dr. Ronny Bruffaerts
Chair (public defence):	Prof. Dr. Koen Van Laere
Jury members:	Prof. Dr. Hilde Bosmans Prof. Dr. Jan D'hooge Prof. Dr. Dirk De Ruysscher Prof. Dr. Christian Richter Dr. Sébastien Brousmiche

April 2023

KU Leuven
Groep Biomedische Wetenschappen
Faculteit Geneeskunde
Departement Beeldvorming en Pathologie
Nucleaire Geneeskunde en Moleculaire Beeldvorming

KU LEUVEN
DOCTORAL SCHOOL
BIOMEDICAL SCIENCES

Lage Dosis CT-protocollen voor Nauwkeurige Planning van Protontherapie

Masoud Elhamiasl

Proefschrift voorgedragen
tot het behalen van de
graad van Doctor in de
Biomedische Wetenschappen

Jury:

Promotor:	Prof. Dr. Johan Nuyts
Copromotoren:	Prof. Dr. Edmond Sterpin Prof. Dr. Xavier Geets
Voorzitter leescommissie:	Prof. Dr. Ronny Bruffaerts
Voorzitter openbare verdediging:	Prof. Dr. Koen Van Laere
Juryleden:	Prof. Dr. Hilde Bosmans Prof. Dr. Jan D'hooge Prof. Dr. Dirk De Ruysscher Prof. Dr. Christian Richter Dr. Sébastien Brousmiche

April 2023

Perfection is achieved, not when there is nothing more to add,
but when there is nothing left to take away.

--- Antoine de Saint-Exupery

Acknowledgment

It's been a long road, but here I am at the end. Conducting this study and putting together this report was challenging yet fulfilling. Although this is presented as my work, I could not have completed it without the help of many people. I would like to take a moment to express my sincerest gratitude to all those who supported and helped me throughout this journey.

First and foremost, I would like to thank my supervisor, Prof. Johan Nuyts. Thank you, Johan, for all the support, patience, kindness, encouragement, and guidance you have provided me during my time here. I am truly grateful for the opportunities you have given me to challenge myself. Thank you for being a constant source of encouragement, for always being available to offer your expertise, for your thoughtful feedback and comments, for leaving no wall between us, and for your dedication to this project. I am confident that the lessons I have learned from you will serve me well in my future endeavors. Once again, I would like to express my sincerest gratitude for all that you have done for me.

I would like to extend my gratitude to my co-supervisors, Prof. Edmond Sterpin and Prof. Xavier Geets. Thank you, Edmond and Xavier, for designing this project, for continuously answering my questions, for your suggestions and feedback, and for sharing your expertise whenever I needed it. Johan, Edmond and Xavier, I would not have been able to achieve all the exciting works presented in this thesis without your supervision. I could not have asked for better supervisors than you. Your impact on my career will not be forgotten and I am honored to have had you as my supervisors.

I would like to express my sincere appreciation to the examination committee, Prof. Hilde Bosmans, Dr. Sébastien Brousmiche, Prof. Jan D'hooge, Prof. Dirk De Ruysscher, and Prof. Christian Richter, for taking the time to review my thesis and for insightful comments and hard questions. Your expertise and insights have been invaluable and have helped me immensely to take my thesis to the next level. Thank you Hilde for your continuous guidance and encouragement. I really enjoyed all the CT-related discussions I had with you and your wonderful team. Sébastien, thank you for looking at this project from another perspective and providing pragmatic solutions. Thank you, Christian, Dirk, and Jan, for the time dedicated to

critically reading my thesis. I would like to express my sincere appreciation to Prof. Koen Van Laere, the head of the Nuclear Medicine & Molecular Imaging Department, for chairing the public defense. Prof. Ronny Bruffaerts, thank you for chairing the reading committee.

My sincere thanks go out to all my teammates. Your help and support with my research, whether it was through sharing ideas, debugging codes or just being there to listen, have been immeasurable. I was lucky to have such smart colleagues and friends during my study. Ahmad and Georg, thank you for being supportive and caring and for sharing your knowledge whenever I needed it. Stack Overflow comes to my mind when I think about how you handle my questions. Ahmad, the day I arrived here on that warm humid day, you picked me up, showed me around, and invited me to your lovely home. You, Maryam, Daniel and Benjamin have been like family to me since day one. Georg, thank you for all the stimulating discussions, from AI to photography and champions league and also for your contribution to the CT denoising chapter. Esmaeel, thanks for being there for me whenever I needed a helping hand. Tao, thanks for walking me through CT images. Marina Vergara, thanks for all those hikes we did and board games we played. Frédéric, thanks for all the discussions we had, from CT imaging to Tour de France. Xikai, thanks for all those fun/sarcastic conversations. Rob, thanks for teaching me how to make ginger beer, one of my favorite drinks. Marina Filipovic, Amir, and Simon, it has been a couple of months since we started working together. Your company is great and I'm looking forward to working with you. Erwin, thanks for scarifying yourself to be my first Master student and for your contribution to the CT denoising chapter. To my teammates, thank you for being there for me in all my ups and downs. Your companionship have made this journey so much more enjoyable and memorable. You are a gem!

I could not have finished this project without the help of many outstanding collaborators. Dr. Walter Coudyzer, thank you for sparing your time whenever I turned to you and for contributing to data collection and image contouring. Dr. Koen Salvo, thank you for guiding me through proton therapy and your wonderful ideas and comment on low-dose CT project. Dr. Kenneth Poels, thank you for always being available to answer my questions. Pieter Populaire, thank you for your thoughtful comments and your contribution to the TV delineation. Dr. Gilles Defraene, thank you for the insights and data you shared with me. Vlad Mihai Badiu, thank you for teaching me how to work with RayStation and for helping me to define proton treatment plans. Dr. Laurence Delombaerde and Dr. Siri Willems, thank you for contributing to the OARs contouring section. Prof. Maarten Lambrecht, thank you and your team, especially Dylan Callens, for helping me with patient selection. I would also like to thank the participating patients and their families, as well as all the staff members of the Department of Radiation Oncology for facilitating data

collection. Prof. Frederic Noo and Dr. Karl Stierstorfer, I appreciate your prompt replies to my CT-related questions. Wies Deckers, Tim Van Deyck, and Bram Mangelschots, thank you for all the technical support.

To my fellow colleagues at the department of Nuclear Medicine: Caro, Chungmeng, Donatienne, Greet, Hannes, Jenny, June, Martijn, Michel, Nathalie, Niloufar, you are all pure joy. To my labmates at the Louvre (MIRC): Ahmed, Alexis, Ewout, Hasti, Jeroen, Kobe, Marcus, Maarten, Mihnea, Mahdi, Sofie, Somayeh, Sophie, and so many more who made me feel so welcome. Thank you all for your friendship and kindness, coffee and lunch breaks, time together, and short runs. I will always cherish the memories we made together.

I am very thankful to Fonds Baillet Latour and KU Leuven for financially supporting this project. Also many thanks to Francine Reniers and Peter Vermaelen for their assistance in the administrative work.

During my PhD, I have had the great fortune to meet many outstanding people. I would like to thank NSS/MIC, ESTRO, CT Meeting, and Fully 3D communities and MIRO and AMPHORA teams. I am grateful to meet many of you during my journey and have learned a lot from you.

Lastly, but perhaps most importantly, my loving family. Maman va Baba, thank you for your unconditional love and support and for your contributions to my education and my life in numerous amounts of ways. Thank you for always being there when I needed someone the most. You mean so much to me. To Mina and Amir, the best partners in crime, for always making me laugh when I was feeling down and making me smile when I was feeling sad. My parents-in-law for their understanding and support. Gholamreza, Amir, Somayeh, and Aysal, thank you for being such a source of kindness. I would also like to acknowledge my grandparent, Ata, who passed away before the completion of my education. I know he would be proud.

My warmest thanks and sincerest gratitude belongs to my best friend, my colleague, and the love of my life, Masoomeh. Thank you for being a shoulder to lean on, for being there for me when I needed a listening ear, for being a helping hand when I needed it most, and for supporting me no matter what. Sharing an office and being able to discuss our works made this experience so much more enjoyable and memorable. Thank you for being my rock and for making this journey truly unforgettable. You mean so much to me and I am so grateful to have you by my side because we make each other better people.

My sincere thanks to all my friends that I have met in Leuven, particularly the Iranian community, for their moral support. I started writing my thesis while many brave people in Iran and Afghanistan were paying the ultimate price for gender equality and social reforms. I owe a debt of gratitude to all those who have been fighting for “woman, life, freedom”.

Masoud

Summary

Proton therapy is an advanced form of external beam radiotherapy that utilizes high-energy proton beams to destroy cancer cells. Proton beams can target tumors precisely while minimizing damage to surrounding healthy tissues. Proton plans are more sensitive than photon plans to anatomical variations over the course of treatment. Range uncertainties due to anatomical variations can be minimized by employing an imaging feedback loop, first, to detect these changes and then to adapt the plan to the patient's new geometry. In fact, the full potential of proton therapy can be exploited by adapting the treatment plan which requires a new computed tomography (CT) acquisition at the beginning of each treatment session. The treatment typically involves several tens of treatment sessions. Performing a new CT image at every treatment session results in an additional accumulated patient dose.

Reducing CT imaging radiation dose is desirable, in particular for pediatric cases (due to the higher sensitivity to ionizing radiation) and also for cases where 4DCT is required to account for breathing motion. However, lowering the CT imaging dose results in a noisier image which may deteriorate its diagnostic and therapeutic value. We hypothesized that the signal-to-noise ratio provided by conventional CT protocols is higher than needed for proton therapy applications. In this thesis, we aim to explore the effect of CT imaging dose reduction on different tasks in proton therapy to determine the lowest possible radiation dose that still produces sufficient clinical information.

To explore the possibility of using low-dose CT (LdCT) for different tasks in proton therapy, a LdCT simulator is developed and validated to generate realistic LdCTs by adding an appropriate amount of position-dependent and correlated noise to the standard-dose CT image. The dose reduction is modeled, first, by estimating the noise equivalent number of photons in the high-dose scan and then applying a thinning technique (random elimination of some of the photons) to reduce that number. The proposed model accounts for the quantum and electronic system noise, for the bowtie filter, for the correlation (crosstalk) between detector elements, for the beam hardening effect, and for the non-linear smoothing filter in very low-dose scans.

Several phantom studies with different acquisition protocols on different CT scanners demonstrate the accuracy of the proposed model in providing realistic LdCT. In each test, the texture and magnitude of the simulated noise are compared with the measurements in the image and sinogram domains. Experimental results show a close agreement between the simulated LdCTs and the measured LdCT, where the relative error on the standard deviation of simulated noise is in the order of 1% and 3% for the sequential and helical scans, respectively. In addition, the noise power spectra of the simulated noise matches the measurements.

LdCT simulation with a gradual reduction (by a factor of up to 10) in imaging dose enables us to explore the effect of CT imaging dose reduction on different tasks in proton therapy, including dose calculation, plan optimization, and delineation of target volumes and organs at risk (OAR). In total, one phantom study and twenty patient studies (mainly 4DCT of esophageal and lung cancer patients) are conducted to assess the effect of reducing CT imaging dose. Each test starts from a standard-dose CT image where the results based on this reference CT image will be considered as ground truth. Then noise is added to the CT scan to emulate the effect of CT dose reduction, and the same test is repeated for the simulated LdCTs. Comparing the results based on LdCTs with those of the standard-dose scan will quantify the effect of CT dose reduction.

Experimental results show that the doses calculated on the LdCT are in close agreement with those calculated based on the standard-dose CT, with the Gamma passing rate (3%/1 mm) of close to 100%. In addition, the plans optimized based on the LdCT are clinically equivalent to those optimized on the standard-dose CT, with the Gamma passing rate (3%/1 mm) of above 90% for the majority of the cases.

LdCTs are also evaluated for the delineation of target volumes and OARs. The anatomical structures are first delineated on the LdCTs and then compared with those based on the standard-dose CTs. Experimental results show a strong overlap between the contours based on the low-dose and standard-dose CTs where the error is smaller than inter-observer variability. However, a lower feeling of certainty was reported for the manual delineation of target volumes on the LdCT. In addition, the higher level of CT noise on LdCTs makes the delineation of the brachial plexus more challenging.

A higher level of noise on LdCTs might hinder the process of plan adaptation, especially when human intervention is needed. This problem can be addressed by employing a LdCT denoiser to suppress CT noise on LdCTs. A CNN based on the ResUNet architecture is developed and trained to denoise LdCTs. The training is performed using standard-dose and simulated LdCT pairs. The denoised LdCTs are then used for proton therapy treatment planning. The doses and plans based on the denoised images slightly

outperform those based on the noisy LdCTs. In addition, the overlap between contours is higher in the majority of cases when the noisy LdCTs are replaced with denoised images.

To sum up, the results show that CT imaging dose reduction by up to 90% did not have a notable impact on proton therapy dose calculation and plan optimization as well as target volumes and OARs delineation. The results based on LdCT are in close agreement with those based on the standard-dose image. However, less dose reduction is expected to be achievable in cases that require the delineation of the brachial plexus.

Beknopte samenvatting

Protontherapie is een geavanceerde vorm van uitwendige bestraling waarbij gebruik wordt gemaakt van hoogenergetische protonenstralen om kankercellen te vernietigen. Protonenbundels kunnen tumoren precies treffen terwijl de schade aan omliggende gezonde weefsels wordt geminimaliseerd. Protontherapie is gevoeliger dan fotontherapie voor anatomische variaties in de loop van de behandeling. Bereikonzekerheden als gevolg van anatomische variaties kunnen worden geminimaliseerd door beeldvorming te gebruiken om deze veranderingen te detecteren en dan het plan aan te passen aan de nieuwe geometrie van de patiënt. Met zulke aanpassingen kan het volledige potentieel van protontherapie worden benut, maar daarvoor is wel een nieuwe computertomografie (CT)-opname vereist aan het begin van elke behandelsessie. De behandeling omvat doorgaans enkele tientallen behandelsessies. De opname van een CT-beeld bij elke sessie resulteert in een extra geaccumuleerde patiëntdosis.

Het is wenselijk om de stralingsdosis van CT-beeldvorming te verlagen, in het bijzonder voor pediatrische gevallen (vanwege de hogere gevoeligheid voor ioniserende straling) en voor gevallen waarin 4DCT nodig is om rekening te houden met de ademhalingsbeweging. Het verlagen van de CT-dosis resulteert echter in een beeld met meer ruis, waardoor de diagnostische en therapeutische waarde ervan kan verminderen. Onze hypothese was dat de signaal-ruisverhouding van conventionele CT-protocollen hoger is dan nodig is voor toepassing in protontherapie. In dit proefschrift onderzochten we het effect van CT-dosisreductie op verschillende taken in protontherapie om de laagst mogelijke stralingsdosis te bepalen die nog steeds voldoende klinische informatie oplevert.

Om de mogelijkheden van lage dosis CT (LdCT) te onderzoeken voor verschillende taken in protontherapie, is een LdCT-simulator ontwikkeld en gevalideerd. De simulator kan realistische LdCT's te genereren door een geschikte hoeveelheid positieafhankelijke en gecorreleerde ruis toe te voegen aan het standaarddosis CT-beeld. De dosisreductie wordt eerst gemodelleerd door het ruis-equivalent aantal fotonen in de scan met hoge dosis te schatten en vervolgens een verdunningstechniek (willekeurige eliminatie van fotonen) toe te passen om dat aantal te verminderen. Het voorgestelde model verklaart

de kwantum- en elektronische systeemruis, het bowtie-filter, de correlatie (overspraak) tussen detectorelementen, het bundelverhardingseffect en het niet-lineaire afvlakfilter in scans met een zeer lage dosis.

Fantoomstudies met verschillende acquisitieprotocollen op verschillende CT-scanners tonen de nauwkeurigheid aan van het voorgestelde model voor de simulatie van realistische LdCT. Bij elke test werden de textuur en omvang van de gesimuleerde ruis vergeleken met die van echte metingen in het beeld- en sinogramdomein. De experimentele resultaten laten een nauwe overeenkomst zien tussen de gesimuleerde LdCT's en de gemeten LdCT, waarbij de relatieve fout op de standaarddeviatie van gesimuleerde ruis in de orde van 1% en 3% ligt, voor respectievelijk sequentiële CT en spiraal-CT. Bovendien komen de ruisvermogensspectra van de gesimuleerde ruis goed overeen met die van de metingen.

LdCT-simulatie met een geleidelijke verlaging (tot een factor 10) van de beelddosis stelt ons in staat om het effect van CT-dosisreductie op verschillende taken in protontherapie te onderzoeken, waaronder dosisberekening, planoptimalisatie en afbakening van doelvolumes en organen-in-gevaar (OAR). In totaal werden één fantoomstudie en twintig patiëntenstudies (voornamelijk 4DCT van patiënten met slokdarm- en longkanker) uitgevoerd om het effect te beoordelen van het verlagen van de CT-dosis. Elke test begint met een standaarddosis CT-beeld waarbij de resultaten op basis van dit referentie-CT-beeld als grondwaarheid worden beschouwd. Vervolgens wordt ruis toegevoegd aan de CT-scan om het effect van CT-dosisreductie na te bootsen, en dezelfde test wordt herhaald voor de gesimuleerde LdCT's. Door de resultaten op basis van LdCT's te vergelijken met die van de standaarddosisscan, kan het effect van CT-dosisverlaging worden gekwantificeerd.

Experimentele resultaten laten zien dat de doses berekend op de LdCT nauw overeenkomen met die berekend op basis van de standaarddosis CT, met een Gamma-passing rate (3%/1 mm) van bijna 100%. Bovendien zijn de plannen die zijn geoptimaliseerd op basis van de LdCT klinisch equivalent aan de plannen die zijn geoptimaliseerd op de standaarddosis-CT, met een Gamma-passing rate (3%/1 mm) van meer dan 90% voor de meeste gevallen.

LdCT's werden ook geëvalueerd voor de afbakening van doelvolumes en OAR's. De anatomische structuren worden eerst afgebakend op de LdCT's en vervolgens vergeleken met die op basis van de standaarddosis-CT's. Experimentele resultaten laten een sterke overlap zien tussen de contouren op basis van de CT's met lage dosis en standaarddosis, waarbij de fout kleiner is dan de variabiliteit tussen waarnemers. Er werd echter een lager gevoel van zekerheid gerapporteerd voor de handmatige afbakening van doelvolumes op de LdCT. Bovendien maakt het hogere niveau van CT-ruis op LdCT's de afbakening van de plexus brachialis uitdagender.

Een hoger ruisniveau op LdCT's kan het proces van planaanpassing belemmeren, vooral wanneer menselijk ingrijpen nodig is. Dit probleem kan mogelijk worden verholpen door de ruis op LdCT's te onderdrukken. Een CNN (convolutioneel neuraal netwerk) op basis van de ResUNet-architectuur werd daarvoor ontwikkeld en getraind. De training werd uitgevoerd met telkens een gesimuleerd LdCT-beeld als input en een standaarddosis-CT-beeld als referentie. De van ruis ontdane LdCT's werden vervolgens gebruikt voor de planning van de protontherapie. De doses en plannen op basis van de beelden met ruis-onderdrukking presteren iets beter dan die op basis van de LdCT's. Bovendien is de overlap tussen contouren in de meeste gevallen groter wanneer de LdCT's werden verwerkt met het CNN.

Samenvattend laten de resultaten zien dat CT-dosisreductie tot 90% geen noemenswaardige invloed had op de dosisberekening en planoptimalisatie in protontherapie, en evenmin op de definitie van doelvolumes en afbakening van OAR's. De resultaten op basis van LdCT komen goed overeen met die op basis van het standaarddosisbeeld. Er wordt echter verwacht dat minder dosisverlaging haalbaar is in gevallen waarbij de afbakening van de plexus brachialis vereist is.

List of Abbreviations

3D Three-dimensional.

4D Four-dimensional.

4DCT Four-dimensional computed tomography.

ADMIRE Advanced modeled iterative reconstruction.

AEC Automatic exposure control.

CBCT Cone-beam computed tomography.

CNN Convolutional neural network.

CT Computed tomography.

CTV Clinical target volume.

DD Dose-difference.

DECT Dual energy computed tomography.

DSC Dice similarity coefficient.

DTA Distance-to-agreement.

DVH Dose-volume histogram.

FBP Filtered backprojection.

GPR Gamma passing rate.

HD Hausdorff distance.

HU Hounsfield unit.

iCTV Internal clinical target volume.

IMPT Intensity-modulated proton therapy.

IMRT Intensity-modulated radiation therapy.

Ld2Hd Low-dose to high-dose.

Ld2Ld Low-dose to low-dose.

LdCT Low-dose computed tomography.

MAE Mean absolute error.

MLTR Maximum likelihood algorithm for transmission tomography.

MRI Magnetic resonance imaging.

MSE Mean square error.

NCD Noncommunicable disease.

NPS Noise power spectrum.

OAR Organ at risk.

PBS Pencil beam scanning.

PSNR Peak signal-to-noise ratio.

PTV Planning target volume.

SDF Signal-dependent filter.

SOBP Spread-out Bragg peak.

SPR Stopping-power ratio.

SSIM Structural similarity index measure.

TPS Treatment planning system.

WET Water equivalent thickness.

Table of Contents

List of Figures

List of Tables

1 General introduction

Cancer is one of the leading causes of premature death worldwide. Globally, cancer alone was responsible for about 29.8% of premature deaths from Non-Communicable Diseases (NCDs) in 2016 [1]. Unfortunately, there is a continuing rise in cancer incidence and mortality worldwide. Cancer has been overtaking cardiovascular diseases as the predominant cause of mortality from NCDs [2]. In 2021, there were estimated to be over 4 million cancer cases and 1.9 million cancer deaths in Europe [3]. Compared to 2020, the number of new cancer cases is estimated to increase 21% by 2040 in EU and EFTA countries [4], placing massive emotional and financial pressure on individuals and healthcare systems [5]. Recent studies have indicated that the United Nations' target to reduce a third of premature death from NCDs (including cancer) over 15 years is feasible through early diagnostics and the use of more advanced treatment techniques [2].

Cancer therapy is the process of killing or removing cancer cells while minimizing damage to healthy tissues. Surgery, chemotherapy, radiation therapy, and immunotherapy are the major therapeutic approaches for cancer treatment. The type of treatment depends on many factors such as the type of cancer, the location of the tumor, and its stage. In fact, cancer therapy is a multi-modality approach, meaning that more than one modality of treatment is usually involved during treatment. For example, surgery followed by radiation therapy to destroy residual tumor cells has shown to be beneficial for many brain tumors [6].

1.1 External radiotherapy

External beam radiotherapy is a non-invasive approach that utilizes high-energy ionizing radiation from outside of the patient to destroy cancer cells. It kills cancer cells or keeps them from dividing by damaging their DNA. It is estimated that approximately 50% of all cancer patients receive radiation therapy during their treatment [7, 8, 9]. Ionizing radiation deposits its energy in the cells of the tissues it passes through, resulting in damage to the normal cells along with cancer cells. The main goal of radiation therapy is to deposit a maximum amount of dose in the tumor, while minimizing the damage to surrounding healthy tissues.

High-energy photons from a linear accelerator is the most common form of radiation treatment used in cancer treatment. The photon depth-dose distribution profile (Figure 1.1) shows that the photons deposit their maximum dose close to the entrance surface. After a short build-up region, the dose decreases exponentially with increasing depth in the tissue. Therefore, multiple field directions must be used to ensure a homogeneous coverage of the tumor while sparing surrounding Organs At Risk (OARs). For example, Intensity-Modulated Radiation Therapy (IMRT) [10, 11] can be employed to deliver higher doses of radiotherapy to tumor tissues while minimizing the damage to the critical surrounding structures. Nevertheless, healthy tissues are still exposed to low radiation doses, increasing the risk of radiation-induced malignancies [12, 13, 14].

A conformal dose distribution can also be achieved by employing charged particles. In contrast to photons, charged particles deposit a peak of energy close to the end of their path, over a very small volume known as the Bragg Peak. Figure 1.1 compares the relative depth-dose curves for photon and proton. The Bragg peak of a single proton is sharp and its location depends on the incident energy of the protons.

It is possible to deliver a homogeneous dose over the entire tumor volume by combining multiple proton beams with slightly different energies, known as the Spread Out Bragg Peak (SOBP), as shown in Figure 1.1. An advanced dose sculpting with the added benefit of a low plateau dose before and no exit dose after the Bragg peak makes the proton an attractive particle for cancer therapy, especially for tumors in proximity to dose-sensitive organs and pediatric cases with a higher risk of secondary cancer.

1.2 Proton therapy

Proton therapy was first introduced by R. Wilson [16] in 1946 but was limited to research laboratories until the 1990s. Subsequently, clinical proton therapy has been growing steadily. According to the Particle Therapy Co-Operative

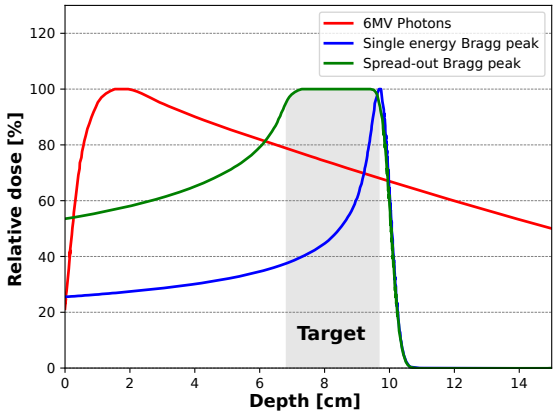

Figure 1.1: Illustration of relative depth-dose curves for photon and proton in water. Figure based on [15].

Group (PTCOG) report, over 280,000 patients have received proton therapy worldwide in more than 120 centers (with 36 others under construction) [17].

Proton therapy can deliver a large amount of energy to cancer tissues with fewer doses deposited in surrounding healthy tissues. As compared with any form of photon therapy, the total amount of energy deposited by proton beams in the patient, also called integral dose, is at least a factor of three lower [18]. This makes proton beams an interesting particle, especially for children or patients with long-expected overall survival.

Discussion about the pros and cons of proton versus photon treatments goes beyond the scope of this study. Briefly, the proton beams can deliver more conformal doses to the tumor and spare surrounding healthy tissues more effectively. However, the higher cost of proton therapy systems and lack of comparative effectiveness data make it controversial [19]. Furthermore, proton beams are very sensitive to range uncertainty (uncertainty in the exact position of Bragg peaks in the patient) due to the sharp gradient of the Bragg peak. For example, the motion of the tumor inside the body of the patient has a small impact on the dose distribution in photon treatments. In contrast, in proton therapy, a small motion of the tumor or density changes in the beam path can lead to substantial dose distortions. This is because even relatively small changes in the trajectory of the protons through the body can have an important effect on the position of the Bragg peak.

Even though protons offer a better dose sculpting, the variation in patient setup and anatomy can adversely affect target volume coverage and OAR sparing. In proton therapy, there are several sources of range uncertainties. Range uncertainties could be due to volumetric imaging system (relative

stopping power calibration), dose calculation (nuclear interactions and Coulomb scattering), treatment delivery (proton energy variations), and patient anatomy (rigid or deformable patient changes) [20, 21]. There are numerous studies exploring the possible strategies to mitigate range uncertainties. For example, a wide variety of immobilization devices can be used for fast and reproducible setup of the patient, minimizing inter- and intra-fractional variation [22, 23, 24]. Stoichiometric calibrations [25, 26] or Dual Energy Computed Tomography (DECT) imaging [27, 28, 29] have been suggested to minimize systematic range uncertainties from Computed Tomography (CT) imaging system. Robust optimization [30, 31, 32, 33] can be employed to mitigate setup and range errors. Robust optimization considers different scenarios during the plan optimization, to assure target coverage and OAR sparing in presence of setup errors, however, it cannot account for all the uncertainties.

In proton therapy, a significant (often dominant) source of range uncertainty is anatomical changes through the course of treatment [34, 35]. It is due to the fact that proton therapy treatments are defined based on a single image set that is acquired days or weeks before treatment, assuming that the patient's anatomy remains constant during the course of treatment. In addition, the total radiation dose is split up into several tens of smaller fractions over the course of treatment, from several days to weeks [36], to exploit the higher repair capacity of normal tissue compared to tumor cells. Anatomical changes frequently occur between fractions, consequently, the delivered dose distorts from what was originally planned. Such anatomical changes can significantly compromise the physical advantage of proton beams.

Applying an appropriate margin around the target volume is an accepted practice to account for most uncertainties and to ensure coverage of the target volume. However, it increases the dose to the surrounding healthy tissues. In addition, some anatomical changes are not considered in the planning target volume because they are not predictable. Some of these changes are treatment-related such as tumor shrinkage or growth or patient's weight loss, some are unrelated to radiation such as variation in rectal, bladder, bowel, or nasal cavity filling [21]. Additionally, breathing, heartbeat, or intestinal motion (which can not be avoided) can cause intra-fractional anatomical changes during one fraction.

The effect of inter- and intra-fractional anatomical variations should be considered in the treatment plan. For example, the beam direction must be carefully selected to mitigate the effects of anatomical changes [15]. However, even anatomically robust optimization might be insufficient to account for some of these anatomical changes completely [37, 31, 38, 21]. A better solution to mitigate the effect of anatomical changes can be achieved by plan adaptation. Adaptive radiation therapy is intended to detect changes in patient anatomy

and adapt the treatment plan when necessary. In fact, the full potential of proton therapy can only be exploited in combination with adaptive strategies.

1.3 Adaptive proton therapy

Adaptive proton therapy aims to deliver radiation dose accurately in the presence of anatomical changes by employing a closed-loop imaging system to systematically monitor these changes and tailor the treatment plan to the "geometry of the day" [39]. It is applied to account for inter-fractional anatomical changes during the course of fractionated treatment delivery. Cases that exhibit large inter-fractional variations are most likely to benefit from adaptation [21].

The ultimate goal of adaptive proton therapy is to re-optimize the treatment plan based on the image on the day [21]. Adaptation is especially critical in proton therapy where small anatomical changes can lead to significant dose perturbations due to the dose conformality and finite range of proton beams [21]. A comparison of IMRT and Intensity-Modulated Proton Therapy (IMPT) plans revealed that more than 60% of non-small cell lung cancer (NSCLC) patients needed plan adaptation when treated with protons, while no patients required adaptation when treated with photons [40].

Figure 1.2 (left) shows an example of proton therapy workflow [15]. After the first consultation, appropriate volumetric images are acquired. The volumetric images are used to determine the prescribed dose to the target(s) and to delineate anatomical structures such as Clinical Target Volume (CTVs) and OARs. Once the anatomical structures and field directions have been specified, the objectives and constraints should be defined for target volumes and OARs. A treatment planning system should then be employed to minimize the objective function while obeying the constraints. Proton therapy dose calculation and plan optimization are typically based on the planning CT image. The planned dose distribution will then be discussed and modified to select the plan with the most appropriate trade-offs between different planning goals. Once the optimization process is complete, the plan can be evaluated by assessing the fulfillment of clinical goals. Finally, physical quality assurance tests are performed to ensure that the plan can be delivered as expected [15].

For plan adaptation, a similar workflow will be followed. Figure 1.2 (right) represents the workflow when adaptation is required. The process starts with performing a new volumetric image (so-called image-of-the-day). The anatomical structures can then be propagated from the planning CT (which requires image registration) or re-defined on the new image (which typically requires auto-contouring software). The plan is then reoptimized, followed by assessing the clinical and physical quality of the new, adapted plan [15]. An

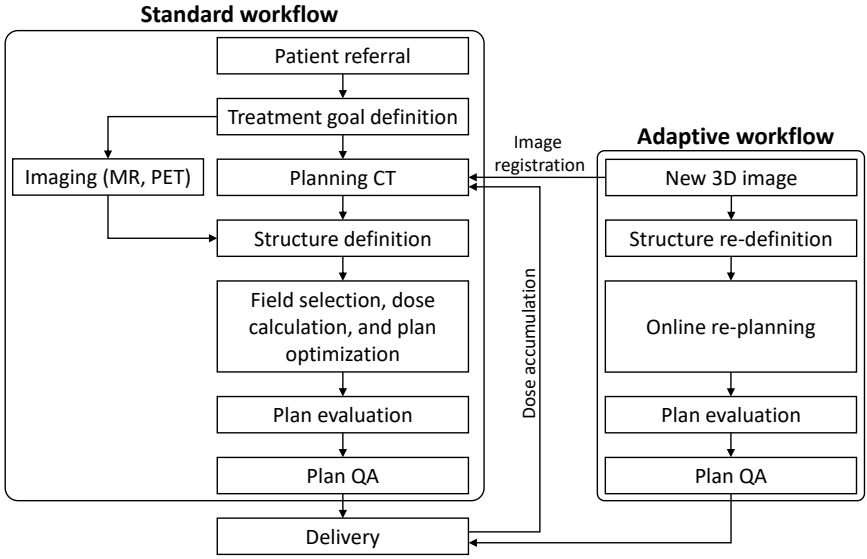

Figure 1.2: Schematic overview of the standard (left) and adaptive (right) proton therapy workflows. The treatment goal and prescribed dose usually remain unchanged during the treatment. Figure based on [15] and [41].

accurate dose accumulation technique is also needed to keep track of the total dose to the target volume and OARs.

Adaptation can be performed on-line or off-line. In current clinical practices, off-line adaptation is used when covering the target or sparing the OAR is not possible (due to anatomical changes). In this case, a new image is acquired and the plan is optimized based on it. Due to the massive workload associated with adaptation, there may be a gap up to several days between the time the new image is acquired and the time the modified plan is applied. Off-line adaptation is especially beneficial for gradual changes, such as weight loss or tumor shrinkage, and cannot act on random variation.

For random anatomical changes, such as rectal, bladder, or nasal cavity filling, the plan-of-the-day concept can be applied [42]. It requires the acquisition of several planning images, taken on different days with different anatomical conditions. The appropriate plan should be then defined and approved for each image. Each treatment starts with the acquisition of a new image to select the best matching plan. The plan-of-the-day concept is much faster, however, it imposes even a higher workload and cannot account for unexpected variations.

On-line adaptation (automated) can be employed to account for any

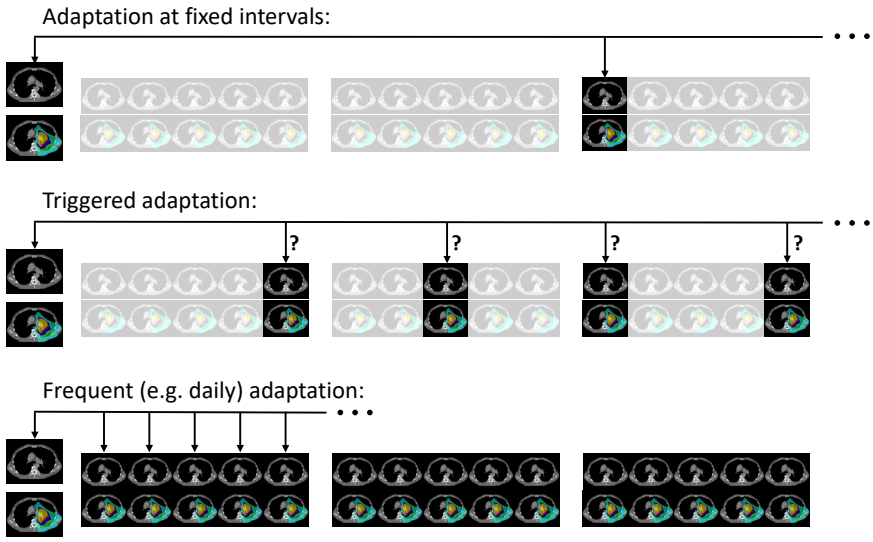

Figure 1.3: Representation of possible adaptive proton therapy strategies including: adaptation at constant intervals (first row), adaptation triggered by on-line imaging (second row), and adaptation on a daily basis (third row). Figure based on [21] and [43].

anatomical changes. On-line adaptation aims to ensure accurate positioning of the patient with respect to the beam and also a faithful reproduction of the planned dose distribution. However, employing quick on-line re-planning tools is necessary and automation is inevitable as time is the main bottleneck in implementing adaptive workflows. On-line adaptive strategies have already been introduced in commercial photon therapy systems (MR-linacs and Ethos systems).

There is no consensus on the appropriate frequency of adaptation. Figure 1.3 shows some common examples of adaptation techniques. When tumor shrinkage is expected, adaptation at constant intervals (often halfway through the treatment) is commonly used [21]. Triggered adaptation modifies the plan by observing the anatomical changes on a given treatment day (often weekly imaging) and reacting to them if a certain anatomical threshold is reached. Replanning can be triggered by weight loss, changes in surface contour or mask fit, changes in OAR and CTV volume, or systematic deviations in setup [44, 43]. The ideal scenario is daily adaptive proton therapy, possibly accompanied by a trigger adaptation, however, it requires significant labor and computational resources [43].

The implementation of adaptive proton therapy in the clinical workflow is in its infancy, and several obstacles need to be overcome. A new image acquisition, structure re-definition, plan evaluation, plan adaptation, and plan verification are involved in plan adaptation [21]. On-line adaptation has to be completed within minutes, posing extra challenges due to time limitations, especially if human intervention is required for the manual modification of target volumes and OARs and other verification processes [45]. For this reason, automation may be necessary in order to accelerate the plan adaptation process [46]. Nonetheless, the first and most crucial component of the adaptation is the acquisition of a new volumetric image at every treatment session.

1.4 Imaging modalities

In the adaptive proton therapy process, a new volumetric image acquisition is required to evaluate the original plan based on the geometry of the day and to adjust the treatment plan if necessary. Proton therapy relies on precise knowledge of tissue characteristics to accurately predict the proton Stopping-Power Ratio (SPR) and thereby dose deposition. Stopping power is used in treatment planning to calculate the dose distribution and proton range. The selection of the correct imaging modality plays an important role in treatment quality. These repeated images are acquired regularly, therefore, employing the correct modality is crucial for cost, time, and resource management. In-room CT, Cone-Beam Computed Tomography (CBCT), and Magnetic Resonance Imaging (MRI) are the main imaging modalities that can be employed for plan adaptation. Each of these imaging modalities has its costs and benefits.

In current clinical practice, single-energy X-ray CT is the most common and reliable imaging modality for estimating proton stopping powers. Proton therapy facilities are usually equipped with either CT or CBCT as the daily imaging system [21]. Compared to CBCT, in-room CT scanners offer better Hounsfield Unit (HU) accuracy, image contrast, and 4DCT capabilities. In-room CT provides Three-Dimensional (3D) images with similar quality to those of the planning CT images which makes it the most practical modality for adaptive proton therapy application [47]. CT-on-rail in combination with a robotic patient positioner enables patient imaging on the treatment bed, within the treatment room. CT-on-rails are diagnostic CT scanners that are mounted on rails to move in the axial direction relative to the patient. However, the treatment couch must be moved between the in-room CT imaging system and the treatment area (by a robotic patient positioner), increasing the risk of the patient moving before the treatment [48].

DECT can provide more accurate stopping power calculations. This is because tissues with different compositions can have different stopping powers

but the same HU for a particular kVp. DECT acquires two CT scans with different X-ray spectra so that more information can be obtained about the tissues compositions. Proton range uncertainty can be decreased from 3% for single-energy X-ray CT to 2% by deploying DECT [29]. DECT also offers better image quality, improves the delineation of target volume and OARs, enables virtual subtraction of contrast agent, etc [28, 49]. Although DECT has potential benefits, its implementation in clinical practice is still at an early stage, mainly due to the lack of practical hardware and software solutions [28].

CBCT is commonly used in current clinical practices for the positioning of the patient. Even though CBCT offers imaging at the treatment position, it suffers from reduced field-of-view and inaccurate estimates of HU number. Therefore, it cannot be used for proton dose calculation and plan reoptimization. Considerable effort is being made to allow CBCT for dose calculation by correcting HU in CBCT, however, it is still a research topic [50, 51, 52].

MRI imaging has gained interest in proton therapy in recent years, particularly due to higher soft tissue contrast and a dose-free imaging technique. However, extensive magnetic shielding is required to minimize interference between the electromagnetic fields of the treatment system and the magnetic field of the MR scanner. In addition, estimating proton stopping power from an MRI is not trivial due to the fact that MR images are not (directly) correlated with the material density. The range uncertainty of the proton beam would increase if MR images were used for dose calculations. Translation of MRI images to synthetic CTs could be a possible way to use MR images for planning, but research still needs to be done [53, 54, 55, 56].

To sum up, in current clinical practice, proton therapy treatment planning is based on stopping power estimation from single-energy CT images. Performing a new CT acquisition in every treatment session results in an additional accumulated radiation dose to the patient. The radiation dose from imaging systems is one of the obstacles to implementing adaptive proton therapy in the clinical workflow.

1.5 Organ doses from CT scans

The use of CT has grown rapidly since its introduction in the 1970s. By nature, CT scans expose patients to high levels of X-rays, raising concerns about the potential lifetime radiation-related cancer risk. The radiation dose a patient receives from a CT scan varies significantly within and across institutions and depends on several factors: the number of scans, the product of tube current and scan time (the “mAs”), the patient size, the axial range, the scan pitch, the tube voltage (kVp), the scanner type, etc. The effective dose reported in previous studies varies significantly. The effective dose, as a

rough estimate, ranges from 2 mSv for a routine head CT scan to 31 mSv for a multiphase abdomen and pelvis CT scan [57]. Organ dose during a CT examination is around 10 mGy but can also be as much as 80 mGy for coronary angiography [58]. The cumulative effective dose can sometimes exceed 100 mSv for patients who undergo recurrent CT examinations [59, 60], resulting in significantly increased lifetime radiation risk.

Radiation-related cancer mortality is typically estimated to be 1 death for every 2000 scans, assuming an effective dose of 10 mSv per scan [61]. Therefore, CT acquisition protocols should always be tailored to the individual examination type to practice the "As Low As Reasonably Achievable (ALARA)" principle and to mitigate the hazards associated with radiation.

Minimizing the ionizing radiation doses from the imaging system is crucial to reduce the risk of radiation-induced malignancies [62]. This is particularly relevant for children due to their higher radiosensitivity and longer life expectancy [63, 64, 58, 65, 66, 67, 68, 69] and for patients undergoing recurrent CT exams [59, 60, 70], such as patients who undergo adaptive proton therapy. It has been estimated that the lifetime cancer mortality risk associated with radiation exposure from an abdominal CT and a head CT examination in a 1-year-old child is approximately one in 550 and one in 1500, respectively, which is an order of magnitude higher than risks for adults [63]. Previous studies have reported a positive association between CT exposure during childhood and the risk of developing central nervous system (CNS) tumors and leukemia [65, 68, 71, 72]. Radiosensitivity declines with age for most cancers, however, there are some exceptions. For example, lung cancer risks associated with radiation increase with age (up to middle age) [58].

1.6 Radiation dose reduction in CT scanners

There are several components integrated into modern CT scanners that help minimize unnecessary radiation to the patient, as shown in Figure 1.4. The high X-ray energies pass through the patient's body while the low energies are usually absorbed or scattered. The low-energy filter is located between the X-ray tube and the patient to filter out the low-energy X-ray photons that cannot pass through the patient. The X-ray path length is typically shorter at the periphery of the body than in the central region. A bowtie filter (also known as the beam-shaping filter) is usually used to reduce exposure to the patient's periphery by shaping X-ray beam fluence [74]. The pre-patient collimator is placed between the X-ray tube and the patient to limit the X-ray beam coverage and avoid unnecessary radiation dose to the patient.

It is crucial to have an efficient detector in order to produce good-quality images. The efficiency of detectors can be quantified by their quantum

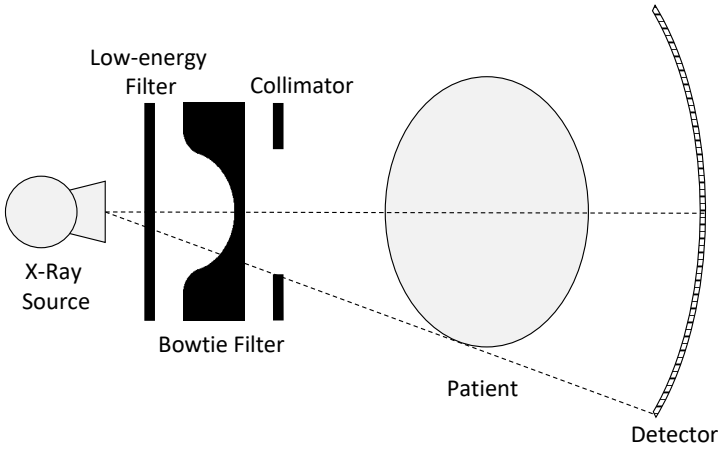

Figure 1.4: Schematic drawing of a simple CT system with angle-dependent X-ray beam intensities. Figure based on [73].

detection efficiency and geometrical efficiency [75]. Electronic noise can also significantly degrade image quality, particularly if a Low-dose CT (LdCT) is performed. Employing efficient detectors such as photon counting detectors [76] can eliminate electronic noise, improving image quality for LdCT protocols.

Automatic exposure control (AEC) [77] aims to automatically modulate the x-ray tube current to account for differences in attenuation due to patient anatomy, shape, and size. The tube current can be modulated depending on the projection angle (angular modulation) and longitudinal location along the patient (z-modulation) [75]. In addition, advanced image reconstruction techniques in combination with lowering the tube load can be employed to reduce radiation dose.

The most effective strategy to reduce radiation-related cancer risk can be achieved by optimizing CT acquisition protocols and by avoiding unnecessary CT examinations. Optimizing CT acquisition protocols is a challenging task. There is a trade-off between CT noise and the desire to lower radiation doses. A reduction in imaging dose results in a reduction in image quality.

1.7 Summary

A diagnostic-quality CT scan directly before each treatment session would be paramount in order to exploit the full potential of proton therapy. Even though the dose from a CT is small compared to the therapeutic radiation, the total

dose associated with the series of these CTs can be significant [78], especially for pediatric cases or if a Four-Dimensional (4D) CT is acquired to account for breathing effects. This contradicts the ultimate goal of proton therapy which is minimizing the unnecessary dose to healthy tissues. This problem can be addressed by performing a LdCT. Reducing CT dose is always desirable, however, lowering the radiation dose results in a lower signal-to-noise ratio and therefore in a reduced image quality which may deteriorate the diagnostic and therapeutic value of CT images.

In this thesis we aim to investigate the effect of reducing CT imaging dose on different tasks for proton therapy treatment planning. By doing so, it is possible to determine the lowest radiation dose that provides sufficient information for proton therapy treatment planning. The objectives and the outline of this thesis are described in the next chapter.

2 Research objectives

The research conducted during this PhD sought to investigate the effect of CT imaging dose reduction on proton therapy treatment planning. The ultimate goal is to determine the lowest possible CT radiation dose that still produces sufficient information for proton therapy treatment planning.

We hypothesize that the signal-to-noise ratio provided by conventional CT protocols is higher than needed for several tasks in proton therapy and there is room for CT imaging dose reduction. The requirements for proton therapy planning are different from those for conventional diagnostic CT imaging. For example, typically a voxel size of around 3 mm is used for proton dose calculation, which indicates that the resolution of standard CT imaging protocols (usually 0.6 to 1 mm) is higher than needed.

To verify our hypothesis and enable a patient-dependent CT imaging dose reduction, a CT dose reduction simulation tool was developed and validated to simulate LdCT scans from an existing standard-dose scan (also knows as reference or high-dose CT). This tool produces a virtual lower-dose scan by adding the appropriate amount of a position-dependent and correlated noise to the standard-dose scan. Details of this tool will be discussed in Chapter 3. The primary goal of Chapter 3 is to extend the currently available standard-dose CT scans dataset, to generate the standard-dose and low-dose CT pairs that will be used in subsequent chapters.

Simulating the corresponding realistic LdCT with a gradual reduction in imaging dose enables us to explore the effect of CT imaging dose reduction on different tasks in proton therapy treatment planning such as proton therapy

dose calculation and plan optimization, and also the delineation of target volume and organs at risk. Comparing the results based on LdCT with those of the standard-dose scan can quantify the effect of reducing CT dose on proton therapy treatment planning.

Chapter 4 discusses the effect of reducing CT imaging dose on proton therapy dose calculation, plan optimization, and water equivalent thickness estimation. The simulated LdCTs are used for dose calculation and plan optimization and the results are compared quantitatively with those of the ground truth, acquired from the standard-dose CT image. Integrating SPRs along the beam path is a fundamental element in proton therapy dose calculation. SPRs are (indirectly) derived from CT images. There are negative noise correlations between neighboring pixels in CT images. Therefore, the noise is expected to partly cancels out by integrating them along beams. Consequently, a strong CT dose reduction is expected to be acceptable for dose calculation and plan optimization. The effect of CT noise on the delineation of target volumes and OARs (image contouring) is not included in this chapter. Thus, this chapter is highly relevant to dose restoration approaches [79, 80, 81] in which repeated CTs are used to adapt a plan without the need for contour adjustment.

It is particularly imperative to reduce CT dose if a 4DCT is required for plan adaptation. With 4DCT, the effective dose could be four to ten times higher than with 3DCT [82, 83]. Chapter 5 discusses the effect of reducing CT dose on proton therapy treatment planning for esophageal and lung cases where a 4DCT image is needed to account for breathing motion. The effect of CT noise on the delineation of target volumes and OARs, along with the effect on dose calculation and plan optimization, is discussed in this chapter. Noise in LdCT makes manual delineation more demanding, therefore, less aggressive dose reduction is expected if the CT images are used for the manual segmentation of anatomical structures.

Human intervention is currently inevitable in the process of plan adaptation. The higher amount of noise in the LdCT might hinder the performance of the human operator. To address this problem, a Convolutional Neural Network-based (CNN) LdCT denoiser is developed and trained to denoise LdCTs. Training of CNN models requires high-quality (clean) CT images as the reference data (label) and the corresponding LdCTs (noisy) as the training samples. The lack of high-quality training data pairs is the main bottleneck in the training of CNN-based methods. The simulated LdCTs, along with standard-dose images, provide us with a valuable database that allows us to develop and train a CNN-based model to suppress CT noise. The training sample can be generated by simulating LdCTs from high-dose CT scans and then the training can be carried out using the standard-dose and low-dose training

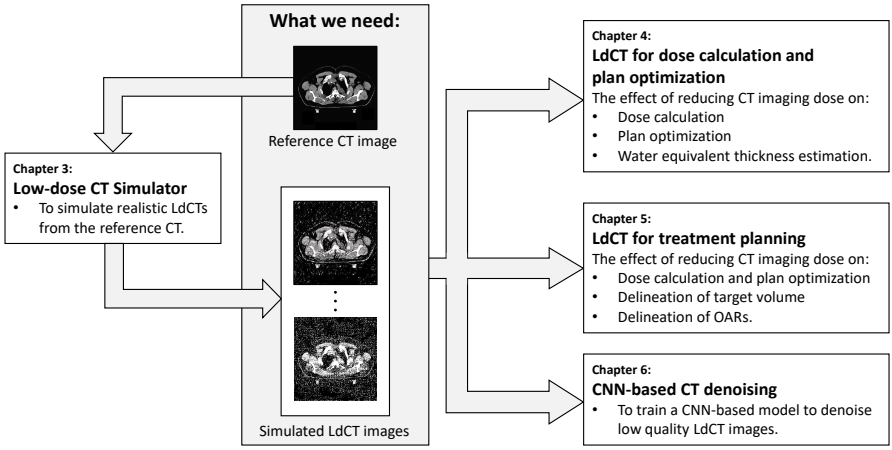

Figure 2.1: Schematic of the research framework and thesis outline.

pairs. Detailed descriptions of the network architecture, training process, and validation of the CNN-based CT denoiser are described in Chapter 6.

2.1 Overview

This thesis is composed primarily of articles which have been published or are in preparation for submission. Figure 2.1 represents the design of this Thesis.

Chapter 3 presents LdCT simulation based on the CT scans acquired on Siemens SOMATOM Force scanner and has been published in Physics in Medicine and Biology. The LdCT simulator was successfully calibrated on the Siemens SOMATOM Drive and Definition Edge scanners that are in use at the radiation oncology department of the University Hospital of Leuven. The results have partially appeared in a conference proceeding for the International Conference on Image Formation in X-Ray Computed Tomography (CT Meeting 2020).

In Chapter 4 results are presented on the study into the effect of CT noise on proton dose calculation and plan optimization, and have been published in Physics in Medicine and Biology. The results based on phantom studies were published in two conference proceedings for the International Conference on Image Formation in X-Ray Computed Tomography (CT Meeting 2020) and the IEEE Nuclear Science Symposium and Medical Imaging Conference (NSS/MIC 2021).

Chapter 5 discusses the effect of CT imaging dose reduction on proton therapy treatment planning (including dose calculation, plan optimization, and

image delineation) based on the 4D planning CT of esophageal and lung cancer patients that were treated at our center. This chapter is in preparation for submission.

In Chapter 6, a CNN-based LdCT denoiser has been developed, trained, and validated to denoise LdCT images. The denoised images are then used for proton therapy dose calculation, plan optimization, and delineation of OARs in order to investigate the feasibility of using CT denoisers to improve the results based on the (noisy) LdCT images. The preliminary results were published in a conference proceeding for the IEEE Nuclear Science Symposium and Medical Imaging Conference (NSS/MIC 2022). This chapter is also in preparation for submission.

In Chapter 7 the findings of the thesis are discussed and future prospects are presented.

3

Low-dose X-ray CT simulation from an available higher-dose scan

Masoud Elhamiasl, Johan Nuyts. Published in *Physics in Medicine & Biology*, vol. 65, no. 13, p. 135010, 2020.

Abstract

In CT imaging an optimal compromise between the radiation burden and the image quality for the imaging task is needed. Lower-dose CT is desirable, however, lowering the dose results in a lower signal-to-noise ratio and therefore in a reduced image quality. In this research, we aim to develop a tool to simulate lower-dose scans from an existing standard-dose scan. The main application of this tool is to determine the lowest possible radiation dose that still produces sufficient clinical information. The X-ray tube current reduction is modeled by estimating the noise equivalent number of photons in the high exposure scan and applying a thinning technique to reduce that number. The proposed method accounts for the bowtie filter, for the electronic system noise, for the noise correlation between neighboring detector elements, for the beam hardening effect, and for the non-linear smoothing filter in very low-dose scans. Several phantom studies with different acquisition protocols were performed to evaluate the accuracy of the proposed framework. The results demonstrate a close agreement between the noise

magnitude and texture of the measured and the simulated lower-dose scans. For instance, the standard deviation of noise in the simulation of lower-dose scans with 90% tube current reduction matches the reconstructions from the real scans with less than 1% and 3% error for sequential and helical scans, respectively. The noise texture was also assessed by analyzing the noise power spectrum of the simulated lower-dose images which matches those from the real scans. Furthermore, the relation between the measured and predicted noise in projection domain is very close to the line of identity which confirms the accuracy of the model.

3.1 Introduction

Computed Tomography (CT) is one of the most commonly used imaging modalities for diagnosis, treatment planning, and patient follow-up. The number of CT examinations is still increasing due to excellent soft tissue resolution (contrast), high spatial resolution, and short acquisition duration. However, there are some concerns regarding the risks associated with ionizing radiation exposure to the patients. Various measures have been taken to keep the dose as low as reasonably achievable (ALARA). Furthermore, modern CT scanners have been equipped with different components to minimize unnecessary radiation to the patient including bowtie filter, automatic exposure control (AEC), and also raw data preprocessing and advanced reconstruction algorithms in combination with lowering the tube current.

Low-dose CT (LdCT) scans can be achieved by reducing the radiation exposure to the patient, i.e. by lowering the X-ray tube current. However, there is a compromise between the radiation burden and the image quality in the imaging task. Lowering the radiation results in a lower signal-to-noise ratio and therefore in a poorer image quality. The most common way to determine the lowest possible radiation dose in CT protocols is clinical evaluation by physicians [84, 85, 86, 87, 88]. One method is to perform repeated scans with different radiation levels on the same patient and select the lowest exposure scan with minimum acceptable information. This strategy, however, is not ethical due to multiple exposures of the patient or should be done on phantoms instead where its clinical relevance is less. A more sophisticated strategy is to develop a tool to simulate reduced-dose scans from an existing high exposure scan and determine the lowest exposure scan which still provides sufficient information for the clinical task.

Dose reduction simulation techniques can be classified into two categories: those based on reconstructed CT images and those based on projection data. The methods of both categories simulate the lower dose scans by adding a proper synthetic noise to the higher-dose scan. The first approaches add noise in image space without the usage of the transmission data [89, 90, 91, 92].

These approaches are especially effective when the raw projection data are not available. However, nonlocal noise properties in reconstructed CT images [93] make it very difficult to simulate noise directly in the image domain. In the absence of raw projection data, an alternative way can be to generate a virtual sinogram from a high dose CT image [94, 95] and model dose reduction in the sinogram domain.

The methods of the second category simulate LdCT scans by adding synthetic noise to the higher dose scan in the projection domain. Our method falls into the second category. The existence of appropriate noise models in projection space is the main advantage of this category. The methods of this category mainly use a monochromatic noise model and consider synthetic noise as a Poisson, normal, or combination of Poisson and normal distribution. A detailed analysis of the transmission signal statistics was proposed by Whiting [96, 97] and Nuyts [98].

Preliminary works on dose reduction simulation have been done by Mayo [99] and Frush [100] by adding random Gaussian noise to the high exposure projection data. However, the effect of electronic noise was ignored in their model. Shortly afterward, Amir [101] used projection data to estimate the variance of synthetic Gaussian noise and added the reconstructed noise to the high dose scan in image space. Previous studies have shown that the bowtie filter and tube current modulation are two components that significantly affect the noise characteristics of CT transmission data. Massoumzadeh [102, 93] and Yu [103] simulated the LdCT scan by including the effects of electronic noise, bowtie filter, and tube current modulation in the simulation. The electronic noise obeyed a zero-mean Gaussian distribution and the noise in the higher dose scan was included in their models. Zabic [104] used a realistic non-Gaussian electronic noise which was measured during no-X-ray scans on the real systems to improve the accuracy of the simulations in very low dose scans. This model also accounted for the fact that the high dose scan was already noisy. Zeng [105] investigated the relationship between the incident flux of low and high dose scans and proposed a simple tool for low dose simulation by considering the effect of both quantum and electronic noise. Wang [106, 107] proposed a model similar to Frush [100] for dual-energy CT data with the goal of simulating data with various tube voltages.

In the state-of-the-art approaches, the transmitted data is often considered as the combination of Poisson and normal distribution [105, 104, 108, 109, 110] which is a good approximation of CT transmitted data. Additionally, the noise was often considered to be spatially uncorrelated although the noise of neighboring detector channels is actually correlated due to crosstalk between detector elements [97, 76, 111]. It is worth noting that the noise propagation through the image reconstruction is

not the same for correlated and uncorrelated noise, therefore, this correlation should be included in the simulation procedure. The uncorrelated noise does not exhibit the correct noise texture and results in the underestimation of the real noise magnitude in LdCT scans [112]. Wang [112] assumed the noise to be spatially correlated where the correlation was introduced by convolving the uncorrelated white noise with a kernel. The injected correlated noise accounted for both quantum and electronic noise, as well as their spatial correlation.

In this research, we aim to develop and validate a dose reduction simulation tool to simulate LdCT scans from an existing standard-dose scan. The main motivation is to determine the lowest possible radiation dose that still produces sufficient information for proton therapy treatment planning. However, this paper focuses on the issue of low dose CT simulation with a first evaluation based on the noise characteristics. Its application in proton therapy is ongoing research and will be reported on in future publications. The bowtie filter, the electrical noise, the crosstalk between detector channels, the beam hardening effect, and the non-linear smoothing filter in very low dose scans have been included in the proposed model. The proposed method employs the binomial distribution for thinning the high dose scan, which accounts for the fact that the higher exposure scan is already noisy. Most of the effects accounted for in our method have also been considered in previous publications, but to our knowledge, a method simulating all these effects was not previously proposed. In particular, many existing methods do not model the detector cross-talk and the non-linear smoothing filter. The preliminary results on a water phantom have been published at Fully3D 2019 conference [113].

The rest of this paper is organized as follows. A brief review of X-ray CT noise is presented in Section 3.2.1 and this section is followed by the proposed method for LdCT scan simulation. Experimental results are described and discussed in Section 3.3, and finally, some concluding remarks are drawn in Section 3.4.

3.2 Materials and Methods

Lower-dose CT scans can be modeled by adding a proper synthetic noise to a higher dose scan. In this section, the noise model of X-ray CT will be described and the effect of each CT scanner component on the noise model will be investigated in more detail. A new framework will then be developed to simulate lower-dose scans by estimating the noise equivalent number of photons in the higher exposure scan and applying a thinning technique to reduce that number.

3.2.1 Noise model

An X-ray tube produces polyenergetic X-rays, with a distribution of energies which depends on the applied tube potential and inherent filtration [97]. Additionally, at a fixed tube voltage, the number of X-ray photons emitted from an X-ray tube depends on the product of the tube current and the exposure time. In the rest of the paper we will refer to this product as the *tube load*. It has commonly been assumed that the incident X-ray intensity with the tube load α, $I_0^{(\alpha)}$, is linearly proportional to the tube load and its value depends on the tube current, the measurement duration time, and bowtie filter.

A CT scan is a set of measurements I_i, which are produced by photons passing through the patient body along a given ray path i, denoted by $l(i)$. Passing through the patient, the incident X-ray beam is attenuated by random absorption and scattering events. The I_i then enters the energy integrating detector and gets converted into an electronic signal. For polyenergetic X-rays generation, it is convenient to assume that $I_0^{(\alpha)}$ is grouped into discrete energy bins E_m, $m = 1, \cdots, M$, with probabilities λ_m. The values of λ_m spatially vary due to the effect of the bowtie filter and heel effect [114]. The mean number of surviving photons $\bar{I}_m$ of energy E_m arriving at the detector unabsorbed and unscattered can be described by Beer's law

$$\bar{I}_m = I_0 \lambda_m \exp\Big(- \int_{l(i)} \mu(x, E_m) dx \Big) \tag{3.1}$$

where $\mu(x, E_m)$ represents the energy-dependent attenuation map. In practice, the recorded value I_m is corrupted by many sources of variability and the real value of it is not available [98]. The noise produced in the detectors consists of quantum noise and electronic noise, and unless the attenuation along the path is extremely high, it is dominated by the former. The quantum noise is due to the limited number of X-ray photons detected by the detector and can be well modeled as a Poisson distribution. The detectors also add additional variability to the recorded signal, called electronic noise, due to fluctuations in the electronic components. The electronic noise is dominated by readout noise, which is independent of the exposure time, and we assume it obeys a normal distribution. In modern CT systems, the mean value of the electronic noise is measured before each scan in a short no-X-ray scan and the calculated mean is subtracted from the scan data. Consequently, the electronic noise can be modeled as a zero-mean normal distribution. The total number of photons of energy E_m that arrives at the detector can be written as

$$I_m = \mathcal{P}(\bar{I}_m) + \mathcal{N}(0, \sigma_e^2) \tag{3.2}$$

where $\mathcal{P}(a)$ denotes a realization of a Poisson distribution with mean a and $\mathcal{N}(0, \sigma^2)$ represents a realization of a zero-mean normal distribution with variance σ^2. This means that for a polychromatic X-ray generator, the CT transmission data I_i, observed in detector element i, can be modeled as a combination of a compound Poisson distribution and a normal distribution [97]. The contribution of each detected photon in the measured detector signal is proportional to its energy E_m. Consequently, we can assume that each detected signal is a realization of a random variable I_i whose statistics are described by

$$I_i = G_i \sum_{m=1}^{M} E_m \mathcal{P}\Big\{ I_{0i} \lambda_m e^{-\int_{l(i)} \mu(x, E_m) dx} \Big\} + \mathcal{N}\{0, \sigma_e^2\} \tag{3.3}$$

where G_i represents detector conversion factor [114]. The first term in Eq. 3.3 represents the effect of photon statistics, an energy-weighted combination of Poisson random variables which results in compound Poisson statistic [96, 115], and the second term represents the influence of the electronic noise.

Even though the proposed model in Eq. 3.3 can describe the polychromatic nature of X-ray generation, it is inconveniently complicated. To simplify Eq. 3.3, we can start by approximating a compound Poisson distribution as a (scaled) Poisson distribution which can be written as

$$I_i = \sum_{m=1}^{M} w_m I_m = \sum_{m=1}^{M} w_m \mathcal{P}(\bar{I}_m) \simeq \omega \mathcal{P}(\bar{I}_\omega) \tag{3.4}$$

where ω and $\bar{I}_\omega$ are fitting parameters. The quantity $\bar{I}_\omega$ can be regarded as the noise equivalent count of the original (compound Poisson distributed) signal [116]. The fitting parameters can be determined by requiring that the mean and variance of the Poisson distribution equal that of the compound Poisson distribution, which means

$$\sum_{m=1}^{M} w_m I_m = \omega \bar{I}_\omega \tag{3.5}$$

$$\sum_{m=1}^{M} w_m^2 I_m = \omega^2 \bar{I}_\omega \tag{3.6}$$

Note that if the tube load of the CT scanner is increased, all I_m increase by the same factor, and therefore $\bar{I}_\omega$ has to be increased by the same factor too. Thus, $\bar{I}_\omega$ is proportional to the tube load, and ω accounts for the weights introduced by the energy spectrum and the detector characteristics. Consequently, we can simplify Eq. 3.3 by approximating the compound Poisson distribution as a

simple Poisson distribution and use a monochromatic attenuation line integral. This approximation gives us

$$I_i \approx G_i \bar{E}_i \mathcal{P}\Big\{ I_{0i} e^{-\int_{l(i)} \mu(x,\bar{E})dx} \Big\} + \mathcal{N}\{0, \sigma_e^2\} \tag{3.7}$$

where $\bar{E}_i$ represents average energy. In addition, we can assume that this scaling factor, $G_i \bar{E}_i$, is the same for an air scan and a transmission scan. In the proposed method, the scaling factor vanishes since we always use the ratio of an air scan and a transmission scan. For simplicity, in the rest of the paper, we drop the subscript i, unless it is important to indicate it.

3.2.2 Quantifying the incident x-ray intensity

Dose reduction can be modeled by estimating the (noise equivalent) number of photons in the high exposure scan and applying a thinning technique to it. Assuming a monochromatic beam, the mean number of detected photons in the high dose scan of β mAs can be written as

$$I^{(\beta)} = \beta \; I_0^{(1)} \exp(-\rho) \tag{3.8}$$

where ρ denotes log-converted data. For the scanners considered in our project, the raw data contain log-converted data, $\rho = \ln(I_0/I)$. The log-converted raw data should first be converted into the form of transmission data using Eq. 3.8 which requires knowledge of $I_0^{(1)}$, a noise free estimate of the incident X-ray intensity for a unit tube load. At a fixed exposure time, the X-ray intensity is linearly proportional to the tube current which means $I_0^{(\alpha)} = \alpha I_0^{(1)}$ where α represents the tube current [117]. The variance of an air scan without any attenuating object can be used to estimate the incident X-ray intensity for every detector element. Modeling the transmission data as a combination of a Poisson and a normal distribution, the variance of the transmission data in an air scan is given by

$$\mathrm{var}\Big[\exp(-\rho_{air}^{(\alpha)})\Big] = \mathrm{var}\Big[\frac{I_{air}^{(\alpha)}}{I_0^{(\alpha)}}\Big] = \frac{\mathrm{var}[I_{air}^{(\alpha)}]}{(I_0^{(\alpha)})^2} = \frac{\alpha I_0^{(1)} + \sigma_e^2}{(\alpha I_0^{(1)})^2} \tag{3.9}$$

Performing some air scans at different levels of tube load, the system is overdetermined and $I_0^{(1)}$ and σ_e^2 can be estimated using a least square estimator. When the number of incident photons $\beta I_0^{(1)}$ is known, the number of surviving photons in the transmission scan can be estimated with Eq. 3.8.

3.2.3 Thinning technique

Knowing the number of surviving photons in a high-dose scan with tube load β mAs, our goal is to simulate a lower-dose scan of α mAs. A thinning technique can be applied on the surviving photons of the high-dose scan to produce a (more) noisy LdCT scan. Thinning means the random elimination of some of the detected photons with survival probability of α/β, where the chance of not being eliminated is the same for each photon. Thinning of a known number of counts n with survival probability p produces a binomial distribution $\mathcal{B}(n;p)$. Employing a binomial distribution for thinning accounts for the fact that the higher-dose scan is also noisy.

The thinning should be applied to the quantum noise and not on the electronic noise, but there is no easy way to separate the two contributions for a single, noisy measurement. Therefore, we apply the shifted Poisson approximation [118] to Eq. 3.2 as follows:

$$I_m = \mathcal{P}(\bar{I}_m) + \mathcal{N}(0, \sigma_e^2) \simeq \mathcal{P}(\bar{I}_m + \sigma_e^2) - \sigma_e^2 \tag{3.10}$$

where σ_e^2 is the mean electronic noise contribution (this is a known constant, unaffected by noise). Both distributions have the same mean and variance, they differ only in the higher order moments. With this approximation, the total noise (including both quantum and electronic noise) on the signal is expressed as an effective number of photons and becomes amenable for thinning. However, the thinning also reduces the contribution of the electronic noise, whereas in reality, the electronic noise contribution is independent of the tube load. Therefore, that contribution is restored by adding a (noisy) number of additional photons. After the thinning, the mean electronic noise is subtracted to restore the correct mean, as in Eq. 3.10. This leads to

$$I_{sim}^{(\alpha)} = \mathcal{B}\Big(\beta I_0^{(1)} \exp(-\rho) + \sigma_e^2, \frac{\alpha}{\beta}\Big) + \mathcal{P}\{(1 - \frac{\alpha}{\beta})\sigma_e^2\} - \sigma_e^2 \tag{3.11}$$

The first term reduces the number of photons observed in the converted raw transmission data, which itself is a random value because ρ is obtained from a measurement. The electronic noise is modeled as additional photons, which are also thinned. The second term adds a noisy number of photons to compensate for the thinning of the electronic noise. The last term subtracts the mean number of electronic noise photons, to ensure that the electronic noise has zero mean.

3.2.4 Noise correlation

So far, it is assumed that the noise contribution of any detector element is independent of that of the other detectors. Turning to the experimental evidence, we found that the noise of neighboring CT detector pixels is correlated with an almost fixed correlation matrix r which is due to crosstalk between detector pixels [97]. Considering that CT detectors are very small compared to the human body, we can assume that neighboring detectors i and j see the same intensity $\bar{A}$, such that their covariance can be written $C_{ij} = r_{ij}\bar{A}$, where r_{ij} is the noise correlation. The covariance between the detector pixels i and j is decreased to $\eta^2 C_{ij}$ after applying the thinning algorithm with survival probability of η. The problem is that in realistic data, the covariance should equal ηC_{ij}, not $\eta^2 C_{ij}$. This problem emerges due to the fact that during the thinning, we ignore the fact that neighboring detectors sometimes see the same photons. Since two independent thinning samples were generated from that single contribution, the correlation is suppressed.

It is important to restore this noise correlation in the lower-dose simulated scan because the noise propagation through the image reconstruction is not the same for correlated and uncorrelated noise. Therefore, we have to create an additional covariance of $(\eta - \eta^2)C_{ij}$, without changing the mean or the variance of the noise, and also without changing the correlations in the data, which should be correctly inherited from the original high count data.

The thinning noise N_i, defined as the difference between the signal after thinning and the signal before thinning scaled with η, is an uncorrelated zero-mean noise, satisfying

$$\mathrm{var}[N_i] = \eta\bar{A}(1-\eta) \tag{3.12}$$

which follows from the fact that thinning produces samples from a binomial distribution. Here, the idea is to convolve that thinning noise with a convolution mask w to restore the correlation between detector pixels. Convolving N_i with a convolution mask w generates the samples Q_i:

$$Q_i = \sum_j w_{i-j} N_j \qquad \forall_k \quad w_k = w_{-k} \;\; and \;\; w_k \geq 0 \tag{3.13}$$

The random variables Q_i have the following features:

$$\bar{Q}_i = \sum_j w_{i-j}\bar{N}_j = 0 \tag{3.14}$$

$$\begin{aligned}\mathrm{var}[Q_i] &= \mathbb{E}[Q_i^2] = \mathbb{E}\Big[\sum_j \sum_k w_{i-j} w_{i-k} N_j N_k\Big] \\ &= \sum_j w_{i-j}^2 \mathbb{E}[N_j^2] \\ &= \sum_j w_{i-j}^2 \mathrm{var}[N_j] \\ &= \eta \bar{A}(1-\eta) \sum_j w_j^2 \end{aligned} \tag{3.15}$$

$$\begin{aligned}\mathrm{cov}[Q_i, Q_j] &= \mathbb{E}[Q_i Q_j] = \mathbb{E}\Big[\sum_k w_{i-k} N_k \sum_{k'} w_{j-k'} N_{k'}\Big] \\ &= \sum_k \sum_{k'} w_{i-k} w_{j-k'} \mathbb{E}[N_k N_{k'}] \\ &= \sum_k w_{i-k} w_{j-k} \mathbb{E}[N_k^2] \\ &= \eta \bar{A}(1-\eta) \sum_k w_{i-k} w_{j-k} \\ &= \eta \bar{A}(1-\eta) \sum_\xi w_\xi w_{i-j-\xi} \\ &= \eta \bar{A}(1-\eta)[w \otimes w]_{i-j} \end{aligned} \tag{3.16}$$

where $\mathbb{E}[N_j N_{k\neq j}] = 0$ because the thinning noise is uncorrelated. The last equation is obtained by setting $\xi = k - i$ and using $w_{-\xi} = w_\xi$. It can be concluded that smoothing the thinning noise with mask w has no effect on the mean, scales the variance by a factor $\sum_j w_j^2$, and introduces a covariance which equals the convolution of the mask with itself and multiplied with the variance of the original thinning noise. Therefore, combining Eq. 3.12 and Eq. 3.16, the additional covariance created by convolving thinning noise with the convolution mask w should satisfy:

$$\eta \bar{A}(1-\eta)[w \otimes w]_{i-j} = (\eta - \eta^2) r_{ij} \bar{A}$$

Consequently,

$$[w \otimes w]_{i-j} = r_{ij} \tag{3.17}$$

The correlation matrix r can be obtained by performing a blank scan and estimating the correlation between neighboring detector pixels at a large number of locations (many independent noise realizations). The convolution in Eq. 3.17 can be then written as the multiplication of two circulant matrices and convolution mask w can be computed as the square root of matrix r.

3.2.5 Beam hardening effect

So far, the relation between beam intensity and the effective number of photons has been derived using blank scans. However, in patient scans, the photon beams reaching the detector are harder than in blank scans, because of the beam hardening effect. A harder beam contains fewer photons for the same intensity and is therefore subject to a higher amount of quantum noise [97].

In order to estimate the compensation ratio, two signals which produce the same beam intensity were generated. The first signal was decreased by water attenuation while the second signal was decreased by reducing the tube load. The beam hardening compensation ratio is given by the ratio of the variance of the signal reduced by the tube load to the variance of the signal reduced by water attenuation. Mathematically, it can be written as:

$$\text{Scaling Factor} = \frac{\sum_m S\ E_m^2\ I_m}{\sum_m E_m^2\ I_m\ \exp(-\mu_m l)} \tag{3.18}$$

where I_m is the beam intensity, E_m is the energy bin and, $\exp(-\mu_m l)$ represents water attenuation at energy E_m. The numerator and the denominator represent the variance of the signal reduced by the tube load and water attenuation, respectively. The parameter S was set to obtain the same intensity for both signals.

Knowing the attenuation value and bowtie thickness in each beam path (and therefore its effect on the energy spectrum), and assuming that all patient attenuation is due to water [108], the true value of the effective number of surviving photons can be predicted by multiplying the number of surviving photons in Eq. 3.8 by the scaling factor in Eq. 3.18. Fig. 3.1 represents the compensation ratio for different values of water and Teflon (bowtie) attenuation. It can be observed that the beam hardening effect is not negligible, for example, beam hardening by 20 cm of water produces 11 percent more variance than that of an air scan with the same intensity for an energy spectrum with 120 kVp, a tungsten anode, and typical filtering.

3.2.6 Signal dependent filter

The CT scanners are usually equipped with a preprocessing software, such as a low pass filter [103], to avoid negative values to be passed to the log when the detected signal is very small. In agreement with this, we observed that the noise level in very LdCT scans was less than predicted. Not knowing the vendor algorithm, we designed a Signal Dependent Filter (SDF) by requiring that, when the number of photons is below a particular threshold, the noise to signal ratio, NSR, no longer increases with decreasing number of photons. As

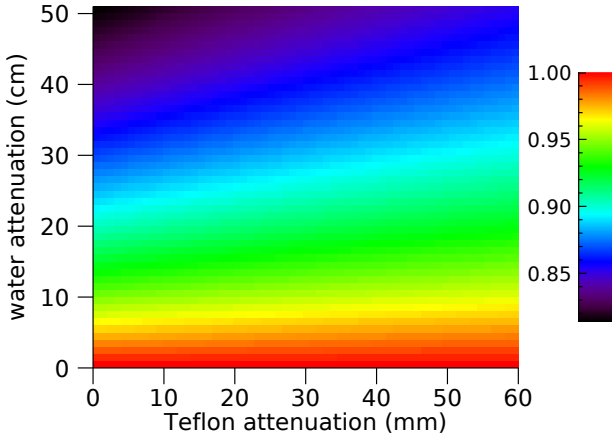

Figure 3.1: Representation of the ratio of the variance of the signal reduced by tube load to the variance of the signal reduced by water attenuation.

a consequence, the correlation between neighboring pixels increases when this filter is applied. The number of photons for which the filter must be activated was determined by analyzing the correlation between neighboring pixels.

The principle of the SDF is to smooth the detected signal by a simple 3×3 smoothing filter and mix the smoothed, $\bar{x}_i$, and the non-smoothed, x_i, signals according to the value of the smoothed signal. The combination of the smoothed and non-smoothed signal for the detector element i, $\tilde{x}_i$, can be described as follows

$$\begin{aligned}\tilde{x}_i &= (1-\tau)x_i + \frac{\tau}{n^2}\sum_{j=1}^{n^2} x_j \\ &= (1-\tau+\frac{\tau}{n^2})x_i + \frac{\tau}{n^2}\sum_{j=1,j\neq i}^{n^2} x_j = \sum_{j=1}^{n^2}\gamma_j x_j \end{aligned} \tag{3.19}$$

where x_i represents the detected signal in pixel i, j is the index of neighborhood pixels, n=3 is the size of the smoothing matrix, and τ determines the combination ratio of the smoothed and non-smoothed signals. Here, the aim is to estimate γ to keep the NSR at a specific level when the detected signal is smaller than the smoothing threshold, T. The NSR of the $\tilde{x}_i$ is given by

$$\mathrm{NSR} = \frac{\mathrm{var}[\tilde{x}_i]}{\mathbb{E}[\tilde{x}_i]^2} = \frac{\sum_{j=1}^{n^2}\gamma_j^2 x_j}{\left[\sum_{j=1}^{n^2}\gamma_j x_j\right]^2} \tag{3.20}$$

Algorithm 1 The procedure of lower-dose X-ray CT simulation.

Part 1: Parameter estimation
Perform blank scans at different tube loads.
Estimate the incident X-ray intensity, $I_0^{(1)}$, for each detector element and the variance of the electronic noise, σ_e^2.
Part 2: Lower-dose scan simulation
Perform a high-dose scan.
for each detector elements **do**
    Estimate the (noise equivalent) number of photons in high dose scan.
    Compensate the effect of beam hardening.
    Apply the thinning technique.
end for
Restore cross-talk correlation between neighboring detector elements.
Compensate for electronic noise reduction due to thinning.
Apply the SDF if the simulated signal is very small.
Convert simulated transmitted signals to logarithmic space.
Reconstruction.

When the detected signal is smaller than the smoothing threshold, the NSR of $\tilde{x}_i$ should be similar to that of when $x_i = T$. Using $\sum_j \gamma_j = 1$, it follows that

$$\sum_{j=1}^{n^2} \gamma_j^2 \approx \frac{\bar{x}_i}{T} \tag{3.21}$$

where $\bar{x}_i$ represents the signal smoothed by 3×3 averaging kernel. The corresponding value for τ is computed by combining Eq. 3.19 and Eq. 3.21. To sum up, the proposed framework estimates the equivalent number of photons in high dose scan and simulates the lower-dose scan by applying the thinning technique to that number. Subsequently, the simulated signal will be smoothed if it is smaller than the smoothing threshold.

So far, we described a model for sequential CT scans without AEC where the tube load remains the same in all views. However, the model can be extended to the clinical helical scans with AEC by comparing the tube current of high and low dose scan for every single view. The lower-dose CT simulation procedure is described in Algorithm 1.

3.3 Results

Several phantom studies were conducted to evaluate the performance of the proposed framework. In each experiment, a high-dose scan along with

Table 3.1: The description of phantom studies that were designed to evaluate the accuracy of the low-dose CT simulator. The scans were reconstructed with different reconstructions, including: MLTR (Maximum Likelihood algorithm for TRansmission tomography), FBP (Filtered BackProjection), and vendor software (ADMIRE: ADvanced Modeled Iterative REconstruction). ρ denotes the log-converted measurement value as defined in Eq. 3.8.

Phantom	Scan Mode	AEC	Reconstruction	ρ range
21cm water filled PMMA cylinder	sequential	No	MLTR	[-0.05, 4.51]
6cm water filled PMMA cylinder	sequential	No	MLTR	[-0.17, 1.12]
Anthro thorax phantom	sequential	No	FBP	[-0.16, 7.00]
Anthro thorax phantom	helical	Yes	FBP	[-0.43, 7.25]
Anthro abdomen phantom	sequential	No	MLTR	[-0.14, 8.40]
Anthro head phantom	helical	Yes	vendor (ADMIRE)	[-0.43, 7.07]

corresponding lower-dose scans were performed. The high-dose scan was used as an input to simulate the lower-dose scans according to the method given in section 3.2. The simulated scans were then reconstructed and compared with corresponding real lower-dose acquired scans. The noise power spectrum (NPS) and the standard deviations of the reconstructed image in uniform ROIs were used for the comparison. Scans with different acquisition protocols, including sequential and helical scans, scans with AEC, and in-house or vendor reconstructions, were used to evaluate the robustness of the proposed strategy against different acquisition protocols. Table 3.1 provides the details of each experiment and the range of raw data in logarithmic space for each phantom.

All the scans have been acquired on a Siemens SOMATOM Force. The tube voltage was set at 120 kVp in all experiments. At each view, the X-ray projection covers a 2-dimensional detector area containing 920×96 detector pixels. Each scan contained 4 different sets where each set corresponds to one of the four possible focal spot positions. This Siemens scanner uses so-called Flying Focal Spot (FFS) to increase the transaxial and axial sampling and therefore the resolution of the system [119, 120, 121]. The focal spot is moved forward and backward between two positions to increase the axial sampling (zFFS). For each of those positions, the focal spot is also moved from left to right to increase the transaxial sampling. Thus, the focal spot is moved to four different positions in four consecutive views and that affects the distance between the source and the detector. Since changing the distance between source and detector affects the photon flux, the four sets have been treated separately.

3.3.1 Parameter estimation

The incident X-ray intensity per unit tube load, $I_0^{(1)}$, and the variance of electronic noise, σ_e^2, are the parameters to be estimated. The first step is therefore performing some air CT scans at different levels of tube load to calculate $I_0^{(1)}$ and σ_e^2 according to the method given in section 3.2.2. A total of seven different tube current levels, from 300 mAs down to 20 mAs, with the exposure time of 1 second were used and at each level the scans were repeated 5 times to compute the variance of the transmitted data for each detector element at each tube load.

Turning to the experimental studies, we have noticed that some detector rows are occasionally off by some arbitrary offset while the other rows in the same view are fine, which induces additional noise correlations. This offset does not have any effect on image reconstruction (due to ramp filter), but it significantly affects the variance of transmission data in the blank scan. To suppress this noise correlation, it can be assumed that the mean value of the acquired blank scan in each row remains the same and the transmission data should be normalized accordingly. The detail on blank scans normalization can be found in Appendix B. This normalization results in a smaller variances on $\exp(-\rho)$ and therefore a larger $I_0^{(1)}$ as expected (see Eq. 3.9).

Fig. 3.2(a) is an image of the number of photons per mAs, $I_0^{(1)}$, for each individual detector pixel. It is an image of 920×96 pixels. The image reveals that the pixels are organized in 46×3 modules, each containing 20×32 detector elements. Fig. 3.2(b) represents the profile of $I_0^{(1)}$ and the variance of the electronic noise for one detector row. The bell shape profile of $I_0^{(1)}$ is due to the bowtie filter, which aims to reduce radiation dose to peripheral parts of the patient's cross-section, resulting in a non-uniform incident X-ray intensity. Because $I_0^{(1)}$ is determined for every detector element, the effect of the bowtie filter is automatically accounted for. It was assumed that the electronic noise was position independent with the same variance for all detector pixels. There are up to about 400 photons per unit mAs, the electronic noise is equivalent to 29 photons and the SDF threshold equals 160 photons. Fig. 3.2(c) illustrates the variance of the transmitted data for one detector row in the blank scan of 20 and 50 mAs and compares it with the fitted variance using estimated $I_0^{(1)}$ and σ_e^2.

3.3.2 Simulation validation

In order to investigate the effect of each component on the simulation of lower-dose scans, four different models have been developed. The first model, the simplest one, simulates the lower-dose scan by applying the thinning to the number of surviving photons in the higher-dose scan and ignores the effect

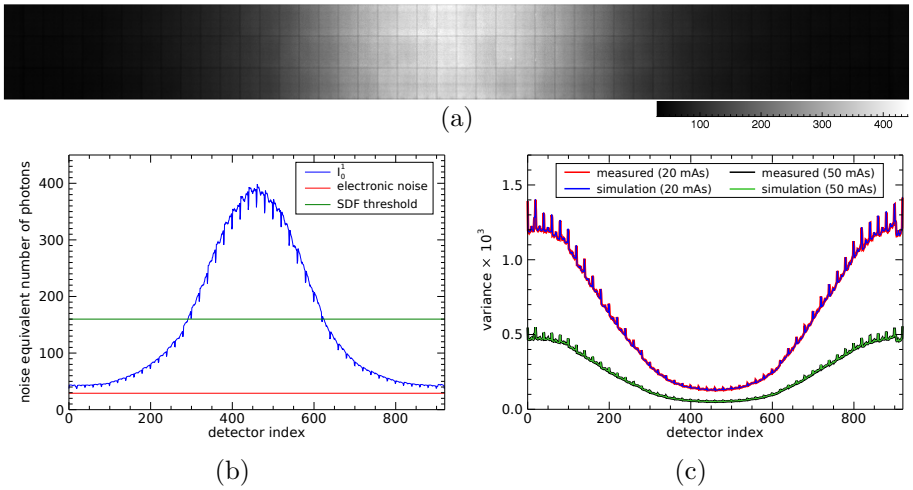

Figure 3.2: The illustration of the incident X-ray intensity per mAs (a) for all detector elements and (b) for a detector row (blue curve). The red and green lines in (b) show the variance of the electronic noise and the threshold where the SDF is applied for the Force scanner, respectively. (c) The comparison of the measured and the fitted variance of transmitted data in the blank scan of 20 and 50 mAs.

of beam hardening, the noise correlation and the SDF. Beam hardening has been included in the second model. The third model accounts for both beam hardening and noise correlation. The fourth model extends the third one by incorporating also the SDF.

In the first experiment, a water filled PMMA cylinder with diameter of 21 cm was scanned using sequential CT head-neck protocol. The lower-dose scans were simulated from a high-dose scan of 300 mAs and compared with corresponding acquired lower-dose scans. The scans were reconstructed using a maximum likelihood algorithm for transmission tomography (MLTR), applying 4 iterations and 25 subiterations [122] without applying any smoothing kernel. For a more detailed evaluation, the phantom was divided into central (C) and periphery (P) regions, represented in Fig. 3.5(a), and the standard deviation in each region was used for comparison. Fig. 3.3 compares the mean value of the noise standard deviation in the reconstructed images for each model at different levels of tube load. It is evident that decreasing the tube load increases the standard deviation in the reconstructed images. In addition, the standard deviation is not the same for center and periphery of phantom and the proposed model is able to track the noise levels for different regions.

For a better visualization, the standard deviation of the noise in each slice

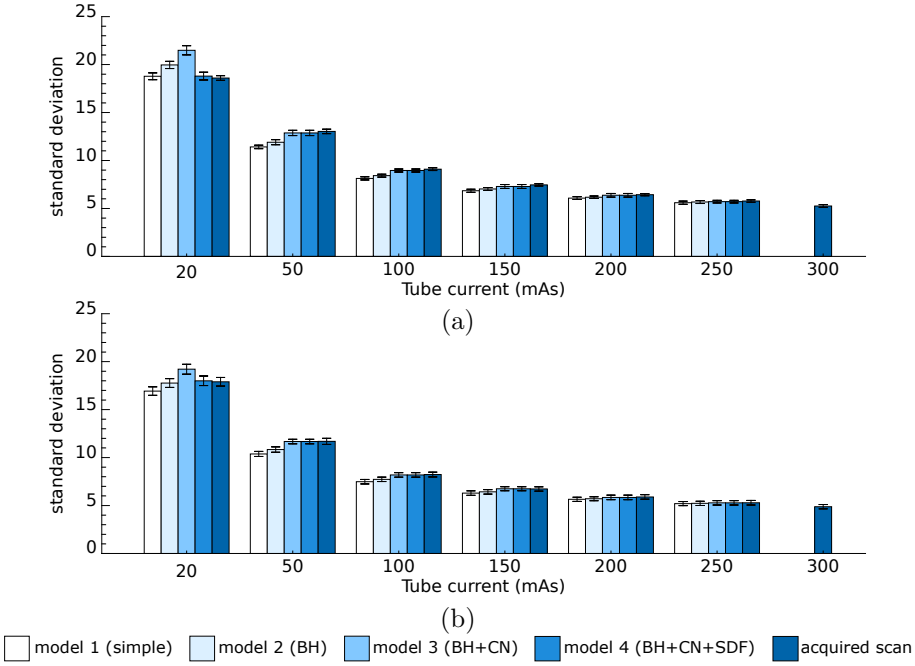

Figure 3.3: Representation of the standard deviation of the measured and the simulated images in the (a) center and (b) periphery of a 21 cm water phantom at different levels of tube current. The comparisons have been made between the models with different components, including beam hardening (BH), correlated noise (CN), and signal dependent filter (SDF). The error bars represent the variability of the noise in different slices.

was normalized by the mean value of the standard deviation in the corresponding acquired lower-dose scan. Fig. 3.4 represents the normalized noise standard deviation for different models. Considering a correlated noise model, in contrast to previous studies, has increased the standard deviation in image space while it did not have any effect on the noise standard deviation in projection data. In addition, incorporating the effect of beam hardening along with noise correlation brings the noise value of the simulated image closer to the real LdCT image, except for the 20 mAs scan. In this scan, the signal intensity was very small and therefore a SDF filter was applied by the system to suppress the noise level. Consequently, the standard deviation of lower-dose real scans is found to be less than predicted. This error is more in the center of the phantom, Fig. 3.4(a), because the detected signal tends to be smaller due to higher attenuation in the center of phantom.

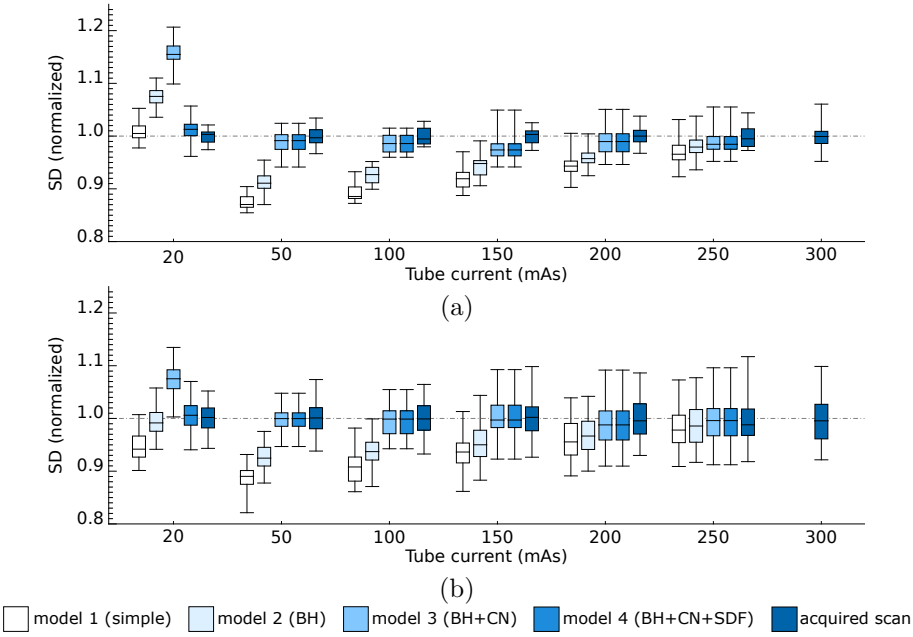

Figure 3.4: Comparison of noise level of reconstructed images in the (a) center and (b) periphery of a 21 cm water phantom at different levels of tube current. Incorporating the correlated noise (CN), beam hardening (BH), and signal dependent filter (SDF) brings the noise value of the simulated image closer to the real LdCT image. The error bars represent the variability of the noise in different slices.

However, when the SDF was included in the simulation, model 4 (final model), the reconstructed images of 20 mAs matches the reconstructions from the real data. Fig. 3.5 shows a high-dose scan of 300 mAs and its corresponding measured and simulated reduced-dose scans.

The noise texture in the reconstructed images was assessed by comparing the NPS in the real and simulated images. The NPS was computed by placing 13 squared ROIs of 51×51 voxel in the 20 slices. First, a 2D NPS was computed in the axial plane and then averaged over the planes. For better visualization, a 1D radially averaged profile of the 2D NPS was computed. Fig. 3.6 illustrates the NPS of simulated images and compares them with those of the real scans, confirming a strong agreement in the noise magnitude and texture between the measured and the simulated lower-dose scans.

As mentioned, the main limitation of model 3 arises when the number of detected photons is too small and a nonlinear smoothing filter is applied

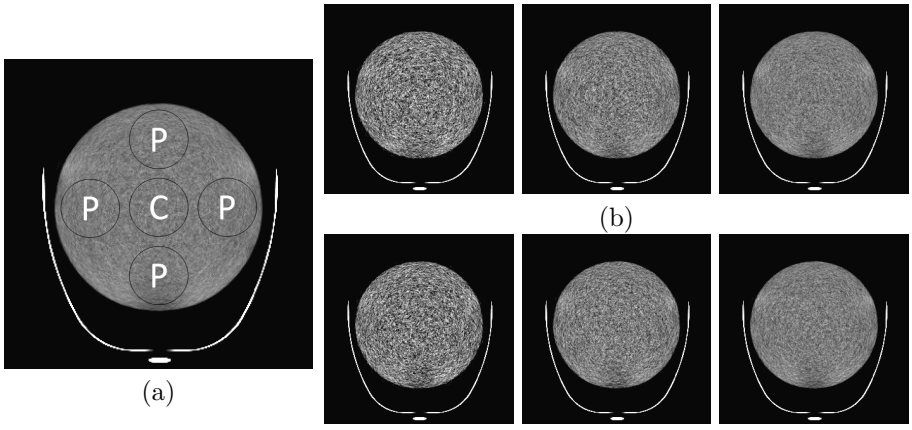

(a) (b) (c)

Figure 3.5: Presentation of (a) the measured high-dose image of 300 mAs, (b) corresponding acquired lower-dose images, and (c) simulated lower-dose images of 20, 50, and 100 mAs (from left to right) using the final model (window level: 0 HU, window width: 100 HU).

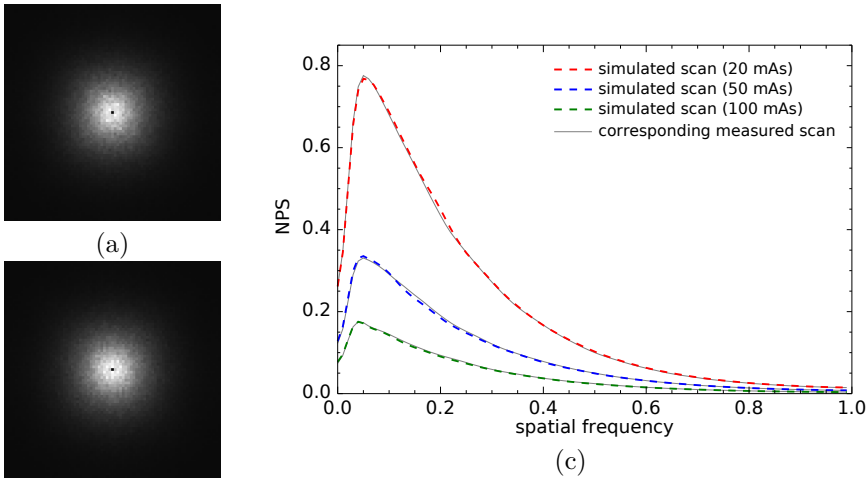

(a) (b) (c)

Figure 3.6: The illustration of the 2D NPS for (a) the measured and (b) the simulated scan of 20 mAs. (c) The comparison of radially averaged NPS for the measured and the simulated scans of 20, 50, 100 mAs.

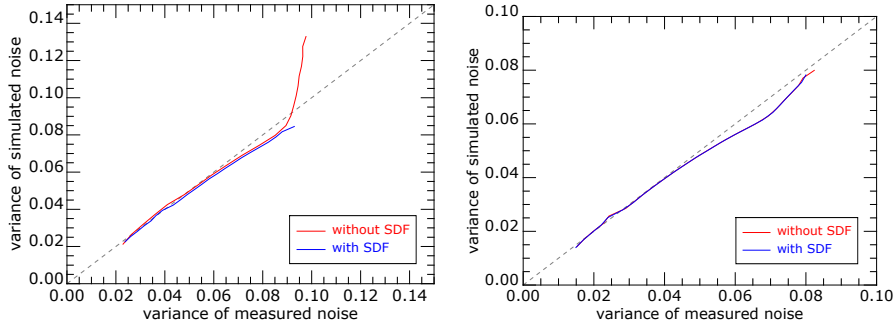

Figure 3.7: Comparison of the variance of the simulated noise versus acquired noise for the scan of (a) 20 mAs and (b) 50 mAs in the projection domain. The prediction deviates from the measurement for the scan of 20 mAs if the SDF has not been included in the simulation procedure.

to suppress the image noise and therefore the variance of the acquired scan is found to be less than predicted. A new experiment has been designed to investigate the effect of this filter. The idea is to compare the simulated and real noise in the sinogram domain by subtracting two scans that have been taken at the same position. The difference between the two scans contains (almost) exclusively noise. The simulated noise is expected to be similar to that of the acquired one. Therefore, the aim is to estimate $\mathrm{var}\left[\rho_{sim}^{(\alpha)} - \rho_{real}^{(\beta)}\right]$ and compare it with $\mathrm{var}\left[\rho_{real}^{(\alpha)} - \rho_{real}^{(\beta)}\right]$ where $\rho^{(\alpha)}$ and $\rho^{(\beta)}$ indicate attenuation value of low and high dose scan, respectively. In order to compare the variances, the predicted variances were binned and for each bin the detectors associated with it were identified. For each bin, the variance of the measured signal over these detectors was computed. The variances from the measurements are compared to the predicted variances in Fig. 3.7. For the simulated scan of 20 mAs, the prediction computed without SDF deviated from the measurement for high variances, Fig. 3.7(a), shows that the variance of the simulated scan is higher than the acquired one before applying the SDF. Including the SDF in the simulation brought the noise level much closer to the acquired noise (the blue curve Fig. 3.7). Fig. 3.7(b) compares the noise level of the simulated and the acquired scans of 50 mAs. For the higher dose scans, where the signal level is always higher than the smoothing threshold, applying the SDF does not have any effect on the simulation procedure and therefore the curve is very close to the line of identity for both models (with/without smoothing).

The same experiment was repeated for a small (6 cm diameter) water filled PMMA cylinder. For such a small object, the effect of beam hardening is less

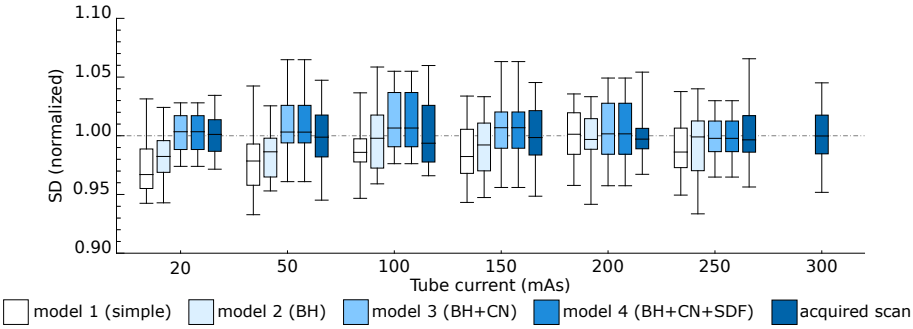

Figure 3.8: Presentation of the standard deviation of the reconstructed images of a 6 cm water phantom for different models at different levels of tube current.

compared to the 21 cm phantom. A high-dose scan of 300 mAs was used and the lower-dose scans were simulated. Fig. 3.8 compares the standard deviation of the reconstructed images in the real and simulated lower-dose scans. Restoring the correlation increased the noise level in image space; however, compensating beam hardening effect did not have significant impact on the results since the beam hardening is negligible for a 6 cm water phantom. In addition, the detected signal is always above the SDF threshold and therefore SDF did not have any effect on the simulated scans, consequently, the noise variance of model 2, 3, and 4 are almost the same.

Table 3.2 compares the standard deviation of the noise for the acquired and the simulated images of the first and second experiments. It reveals a close agreement in the observed and the simulated lower-dose scans. Accordingly, the relative error is less than 2.1% and 1.1% for 21 cm and 6 cm water phantoms, respectively, which confirms the accuracy of the proposed lower-dose simulation tool. For instance, the relative error is around 1% for the simulated scan of 20 mAs where the tube current was reduced by the factor of 15.

In the third experiment, an anthropomorphic thorax phantom (CIRS E2E SBRT) was analyzed by performing a sequential scan. The lower-dose scans were simulated from the scan of 300 mAs using model 4. The experiment was the same as the first experiment but this time a filtered backprojection (FBP) algorithm, without applying any smoothing kernel, was employed for the reconstruction. For the comparison, the phantom was divided into three regions, represented in Fig. 3.10(a), and the standard deviations in the uniform ROIs were compared. Fig. 3.9 compares the noise variance of the simulated and the acquired images. It can be seen that the proposed framework is able to model the noise for different regions at different levels of tube current. A detailed comparison between the simulated and the acquired images is presented in Table 3.3 where the relative error is less than 1.0%.

Table 3.2: The detailed comparison of noise levels of the acquired and the simulated LdCT images at different levels of tube current for 21 cm and 6 cm water phantoms. The standard deviation of the noise in uniform ROIs were used for comparison.

	21 cm water phantom						6 cm water phantom		
Tube	center			periphery			center		
Load	real	sim	error	real	sim	error	real	sim	error
300	5.25	-	- %	4.87	-	-	4.85	-	-
250	5.77	5.71	1.1%	5.29	5.28	0.2%	5.27	5.27	0.0%
200	6.43	6.37	0.9%	5.89	5.84	0.8%	5.77	5.80	0.4%
150	7.45	7.29	2.1%	6.72	6.74	0.2%	6.61	6.64	0.5%
100	9.09	8.95	1.5%	8.23	8.18	0.5%	7.95	8.05	1.1%
50	13.03	12.87	1.2%	11.69	11.67	0.1%	11.14	11.23	0.7%
20	18.59	18.79	1.0%	17.90	18.00	0.5%	17.67	17.70	0.1%

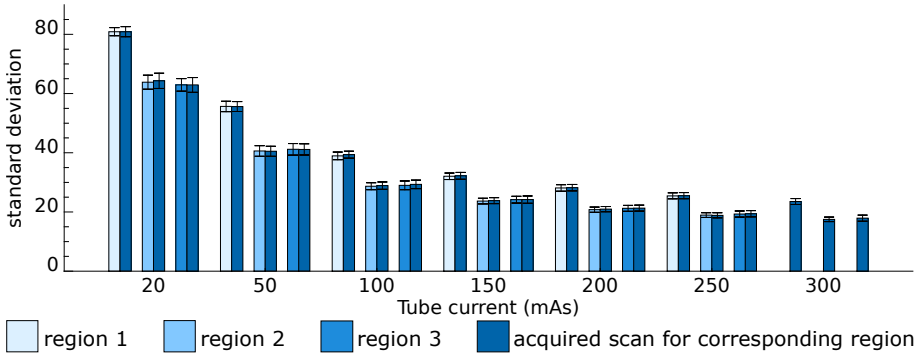

Figure 3.9: Comparison of the noise level of the simulated and measured images of an anthropomorphic thorax phantom for different regions at different levels of tube current.

Fig. 3.10 represents the simulated images and corresponding lower dose acquired images.

In clinical applications, automatic tube current modulation is widely used to adjust the X-ray tube current for each projection angle which results in a significant dose reduction to the patient. The tube current at each projection angle depends on the size and the different densities of the tissues, therefore, in order to get the same tube current profile for repeated scans the tube angle and the bed position should be exactly the same for all scans. The proposed framework was expanded to simulate the lower-dose helical scans with AEC. The tube current of lower-dose scan was estimated according to the tube current

Table 3.3: The detailed comparison of noise levels of the acquired and the simulated LdCT images for the sequential scan of the anthropomorphic thorax phantom.

Tube	region 1			region 2			region 3		
Load	real	sim	error	real	sim	error	real	sim	error
300	23.54	-	-	17.51	-	-	17.92	-	-
250	25.50	25.44	0.2%	18.87	18.94	0.3%	19.40	19.30	0.4%
200	28.21	28.12	0.3%	20.96	20.78	0.8%	21.31	21.23	0.3%
150	32.22	32.06	0.5%	23.83	23.69	0.5%	24.18	24.17	0.0%
100	39.36	38.95	1.0%	28.89	28.69	0.7%	29.31	28.99	1.0%
50	55.61	55.65	0.06%	40.51	40.60	0.2%	41.13	41.17	1.0%
20	80.89	80.88	0.01%	64.31	63.84	0.7%	62.91	62.93	0.2%

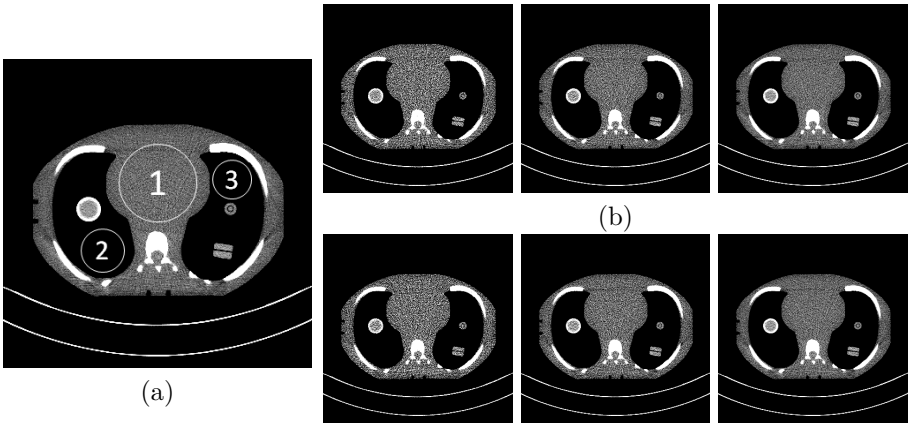

Figure 3.10: Presentation of (a) the measured high-dose image of 300 mAs, (b) corresponding acquired lower-dose images, and (c) simulated lower-dose images of 20, 50, and 100 mAs (from left to right) using the final model for the sequential scan of the thorax phantom (window level: 0 HU, window width: 200 HU).

of higher dose scan and nominal tube current as follows

$$\text{tube current}_{low} = \frac{\text{nominal tube current}_{low}}{\text{nominal tube current}_{high}} \times \text{tube current}_{high} \qquad (3.22)$$

Using the same anthropomorphic thorax phantom, the experiment was repeated by doing a helical CT scan with AEC. The tube current of the

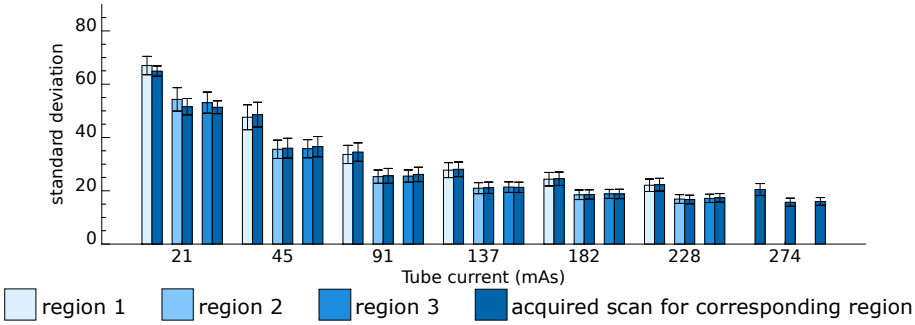

Figure 3.11: Representation of the noise level in the simulation of the lower-dose helical scan of the anthropomorphic thorax phantom with AEC.

high-dose scan was extracted from the header and the corresponding lower-dose tube current was estimated by Eq. 3.22. The high-dose scan of 274 effective mAs was used as the input high dose scan (effective mAs is a parameter setting on Siemens CT scanner defined as the product of tube current and rotation time divided by the beam pitch [93]). The simulation procedure was the same for helical and sequential scans. Fig. 3.11 represents the noise value of the simulated and the acquired scans for different regions at different levels of tube current. The main problem in scans with AEC is that the profile of tube current is not the same for repeated scans due to the difference in the position of tube in each scan. In addition, the profile of modulated tube current is not the same for high and low dose CT protocols. This misalignment results in a larger error in the simulation of lower dose helical scans compared to the sequential one. Table 3.4 reports the standard deviation from uniform ROIs in the reconstructions from the helical scan of the anthropomorphic thorax phantom. Even though the relative error has slightly increased, the error is less than 5.3%, confirming good performance of the proposed model for helical CT scanning with AEC.

An anthropomorphic abdomen phantom (CIRS E2E SBRT) was also performed to mimic abdominal CT scans. The high dose scan of 300 mAs was used for the simulation. The MLTR (8 iterations and 40 subiterations) was used for the reconstruction. For the comparison, three uniform regions were selected, represented in Fig. 3.12(a). Table 3.5 reports the standard deviation of the noise in the simulated and the acquired images at different levels of tube current for each region. Fig. 3.12 shows the simulated images and corresponding lower dose acquired images.

In order to increase the clinical relevance of the experiments, a realistic CIRS head phantom (Proton Therapy Dosimetry Head, Model 731-HN) was scanned with a routine clinical protocol [helical, AEC, Pitch: 0.55]. The high-

Table 3.4: Comparison of the noise level in the reconstruction of lower-dose images at different levels of tube current for anthropomorphic abdomen phantom.

Tube	region 1			region 2			region 3		
Load	real	sim	error	real	sim	error	real	sim	error
300	20.47	-	-	15.70	-	-	16.00	-	-
250	22.28	22.07	0.9%	16.72	16.91	1.1%	17.35	17.14	1.2%
200	24.52	24.33	0.7%	18.60	18.51	0.5%	18.81	18.83	0.1%
150	28.06	27.75	1.1%	21.13	20.97	0.7%	21.30	21.38	0.3%
100	34.53	33.63	2.6%	25.60	25.30	1.1%	26.14	25.53	2.3%
50	48.57	47.61	1.9%	36.00	35.57	1.1%	36.56	35.80	2.0%
20	64.93	66.99	3.1%	51.56	54.31	5.3%	51.35	53.08	3.3%

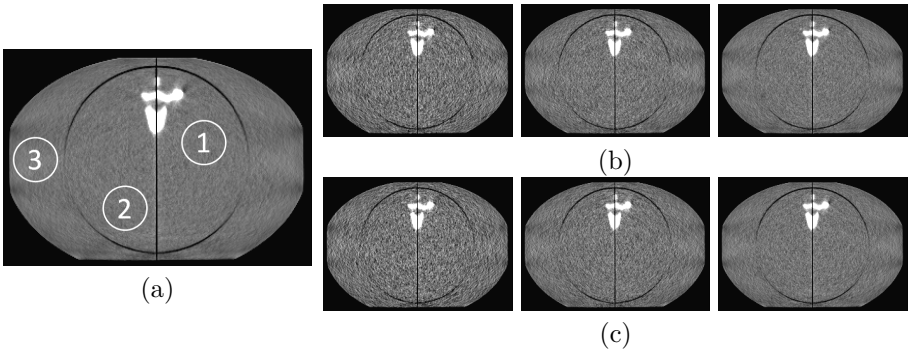

Figure 3.12: Presentation of (a) the high-dose image of 300 mAs, (b) corresponding acquired lower-dose images, and (c) simulated lower-dose images of 20, 50, and 100 mAs (from left to right) using the final model for the sequential scan of the abdomen phantom (window level: 0 HU, window width: 300 HU).

dose scan of 192 effective mAs was used as the input high-dose scan to simulate the lower-dose scans. Subsequently, the simulated scans were transferred into the scanner and reconstructed by the scanner's reconstruction software [Kernel: Hr38, Iterative, Strength: 3]. Table 3.6 compares the noise standard deviation in a uniform region in images obtained from the simulated and acquired scans. For instance, the relative error is 3.2% for the simulation of LdCT scan of 24 effective mAs where the tube current reduced to 12.5% of the normal tube current. Accordingly, the standard deviation of the predicted noise is slightly less than the measured one. Comparing the tube current of measured and simulated scans, it appeared that the level of tube current in the simulated

Table 3.5: Comparison of the noise level in the reconstruction of lower-dose images at different levels of tube current for the sequential scan of the anthropomorphic abdomen phantom.

Tube	region 1			region 2			region 3		
Load	real	sim	error	real	sim	error	real	sim	error
300	11.50	-	-	12.36	-	-	12.69	-	-
250	12.44	12.51	0.5%	13.38	13.30	0.6%	13.23	13.30	0.4%
200	13.99	13.96	0.2%	14.67	14.66	0.1%	14.06	14.17	0.8%
150	16.07	16.12	0.3%	16.81	16.74	0.4%	15.42	15.79	2.3%
100	19.77	19.50	1.3%	19.92	19.91	0.0%	17.86	18.36	2.7%
50	26.73	26.80	0.2%	27.00	27.28	1.0%	23.76	24.67	3.8%
20	35.93	36.93	3.3%	35.82	37.12	3.6%	34.66	35.32	1.8%

Table 3.6: The detailed comparison of noise levels in the measured and the simulated lower-dose images at different levels of tube current for realistic CIRS head phantom.

Tube Load	real	sim	error
192	3.39	-	-
140	3.92	3.91	0.2%
117	4.23	4.24	0.2%
93	4.79	4.69	2.2%
70	5.47	5.44	0.5%
47	6.77	6.65	3.0%
24	9.52	9.21	3.2%

scan is higher than the measured one and consequently a smaller noise level in the simulated images is expected. This misalignment is mainly due to dissimilar behavior of the system for high and low dose scans. Fig. 3.13 compares the tube current of the estimated and the measured lower-dose scan of 24 effective mAs.

The NPS was also computed for a 61×61 voxel uniform ROI in 32 slices, indicated in Fig. 3.15(a), to compare the noise texture in the acquired and simulated scans. Fig. 3.14 compares the NPS of the acquired and simulated scans. As mentioned earlier, the standard deviation of the noise in the simulation of lower dose scan of 24 and 47 mAs is underestimated due to misalignment in the tube current, which results in a higher amplitude of NPS for the acquired scans. Therefore, the radially averaged NPS in Fig. 3.14 was normalized to compared the shape of the 1D NPS in the acquired and simulated scans. Comparing the NPS in Fig. 3.14 shows a good agreement

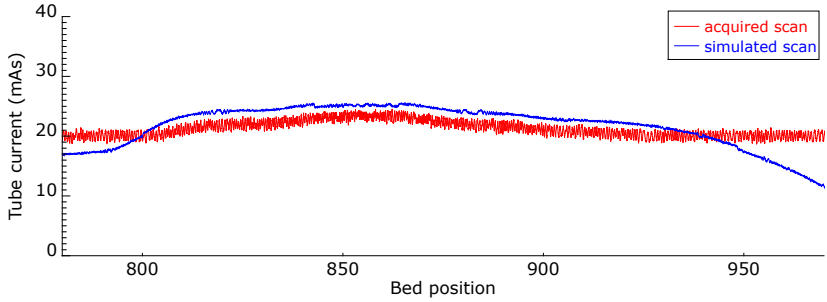

Figure 3.13: Illustration of the measured and the estimated lower-dose tube current of a helical scan at different projection angle. It is clearly seen that the tube current of the simulated scan is higher than the measured one and therefore the standard deviation of the simulated images would be less than the acquired scan.

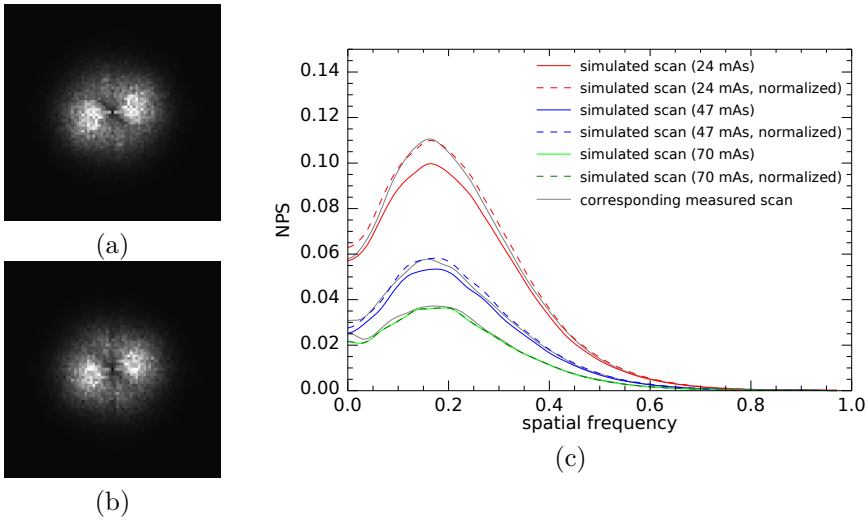

Figure 3.14: The illustration of the 2D NPS of (a) the measured and (b) the simulated scan of 24 mAs. (c) The comparison of the radially averaged NPS for the measured and the simulated scans of 24, 47, 70 mAs.

between the real and the simulated noise which validates the accuracy of proposed model. Fig. 3.15 shows the high-dose scan of 192 mAs and its corresponding measured and simulated lower-dose scans.

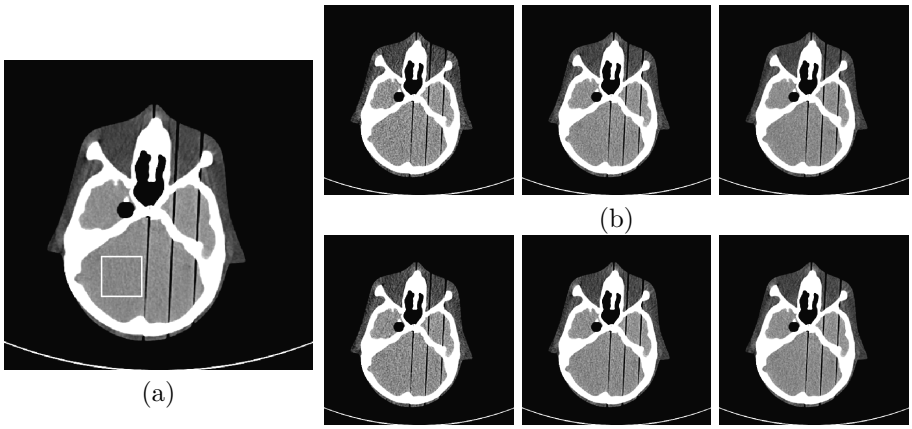

(a) (b) (c)

Figure 3.15: Presentation of (a) the measured high-dose image of 192 effective mAs and (b) corresponding acquired and (c) simulated lower-dose images of 24, 47, and 70 effective mAs (from left to right) using the proposed framework. The square in (a) indicates ROI that was used to compute the NPS in Fig. 3.14 (window level: 60 HU, window width: 120 HU).

3.4 Discussion

In this study, a new strategy was proposed to simulate the lower-dose CT scan from an existing standard-dose scan which can be used to optimize CT acquisition protocols. The main application of the developed tool is to determine the lowest exposure scan which still produces sufficient information for the clinical task.

The developed tool simulated lower-dose scans by adding synthetic noise to a high-dose scan in the projection domain which requires access to raw sinogram data. The general idea was to estimate the noise equivalent number of photons in the high dose scan and apply a thinning technique to simulate the lower dose scan. The transmitted signal was considered as the combination of a Poisson and a zero-mean normal distribution to represent the effect of the quantum and electronic noise. The proposed framework accounts for the bowtie filter, for correlated noise between neighboring detector elements, for the beam hardening effect, and for the non-linear smoothing filter. The noise in the high dose scan is also accounted for by employing a binomial distribution for thinning. The main difference with most existing procedures is the modeling of the noise correlation. It was important to include this correlation in the simulation procedure because the noise propagation through the image reconstruction is not the same for correlated and uncorrelated noise. The experiments revealed

that the correlated noise introduced higher noise in the image space for the same noise variance in the sinogram domain. The signal dependent filter was also included in the simulation procedure. Before applying the SDF, the level of the predicted noise was more than the measured one for very noisy data, however, including SDF in the simulation mitigated that.

All the experiments have been performed on Siemens SOMATOM Force scanner, however, the model can be extended for other scanners after appropriate calibration of $I_0^{(1)}$, electronic noise, and correlation matrix of neighboring detector elements. In this study, tube current reduction, without changing any other acquisition parameters (fixed kVp, rotation time, and collimation), was modeled and the tube voltage was set at 120 kVp in all experiments. Any change in acquisition parameters may affect the signal properties and therefore the parameters should be calibrated accordingly.

Different phantom studies with different acquisition protocols were used to evaluate the accuracy of the proposed framework. The results demonstrated excellent accuracy in providing realistic lower-dose images where the texture and magnitude of the simulated noise matched the measurements in both image and projection domains. The standard deviation of the reconstructed image in uniform ROIs revealed a close agreement of the noise level in the observed and simulated lower-dose scans where the relative error was on the order of $\sim$1% for sequential and $\sim$3% for helical scans. For instance, the relative error in the simulation of the LdCT scan of 20 mAs, where the tube current was reduced to 6.6% of the normal tube current, was 1.0% and 0.7% for water and anthropomorphic thorax phantom, respectively. The local NPS of reconstructed images demonstrated a strong agreement between the real and simulated noise. Comparison of the noise level in the sinogram domain also confirmed the good performance of the proposed model.

Sequential and helical scans with/without AEC can be simulated using the proposed framework. However, the overall error in the simulation of helical scans is higher (when compared with sequential scans) due to the (unpredictable) variation in the profile of tube current for high and low-dose CT protocols when AEC is active. In other words, the behavior of tube current modulation was not the same for low and high dose scans and this dissimilarity introduced an additional error in the simulated lower-dose scans, but we consider the results still acceptable for the optimization of CT scan protocols.

In summary, the proposed lower-dose simulation model can be used to optimize CT acquisition protocols to decrease the radiation dose to the patients. Our main motivation is to determine the lowest possible X-ray CT radiation dose that still produces sufficient information for proton therapy treatment planning, which is the subject of ongoing research.

Acknowledgments

The authors would like to warmly thank Edmond Sterpin and Xavier Geets for the initial design of the research, Walter Coudyzer and Koen Salvo for their contribution in data collection, and Karl Stierstorfer and Frederic Noo for their valuable comments and suggestions.

4

Low-dose CT allows for accurate proton therapy dose calculation and plan optimization

Masoud Elhamiasl, Koen Salvo, Kenneth Poels, Gilles Defraene, Maarten Lambrecht, Xavier Geets, Edmond Sterpin, Johan Nuyts., Published in *Physics in Medicine & Biology*, vol. 67, no. 19, p. 195015, 2022.

Abstract

Objective. Protons offer a more conformal dose delivery compared to photons, yet they are sensitive to anatomical changes over the course of treatment. To minimize range uncertainties due to anatomical variations, a new CT acquisition at every treatment session would be paramount to enable daily dose calculation and subsequent plan adaptation. However, the series of CT scans results in an additional accumulated patient dose. Reducing CT radiation dose and thereby decreasing the potential risk of radiation exposure to patients is desirable, however, lowering the CT dose results in a lower signal-to-noise ratio and therefore in a reduced quality image. We hypothesized that the signal-to-noise ratio provided by conventional CT protocols is higher than needed for proton dose distribution estimation. In this study, we aim to investigate the effect of CT imaging dose reduction on

proton therapy dose calculations and plan optimization. *Approach.* To verify our hypothesis, a CT dose reduction simulation tool has been developed and validated to simulate lower-dose CT scans from an existing standard-dose scan. The simulated lower-dose CTs were then used for proton dose calculation and plan optimization and the results were compared with those of the standard-dose scan. The same strategy was adopted to investigate the effect of CT dose reduction on Water Equivalent Thickness (WET) calculation to quantify CT noise accumulation during integration along the beam. *Main results.* The similarity between the dose distributions acquired from the low-dose and standard-dose CTs was evaluated by the Dose-Volume Histogram (DVH) and the 3D Gamma analysis. The results on an anthropomorphic head phantom and three patient cases indicate that CT imaging dose reduction up to 90% does not have a significant effect on proton dose calculation and plan optimization. The relative error was employed to evaluate the similarity between WET maps and was found to be less than 1% after reducing the CT imaging dose by 90%. *Significance.* The results suggest the possibility of using low-dose CT for proton therapy dose estimation, since the dose distributions acquired from the standard-dose and low-dose CTs are clinically equivalent.

4.1 Introduction

Proton therapy is an advanced form of external beam radiotherapy which utilizes high-energy proton beams to kill cancer cells. Compared to photons, protons offer a better localized dose deposition which enables the delivery of a highly conformal dose to the tumor while minimizing the damage to the surrounding healthy tissue, yet they are sensitive to anatomical variations. The total therapeutic radiation dose is typically split up into several tens of smaller fractions over the course of treatment, from several days to weeks [36, 18]. Anatomical changes frequently occur over the course of treatment, therefore, the delivered dose might differ from what was originally planned. Anatomical changes can occur in any region due to tumor shrinkage, weight loss, organ motion, variation in organ filling, etc. For example, shifts up to 5 mm between the tumor borders have been reported for patients who underwent stereotactic radiosurgery for brain metastases [123]. In esophageal cancer radiotherapy, shift up to more than 1 cm was observed in cranio-caudal direction, for distal locations [124]. Interested readers are referred to [36] for a detailed examination of anatomical changes over the course of treatment.

Day-to-day anatomical variations can substantially compromise the properties of proton beams [125]. That is due to the fact that the stopping power of the tissues traversed by the protons can vary substantially, and even

relatively small changes of the trajectory of the protons through the body can have an important effect on the position of the Bragg peak. Research has shown that around one-third of proton patients required one or more repeated CT scans to adapt the plan during the course of treatment [126]. Applying a safety margin around the clinical target volumes or using robust optimization is necessary to account for the anatomical changes and ensuring coverage of the target. However, surrounding tissue will be exposed to higher levels of radiation, increasing the risk of side effects such as secondary malignancy. Image-guided proton therapy tries to reduce this margin by improving the set-up accuracy, however, the anatomical changes cannot be taken into account by translational and rotational setup corrections [127, 36]. Adaptive Proton Therapy (APT) could be employed to detect these changes and adapt the plan if it is necessary.

APT aims to deliver radiation dose accurately in the presence of anatomical changes by employing a closed-loop imaging system to systematically monitor these changes and modify the treatment plan if required [34]. APT has been shown to have the advantage of reducing the safety margin compared to conventional image-guided approaches [128, 129, 130]. By enabling detection of and correction for changes, APT has the potential to improve the quality of treatment by reducing Organ At Risks (OARs) exposure and toxicity and also facilitating dose escalation and therefore improved tumor control. A survey in 2019 showed that two thirds of radiotherapy centers worldwide are willing to implement adaptive approach for at least one new tumor site [131, 127].

In-room or off-room CT, Cone-Beam CT (CBCT), and on-board MR are the main modalities that can be used for APT. CT is the most accurate modality for estimating stopping powers, and provides also adequate contrast for image delineation. In the current state-of-the-art of the imaging device, the systematic acquisition of a CT image using an in-room CT would provide the best accuracy for dose calculation and subsequent plan adaptation [132]. A new CT scan directly before each treatment session would be paramount in order to exploit the full potential of proton therapy. Even though the dose from a CT is small compared to the therapeutic radiation, the total dose associated with the series of these CTs can be significant [78], especially if a 4D CT is acquired to account for breathing effects. This is highly relevant for children due to their longer life expectancy and susceptibility to mutagenesis [66, 67, 68]. For example, cumulative doses from 2–3 head CTs could almost triple the risk of brain tumors and 5–10 head CTs could triple the risk of leukaemia in the 10 years after the first scan for patients younger than 10 years [65]. Therefore, minimizing the ionising radiation doses from the imaging system is crucial to reduce the risk of radiation-induced malignancies [62].

Reducing CT dose is always desirable, however, lowering the radiation dose

results in a lower signal-to-noise ratio and therefore in a reduced image quality which may deteriorate the diagnostic and therapeutic value of CT images. We hypothesize that the signal-to-noise ratio provided by conventional CT protocols is higher than needed for accurate proton therapy dose estimation. In this research, we aim to investigate the effect of CT imaging dose reduction on proton therapy dose estimation. It should be noted that the effect of CT dose reduction on segmenting the target volumes and OARs (image contouring) falls out of the scope of this paper.

The rest of this paper is structured as follows. Section 4.2 begins with describing the research method used in this study. Section 4.2.1 and 4.2.2 discuss the possible approaches to investigate the effect of reducing CT dose on proton therapy dose estimation, including the effect of CT dose reduction on dose calculation, plan optimization, and water equivalent thickness estimation. Experimental results are presented in Section 4.3, followed by a discussion in Section 4.4. Finally, some concluding remarks are drawn in Section 4.5.

4.2 Materials and Methods

In order to assess the effect of CT dose reduction on proton therapy dose estimation, it is crucial to have the standard-dose CT along with the corresponding LdCT images. As the standard-dose CT, we have always used the CT acquired with the clinical protocol of the Radiation Oncology Department of the University Hospital of Leuven in Belgium. The dose distributions can then be estimated from the LdCTs and compared with that of the standard-dose scan. It is not ethical to scan the same patient several times using different acquisition protocols to generate the standard and low-dose CT pairs. Anthropomorphic phantoms can be used instead [133], however, their clinical relevance is less. A more sophisticated strategy is to use a tool to generate realistic LdCTs from an existing standard-dose CT scan and use them for proton therapy dose calculation.

To verify our hypothesis and enable a patient-dependent reduction of the CT dose, a LdCT simulation tool was developed and validated [134] to simulate realistic lower-dose CT scans from an existing standard-dose scan. This tool produces a virtual lower-dose scan by adding the appropriate amount of (position dependent and correlated) noise to the standard-dose scan. Several phantom studies with different acquisition protocols were performed on different CT scanners to evaluate the accuracy of the proposed model. The results demonstrated excellent accuracy in providing realistic LdCT where the texture and magnitude of the simulated noise matched the measurements. The interested reader is referred to [134] for further details on the developed model.

LdCT simulation with a gradual reduction in dose using real patient data

enables us to verify to what extent the CT dose can be sacrificed without losing any relevant information required for proton dose estimation. Several experiments have been designed to assess the possibility of using LdCTs for proton therapy application. Each test starts from a standard-dose CT image where the results based on this reference CT image will be used as ground truth. Then noise is added to the CT scan to emulate the effect of CT dose reduction, and the same test is repeated for the simulated LdCTs. Comparing the results with those of the standard-dose scan will quantify the effect of CT dose reduction. The possible approaches to analyze the effect of reducing CT dose are discussed in the following sections.

4.2.1 Dose estimation error

In this work, a Pencil Beam Scanning (PBS) technique is employed for proton dose delivery. For PBS, spot positions and spot weights are the machine parameters that define the plan. After defining the objectives and constraints, the Treatment Planning System (TPS) selects the spot positions and their initial weights and works backward to minimize the objective function by modifying the spot weights. The plan optimization is therefore an iterative process to find the optimum spot weights that minimize the objective function. At each iteration, the dose distribution is calculated from the CT image, spot positions, and spot weights from which the dose to ROIs and OARs could be identified.

The dose calculation step can be affected by the CT noise. Plan optimization, which is an iterative process, can also be severely affected by the higher level of CT noise in LdCTs. It is conceivable that the CT noise propagation effects are more damaging during an iterative plan optimization (due to accumulation of errors in an iterative process) than during a single dose calculation. In addition, the noise in the LdCTs can affect plan initialization. For these reasons, we consider two scenarios: the dose calculation error and planning optimization error. It is crucial to investigate the effect of CT noise on these two errors separately owing to the fact that the error of dose calculation might be compensated by the error in plan optimization, and vice versa.

Dose calculation error

In this experiment, LdCTs are only used for proton dose calculation. It is crucial to make sure that the calculated dose is a close representation of the actual delivered dose to the patient. Any deviation from the actual dose could have a serious impact on the quality of treatment. After delineating the target volume and OARs and defining the beams, the plan is optimized on the standard-dose CT image (OptHigh). The dose distribution will be then

recomputed on a set of LdCTs (CalcLow) using the same optimized plan and the results compared with that of the standard-dose scan (OptHigh-CalcHigh). In other words, this experiment examines the effect of reducing CT noise on dose calculation in only one iteration.

Plan optimization error

The second experiment assesses the effect of CT dose reduction on the plan optimization in which the plan is reoptimized separately for each LdCT (OptLow) and the doses are calculated using the standard-dose scans (CalcHigh). The results are then compared with the reference dose distribution (OptHigh-CalcHigh). LdCTs can affect the optimizer, first, during plan initialization where the spot positions and their initial weights are chosen, and second, at each iteration where the dose distribution is calculated. It should be mentioned that dose calculation error and plan optimization error are not independent. The plan optimization is an iterative procedure and its error is mainly due to the small error during dose calculation at each iteration. In this test, we are interested to see if these small errors during dose calculation could drive the optimization to a wrong solution. It is worth mentioning that the plan optimization test can be easily affected by other sources of uncertainties during the optimization procedure where a slight change of initial conditions or a small variation at one iteration may lead to unpredictable changes in the optimized plan. Therefore, it is crucial to minimize other sources of variability as much as possible to focus on CT noise only.

To summarize, three dose distributions will be estimated for each case as follows:

- *OptHigh-CalcHigh*: The plan was optimized on the standard-dose CT. The final dose was also calculated on the standard-dose CT. OptHigh-CalcHigh represents the closest approximation of the delivered dose to the patient using the optimal plan, therefore, it will be considered as the ground truth for validating the other doses.

- *OptHigh-CalcLow*: The plan was optimized on the standard-dose CT, but the final dose was recalculated on the LdCT. OptHigh-CalcLow shows the effect of CT noise on dose calculation and is the most robust and reliable test.

- *OptLow-CalcHigh*: The plan was optimized on LdCT, and the final dose was recalculated on the standard-dose CT. OptLow-CalcHigh shows the effect of CT noise on plan optimization and represents the closest approximation of the delivered dose to the patient for cases in which the plan is optimized on LdCT.

We have not used OptLow-CalcLow, where the plan optimization and also the final dose calculation would be carried out on the LdCT. The dose distributions from this experiment are not useful because errors on dose calculations are likely to be compensated by errors during plan optimization, such that the final estimated dose could agree well with the reference dose, despite significant errors during plan optimization.

4.2.2 Water equivalent thickness error

In proton therapy applications, the radiological thickness of a material is expressed in terms of Water Equivalent Thickness (WET). WET can be estimated by adding Stopping Power Ratio (SPR) values for each voxel along the beam.

Integrating along a line is intrinsic to dose calculation and plan optimization tasks. Therefore, an alternative solution to analyze the effect of CT dose reduction is to compare WET maps acquired from the standard-dose and LdCTs. This test could therefore determine if the surviving noise after integration along the beam is strong enough to cause problems for proton therapy dose estimation. The integration process can be considered as a smoothing filter that could partially suppress the noise in the LdCTs. The CT noise is high frequency noise, which implies that there are negative noise correlations between neighboring pixels. Therefore, by integrating along beams, some of the noise will cancel out.

In this work, RayStation TPS (RaySearch Laboratories, Sweden) is employed for treatment planning. In RayStation the CT-number [HU] of a voxel is first converted to mass density [g/cm^3] by a site-specific CT-to-mass density calibration curve. The mass density is then mapped to material by selecting one of the 55 predefined materials which has the closest mass density to the mass density of the voxel. Finally, the stopping power is calculated from the mass density of the voxel, the characteristics of the RayStation material (atomical composition, mean excitation energy) and the proton energy at the position of the voxel.

After converting the CT-numbers [HU] to SPRs, the WET can be estimated as the line integral of the SPR [135]. The WET maps acquired from the LdCTs can then be compared with that of the standard-dose CT to quantify the remaining noise after integration.

4.2.3 Patient cases and treatment planning

One phantom and three clinical cases were used to analyze the effect of reducing CT dose on proton therapy dose estimation. Standard-dose CTs were acquired with a routine clinical protocol at the Radiation Oncology Department of the University Hospital of Leuven in Belgium. In each case, the LdCTs with gradual

reduction in dose were simulated by employing the in-house LdCT simulator. The dose distributions and WET maps were then estimated for the LdCTs and the results were compared with the ground truth. The plans were defined by a radiation therapy technologist in RayStation V9B. The details of each case are as follows:

- *Case 1*: A realistic proton therapy head phantom (Proton Therapy Dosimetry Head, Model 731-HN) was scanned with a routine clinical protocol [Siemens SOMATOM Force, 120 kVp, 340 effective mAs, pitch: 0.55, pixel size: 0.51×0.51×2 mm, $CTDI_{vol}$[1]: 51 mGy, Effective dose ≈ 5 mSv]. The brainstem was contoured and the Planning Target Volume (PTV) was defined like a horseshoe around the brainstem. An Intensity Modulated Proton Therapy (IMPT) plan with a typical setup of 4 beams [50°, 130°, 220°, and 300°] was used and a dose of 60 Gy RBE (30 fractions of 2 Gy RBE, non-robust optimization) was prescribed on the PTV.

- *Case 2*: A standard-dose 3DCT scan [Siemens SOMATOM EDGE, 120 kVp, 340 effective mAs, pitch: 0.55, pixel size: 0.58×0.58×1 mm, $CTDI_{vol}$: 48 mGy, Effective dose ≈ 5 mSv] of a brain metastases patient was used. An IMPT plan with two beams (260° and 310°) was generated and a dose of 27 Gy RBE (3 fractions of 9 Gy RBE, non-robust optimization) was prescribed on the PTV.

- *Case 3*: A standard-dose 4DCT scan [Siemens SOMATOM Drive, 120 kVp, 50 effective mAs, 10 breathing phases, pitch: 0.09, pixel size: 0.97×0.97×3 mm, $CTDI_{vol}$: 30 mGy, Effective dose ≈ 20 mSv] for an esophageal cancer patient was used. An IMPT plan with two posterior beams (150° and 180°) was generated with the average image of the standard-dose 4DCT as planning CT. A dose of 50.40 Gy RBE (28 fractions of 1.80 Gy RBE) was prescribed on the Internal Clinical Target Volume (iCTV) using robustness settings of 7 mm setup error and 2.6% range error.

- *Case 4*: A standard-dose CT scan [Siemens SOMATOM Drive, 120 kVp, 198 effective mAs, pitch: 1.2, pixel size: 1.52×1.52×3 mm, $CTDI_{vol}$: 13 mGy, Effective dose ≈ 8.5 mSv] of a patient with vertebral metastases was selected. An IMPT plan with three posterior beams (140°, 180°, and 220°) was generated and a dose of 27 Gy RBE (10 fractions of 2.7 Gy RBE, non-robust optimization) was prescribed on the PTV.

[1] $CTDI_{vol}$ (volume CT dose index) values refer to 32cm body phantom.

4.2.4 Evaluation metrics

The dose distributions acquired for the standard-dose and low-dose CT images were compared using the Dose-Volume Histogram (DVH) and 3D Gamma analysis. The DVH provides valuable clinical information, but it does not carry spatial information about the dose distributions, for example, where the hot spots are located. To verify the spatial aspects, the 3D Gamma analysis was used. In the Gamma analysis, the evaluated and reference dose distributions are quantitatively compared through the use of Dose-Difference (DD) and Distance-To-Agreement (DTA) criteria. The Gamma index combines DD and DTA criteria and calculates a scalar dimensionless value which represents the similarity between the evaluated and reference dose distributions.

Let $D_r(\vec{r}_r)$ represent the value of the reference dose at point $\vec{r}_r$ and $D_e(\vec{r}_e)$ denote the value of the evaluated dose at point $\vec{r}_e$. The Gamma index (γ) for each point of the reference dose ($\vec{r}_r$) can be calculated by searching the evaluated dose distribution to find the closest point that has, to some extent, the same dose level. It means:

$$\gamma(\vec{r}_r) = \min_{\vec{r}_e} \Gamma(\vec{r}_r, \vec{r}_e) \tag{4.1}$$

where $\Gamma(\vec{r}_r, \vec{r}_e)$ represents a kind of normalized Euclidean distance between $(\vec{r}_r, D_r(\vec{r}_r))$ and $(\vec{r}_e, D_e(\vec{r}_e))$ and is calculated as:

$$\Gamma(\vec{r}_r, \vec{r}_e)\} = \sqrt{\frac{|\vec{r}_r - \vec{r}_e|^2}{\Delta d^2} + \left|\frac{D_e(\vec{r}_e) - D_r(\vec{r}_r)}{D_r(\vec{r}_r)}\right|^2 \frac{100^2}{\Delta D^2}} \tag{4.2}$$

The variables Δd and ΔD are tolerances that represent the DTA (in mm) and DD (in %) criteria [136]. Here the local Gamma index is defined where the dose difference is normalized by $D_r(\vec{r}_r)$ and the test is carried out over the region receiving at least 10% of the prescribed dose. As an example, 3%/1mm criterion can be seen as the search of the points in the evaluated dose that are less than 1 mm away from $\vec{r}_r$ and have a dose difference smaller than 3% with $D_r(\vec{r}_r)$. If with these values for ΔD and Δd, the value of $\gamma(\vec{r}_r)$ is less than or equal to 1, the point r_r passes the Gamma test. The Gamma Passing Rate (GPR) represents the percentage of voxels in the reference dose that have passed the test. Typically, a clinical threshold of about 90% success for a 3%/3mm criterion is required to consider two dose distributions clinically equivalent [137].

4.3 Results

Each test started by adding noise to the standard-dose scan to simulate the effect of CT dose reduction. LdCTs with 75%, 50%, 40%, 30%, 20%, and 10% of the tube load reported for the standard-dose CT were simulated. A new reconstruction was made using Siemens offline reconstruction software [ReconCT V14.2.0.40998, Reconstruction mode: ADMIRE]. Even though reducing the CT dose beyond 10% of the reference dose is theoretically possible, performing a clinical CT scan below that level is not; therefore, the scan with 10% of the reference CT dose was typically the minimum CT dose that the CT scanner accepted. Figure 4.1 represents the simulated LdCT images with the corresponding acquired standard-dose CT image for each case. It can be seen that the CT noise increases by reducing the CT imaging dose.

4.3.1 Dose estimation error

In the next step, the standard-dose CT image was used for dose calculation and plan optimization (OptHigh-CalcHigh) where the results based on this CT were considered as the ground truth. Figure 4.2 represents an axial slice of each case with overlaid estimated dose of OptHigh-CalcHigh. To minimize additional variation and focus on CT noise only, the same beam angle and same objective functions were used for the standard and LdCTs. In addition, a pencil beam engine was used for dose calculation and plan optimization to avoid additional variation due to the statistical uncertainty of a Monte Carlo simulation.

The dose distributions acquired from the standard-dose and low-dose CT images were compared using the DVH and 3D Gamma analysis. The local 3D Gamma analysis [136] was carried out over the region receiving at least 10% of the prescribed dose.

Dose calculation error

In order to see the effect of CT noise on dose calculation, the plan was optimized on standard-dose CTs. The doses were then recomputed for the LdCTs using the same optimized plan (OptHigh-CalcLow) and the results were compared with that of the standard-dose scan (OptHigh-CalcHigh). For ease of reference, the term OptX-CalcY means that the plan was optimized on LdCT with X% of the reference dose (OptX) and the dose was recalculated for the LdCT with Y% of the reference dose (CalcY). The term High stands for the reference CT dose (standard-dose or high-dose scan).

Figure 4.3(a) compares OptHigh-CalcLow with OptHigh-CalcHigh using DVH analysis for case 3 (the DVHs for all other cases can be found in the

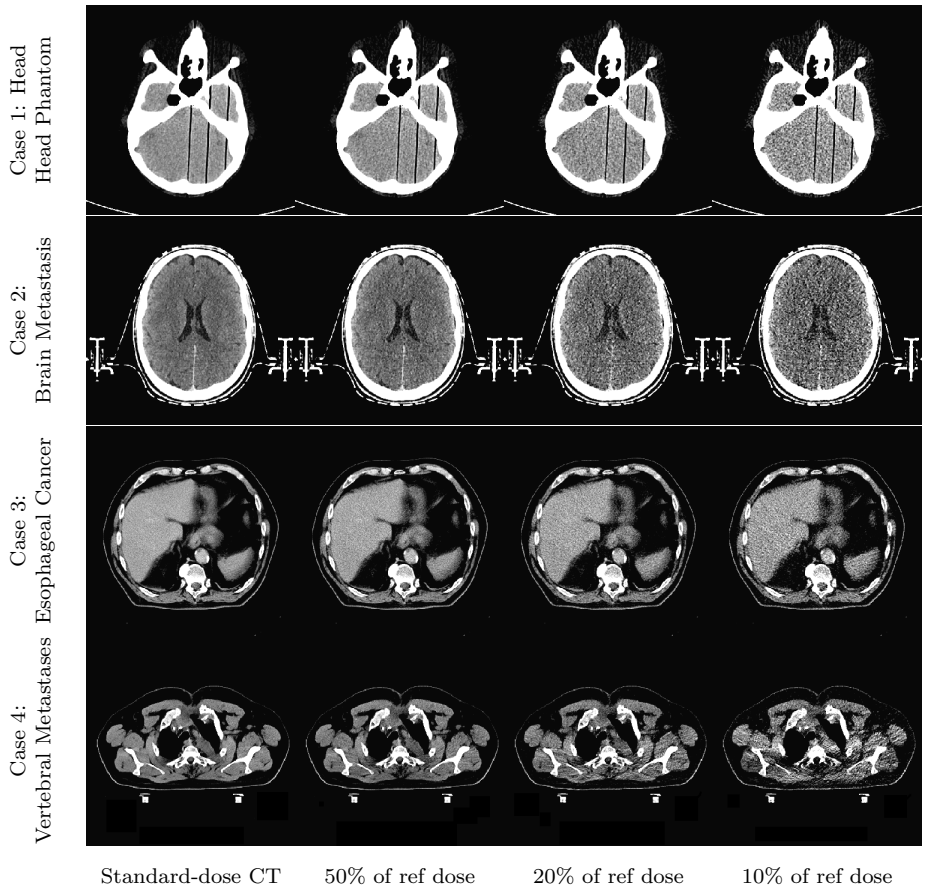

Figure 4.1: Representation of the standard-dose CT image (first column) and the corresponding simulated LdCTs (second, third, and fourth columns). It can be seen that the CT noise increases by lowering the CT dose.

Appendix A, Figure A1). The DVHs are superimposed for target volume and OARs in all cases, showing the similarity between dose distributions calculated from the standard and LdCTs. The dose distributions were also compared using the Gamma analysis. Table 4.1 compares the dose distributions using the Gamma analysis using 3%/1mm and 1%/1mm criteria. Since the standard and low-dose CTs are perfectly aligned, a stricter measure of 1 mm distance-to-agreement was selected instead of the commonly selected 3 mm. The Gamma analysis also confirms the similarity between dose distributions where the mean value of the Gamma is much smaller than 1 and the Gamma passing rate is

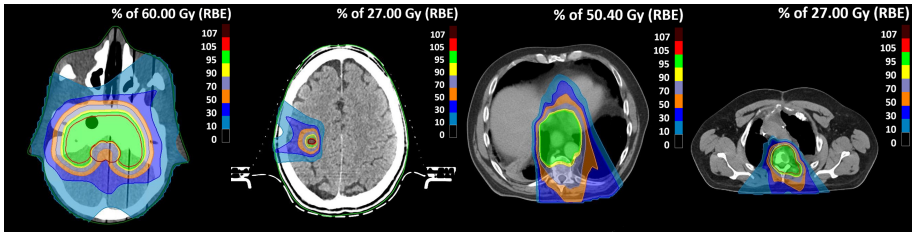

Case 1 Case 2 Case 3 Case 4

Figure 4.2: Axial slices of all the cases with overlaid dose distributions.

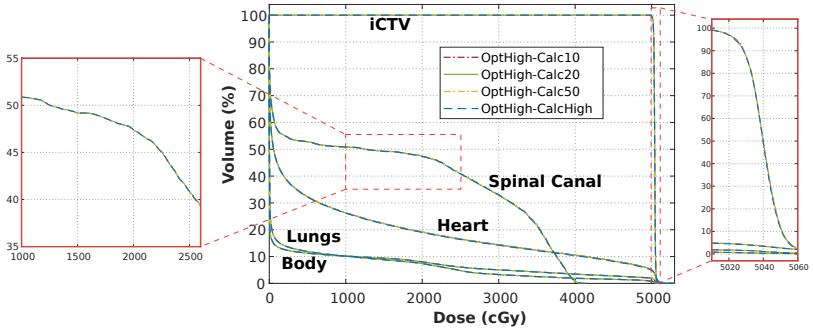

(a) Dose calculation test: OptHigh-CalcLow VS OptHigh-CalcHigh

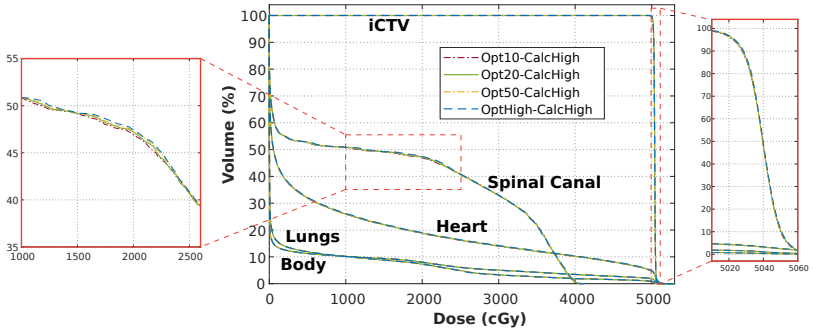

(b) Plan optimization test: OptLow-CalcHigh VS OptHigh-CalcHigh

Figure 4.3: Comparison of the DVHs for OARs and the target volume acquired from the standard and LdCTs to assess the effect of reducing CT imaging dose on (a) dose calculation and (b) plan optimization. Using LdCTs for dose calculation or plan optimization results in DVHs similar to the ground truth.

Table 4.1: Comparison of OptHigh-CalcLow with OptHigh-CalcHigh using the Gamma index passing rate (GPR %) and the mean value of the Gamma index, showing the effect of CT dose reduction on proton dose calculation (reference dose = OptHigh-CalcHigh).

		Case 1		Case 2		Case 3		Case 4	
	Evaluated Dose (%) ⇓	GPR	mean	GPR	mean	GPR	mean	GPR	mean
criteria: 3%, 1mm	OptHigh-Calc75	100	0.00	100	0.01	100	0.04	99.97	0.08
	OptHigh-Calc50	100	0.00	100	0.01	100	0.04	99.93	0.09
	OptHigh-Calc40	100	0.00	100	0.01	100	0.04	99.94	0.08
	OptHigh-Calc30	100	0.00	100	0.01	100	0.05	99.97	0.08
	OptHigh-Calc20	100	0.01	100	0.02	100	0.06	100	0.06
	OptHigh-Calc10	100	0.01	100	0.02	99.92	0.07	98.25	0.16
criteria: 1%, 1mm	OptHigh-Calc75	100	0.01	100	0.03	100	0.07	99.90	0.12
	OptHigh-Calc50	100	0.01	100	0.02	100	0.08	99.85	0.13
	OptHigh-Calc40	100	0.01	100	0.03	99.99	0.08	99.88	0.13
	OptHigh-Calc30	100	0.01	100	0.03	100	0.09	99.93	0.13
	OptHigh-Calc20	100	0.02	100	0.04	99.99	0.10	99.99	0.11
	OptHigh-Calc10	100	0.04	100	0.05	99.87	0.12	97.19	0.25

close to 100% in almost all the cases, except OptHigh-Calc10 in case 4. Having the Gamma passing rate close to 100% and also similar DVHs confirms that the effect of CT noise on proton dose calculation is not significant.

It can be seen that the Gamma values are higher for cases 3 and 4, compared to cases 1 and 2, which indicates a larger dose difference. It is due to the fact that different acquisition protocols were used for case 3 and 4 where the effective mAs was 50 mAs for case 3 and 192 mAs for case 4 compared to 340 mAs for cases 1 and 2. Therefore, the CT noise of the standard-dose CTs for cases 3 and 4 is higher than that of in cases 1 and 2, and therefore a larger error is expected.

Plan optimization error

The LdCTs were also used for plan optimization where the plan was reoptimized on LdCTs and the dose calculation was carried out using the standard-dose scan (OptLow-CalcHigh). The main challenge in this test is that the plan can easily be affected by other sources of variability, such as different initial conditions. Figure 4.3(b) compares OptLow-CalcHigh with OptHigh-CalcHigh for case 3, showing the effect of CT dose reduction on plan optimization (the DVHs for all other cases is presented in the Appendix A, Figure A2). The DVHs are aligned

Table 4.2: Comparison of OptLow-CalcHigh with OptHigh-CalcHigh using the Gamma passing rate (GPR %) and the mean value of the Gamma index showing the effect of CT dose reduction on plan optimization (reference dose = OptHigh-CalcHigh).

		Case 1		Case 2		Case 3		Case 4	
	Evaluated Dose (%) ⇓	GPR	mean	GPR	mean	GPR	mean	GPR	mean
criteria: 3%, 1mm	Opt75-CalcHigh	99.99	0.14	100	0.06	97.06	0.22	97.93	0.24
	Opt50-CalcHigh	99.99	0.13	99.93	0.11	98.33	0.23	98.41	0.21
	Opt40-CalcHigh	99.99	0.13	100	0.05	97.20	0.23	97.42	0.22
	Opt30-CalcHigh	99.88	0.16	96.93	0.27	95.90	0.27	98.53	0.21
	Opt20-CalcHigh	99.94	0.15	99.94	0.14	96.34	0.26	97.42	0.22
	Opt10-CalcHigh	99.60	0.16	100	0.12	95.53	0.30	95.73	0.31
criteria: 1%, 1mm	Opt75-CalcHigh	98.63	0.26	100	0.11	92.24	0.41	94.57	0.37
	Opt50-CalcHigh	98.58	0.25	99.93	0.15	92.88	0.40	96.49	0.32
	Opt40-CalcHigh	99.17	0.24	100	0.10	92.51	0.42	95.70	0.35
	Opt30-CalcHigh	97.03	0.29	95.74	0.34	90.40	0.48	96.12	0.33
	Opt20-CalcHigh	98.77	0.26	99.88	0.18	91.60	0.46	94.73	0.35
	Opt10-CalcHigh	97.09	0.29	98.92	0.16	88.48	0.51	92.14	0.49

for the target volume and OARs. Table 4.2 compares the dose distributions using the Gamma analysis. Typically, a clinical threshold of about 90% success for a 3%/3mm criterion is required to consider two dose distributions clinically equivalent [137]. Considering 3%/1mm criteria, it can be seen that more than 95.50% of voxels passed the Gamma analysis which confirms that the dose distributions are clinically equivalent. It should be noted that the clinical goals were met in all cases and for all levels of CT dose.

An alternative way to compare the optimized plans can be achieved by comparing the energy layers and their corresponding relative weights for the plans optimized on LdCTs (OptLow) with those of the standard-dose scan (OptHigh). The relative weight is normalized within each beam and the total relative weight sums up to 100%. Figure 4.4 represents the energy layers (X axis) and the relative weights (Y axis) for two beams in case 3 (the energy layers and the relative weights for other cases is presented in the Appendix A, Figure A3). It can be seen that there is a close agreement between the energy layers and their weight for the plans optimized on the standard-dose and LdCTs, suggesting the plans yield similar dose distributions.

Investigating the regions where the estimated dose differs from the ground truth suggests that the majority of the error occurs in those regions where the optimizer has the flexibility to modify the plan. Figure 4.5 shows the dose

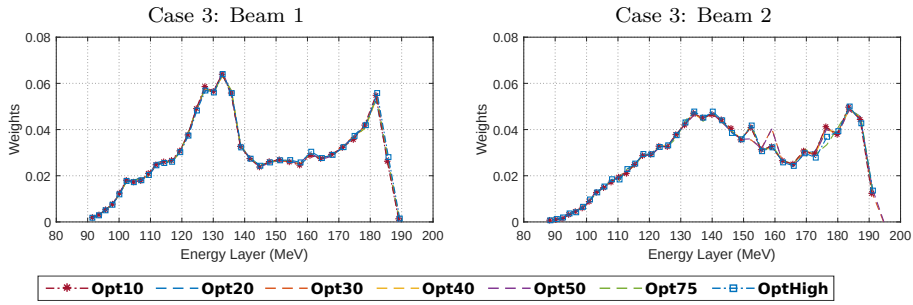

Figure 4.4: Representation of the energy layers and the corresponding relative weights for two beams in case 3. The plans were reoptimized on the standard-dose and LdCTs separately.

difference between Opt10-CalcHigh and OptHigh-CalcHigh and the corresponding Gamma index map for each case. It can be seen that the majority of the error occurs outside of the target volumes. In fact, in all plans, the objective functions were defined to make a conformal dose in the target volumes (objectives: max and min dose, uniform dose) and to minimize the dose to the OARs (objectives: max and mean dose). The plans were optimized based on these objectives, therefore, the optimizer is insensitive to the dose in non-ROI and non-OAR regions and the dose difference is more likely to be higher in these regions.

4.3.2 WET estimation error

WET maps were calculated using openPR plugin which is a part of openREGGUI, an open-source image processing platform for APT. Wet maps were calculated along the lateral direction (corresponding to gantry angles of 270°) for cases 1 and 2 and along the antero-posterior direction (corresponding to gantry angles of 180°) for cases 3 and 4 to resemble the commonly used beam angle for each case. Figure 4.6 represents the WET maps acquired from the standard and low-dose CTs and the corresponding relative error for case 3 for different levels of CT dose (the WET maps for other cases can be found in the Appendix A, Figure A4). Table 4.3 reports the mean value of the relative and absolute error for WET maps. It can be seen that the relative and absolute error is smaller than 0.4% and 0.8 mm, respectively, confirming that the surviving noise after integration along the beam is small.

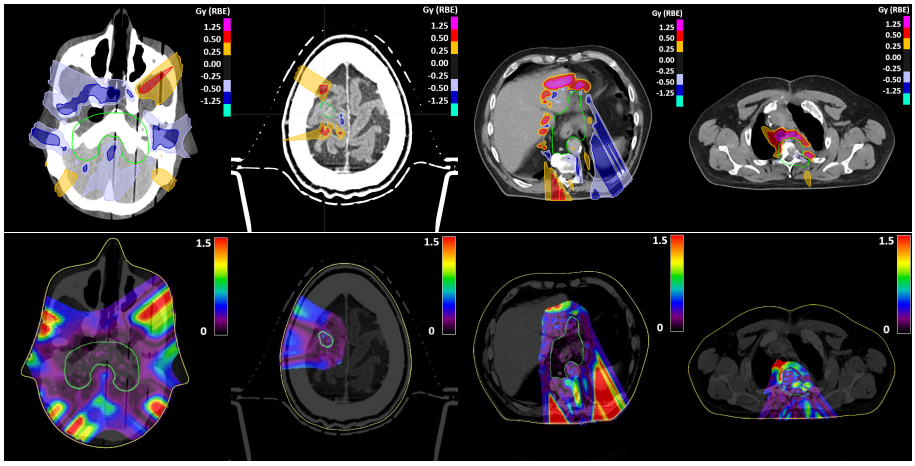

Case 1 Case 2 Case 3 Case 4

Figure 4.5: Representation of (first row) the difference between treatment dose acquired from OptHigh-CalcHigh and Opt10-CalcHigh and (second row) the corresponding Gamma index map for each case. The green contour represents the target volume. It can be seen that the majority of error occurs in non-ROI and non-OAR regions.

Table 4.3: Comparison of the WET maps estimated from the standard-dose and LdCTs using the mean value of the relative error (RE in %) and absolute error (AE in mm).

	Case 1		Case 2		Case 3		Case 4	
CT dose (%) ⇓	RE	AE	RE	AE	RE	AE	RE	AE
75% of ref dose	0.02	0.02	0.02	0.03	0.09	0.18	0.20	0.42
50% of ref dose	0.02	0.02	0.03	0.04	0.11	0.20	0.22	0.47
40% of ref dose	0.03	0.03	0.04	0.05	0.12	0.23	0.24	0.51
30% of ref dose	0.04	0.04	0.04	0.06	0.14	0.26	0.26	0.58
20% of ref dose	0.05	0.06	0.06	0.08	0.17	0.32	0.31	0.68
10% of ref dose	0.09	0.10	0.10	0.14	0.33	0.57	0.42	0.83

4.4 Discussion

The results show that reducing the CT dose does not have a significant effect on proton therapy dose estimation, even for the plans with non-robust optimization. Since robust plans (i.e. case 3) should be less sensitive to the

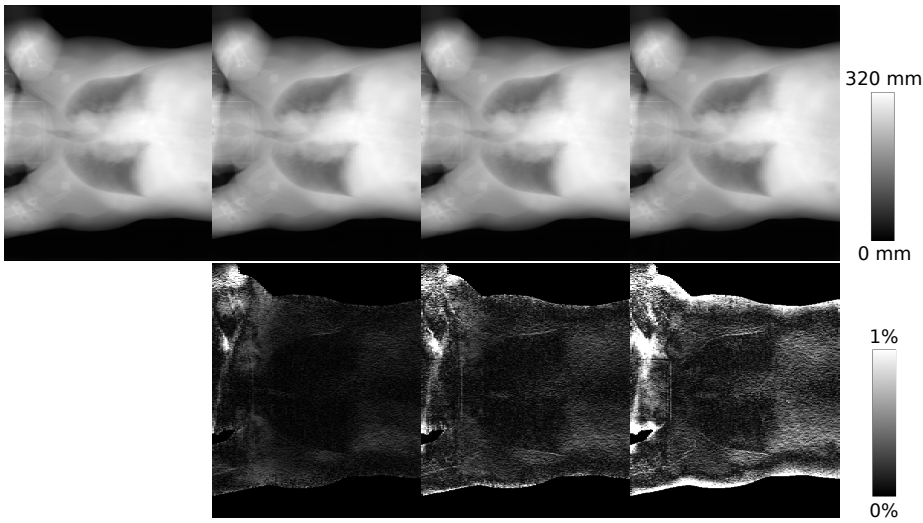

Figure 4.6: Representation of (first row) the WET maps calculated from the the standard-dose and LdCTs in case 3 and (second row) the corresponding relative error.

noise in the CT images, the plans with non-robust optimization (cases 1, 2, and 4) can be considered worst case scenarios. Therefore, the accumulated noise after integration along the beam does not adversely affect proton therapy dose calculations, even with strong dose reductions. The reason is that the CT protocols have been optimized for imaging small CT-number [HU] differences at a high spatial resolution, because they are clinically relevant. A much stronger noise suppression (and higher resolution) is required for visualizing these small HU differences, than for ensuring quantitative accuracy of the proton dose computations.

The results suggest the possibility of using LdCTs for dose calculation. The DVH curves and Gamma analysis indicate that the dose distributions acquired from the standard and low-dose CTs are equivalent. The Gamma passing rate is higher than 99.92% (3%,1mm) even after an aggressive dose reduction by a factor of up to 10, except for the LdCT with 10% of the reference dose in case 4. The dose calculation test is robust against other sources of variability and is a good representation of the effect of reducing CT dose. It can be seen that the mean of the Gamma value increased monotonically by lowering the CT dose.

The LdCTs can also be used for plan optimization, however, a larger error was observed. It could be due to several reasons: first, the CT noise slightly

affected the spot positions and therefore the energy layers associated with the spot positions. Second, the CT noise propagation may be more damaging during several hundreds of consecutive iterations than during a single dose calculation. For example, the optimization algorithm may attribute a higher weight to beamlets that happen to look better than they are due to noise. Third, the risk of ending up in a local optimum is higher when the CT is noisier.

Using a pencil beam engine eliminated the variation due to Monte Carlo simulation, however, there are other sources of variation, such as different initial conditions. In order to minimize these variations, the same experiment was repeated by using different optimization settings. For example, the plans were reoptimized without spot filtering to make sure that no spot or energy layer will be removed during plan optimization. Spot filtering ensures that all spots are deliverable by removing spots with weights below the minimum deliverable monitor units (MUs). The absolute dose difference between OptLow-CalcHigh and OptHigh-CalcHigh decreased by a factor of 2 for all levels of LdCTs after reoptimizing the plans without spot filtering. In another experiment, the spot spacing for planning optimization was set to 0.5, instead of the default value of 1. The spot spacing defines the inter-spot distance, where a lower value decreases the inter-spot distance and therefore more spots would be engaged in a plan. It was seen that after increasing the number of spots and avoiding spot filtering the absolute dose difference was reduced by a factor of 4. The results proved that the plan optimization error is also affected by other sources of variability.

The fact that the Gamma passing rate hardly increases with increasing dose reduction in Table 4.2 supports the assumption that the optimized plan is affected by other variabilities. It can be seen that optimizing on LdCTs has a constant adverse effect on the Gamma passing rate of about 2% in case 1, 8% in case 3, and 5% in case 4 considering 1%,1mm criteria. Because this error seems independent of the noise reduction, we attribute a portion of this error to arbitrary behavior of the optimization where, for example, a slight change of initial conditions or a small change in one iteration may lead to unpredictable changes in the optimized results. Thus, we believe that the observed error is dominated by other sources of variability, implying that the effect of the CT noise increase has a negligible effect on the plan optimization.

Even though the error of plan optimization is larger than the dose calculation error, the LdCTs can still be used for plan optimization due to the fact that OptLow-CalcHigh met all the clinical goals for all levels of LdCTs. The optimized plan on LdCT might differ from the ground truth but it does not necessarily mean that the optimized plan is incorrect. Plan optimization is not a single solution problem and there could be several plans that meet the clinical goal.

The WET maps also indicate that the accumulated error after integration along the beam is small. The relative error is smaller than 1% in the majority of regions except in high attenuated regions such as dental fillings. However, the dental filling region will be usually avoided for beams to travel through. There are two reasons for the higher error in these regions. In the high attenuated regions, the number of detected photons by the CT scanner can become very small, triggering the application of a smoothing filter by the acquisition software to suppress the CT noise. This smoothing filter results in the underestimation of the HU for high attenuated regions. In addition, the CT number-to-SPR conversion is piece-wise linear, therefore, the estimated proton stopping powers are a non-linear function of the reconstructed Hounsfield unit. A zero mean noise will be converted to non-zero mean noise by such non-linear conversion and a systematic error is expected, especially in those points where the slope of the curve varies a lot [138]. This nonlinearity along with the higher level of CT noise in the LdCTs resulted in the higher error.

The effect of reducing CT imaging dose on the delineation of the target volumes and OARs has not been discussed in this work. In APT, however, the generation of reliable new contours, together with their verification and approval for repeated images is crucial [81], yet, its implementation in clinical practice is challenging [139]. Alternatively, simplified approaches such as dose restoration [79, 80, 81] can be employed to facilitate the online adaptive workflow. Dose restoration aims to detect density changes along the beam path to reproduce the planned dose based on the new repeated images. In proton therapy, dose restoration is applicable when the change in anatomy is small and rigid mapping of contours from the previous CT image to the CT of the day is accurate. It generates a new restored plan by adapting proton beam energies and spot weights without involving contour adjustments in the workflow. This makes this work highly relevant for dose restoration approaches [140, 80, 81] where the repeated CTs are used for plan adaptation without involving contour adjustments.

It was shown that the LdCTs are good enough for dose calculation but the noise might become problematic for the verification and correction of lesion and organ contours. Therefore the dose reductions may have to be less aggressive if the CT images are (also) used for organs and targets contouring tasks. The effect of reducing CT dose on image contouring will be investigated in future research. For the lesion and organ contouring, contouring experts will be asked to correct existing contours or define new contours, both on the standard-dose images and the reduced-dose images. In addition, an advanced convolutional neural network-based image denoising method [141] is being developed to suppress the CT noise for organs contouring tasks. The in-house LdCT simulator will be used to generate the standard-dose and low-dose pairs for training the model. The LdCTs can then

be denoised for organ delineation tasks.

4.5 Conclusion

We hypothesized that the signal-to-noise ratio provided by conventional CT protocols is higher than needed for proton therapy dose estimation. To address this question, LdCTs were simulated from an existing standard-dose scan with a previously validated method. The LdCTs were used for dose estimation and the results were compared with that on the standard-dose scan. The results based on a phantom and three patient cases suggested that an aggressive CT imaging dose reduction by 90% does not have a significant effect on proton dose estimation. The DVH of the doses estimated from the standard-dose and LdCTs were on top of each other. The Gamma analysis also showed that the doses are clinically equivalent. The WET maps calculated from the LdCT images were in close agreement with that of the standard-dose CT.

Acknowledgments

Gilles Defraene is postdoctoral fellow of the Research Foundation Flanders (FWO, project 1292021).

5

Low-dose 4DCT for proton therapy treatment planning of esophageal and lung cancer patients

Abstract

In order to practice daily adaptive proton therapy, a new CT image acquisition must be performed at every treatment session. Treatment typically involves around 30 treatment sessions. The total dose associated with these CT scans is significant, in particular for esophageal and lung cancer patients where a 4DCT is performed to account for respiratory motion. Thus, minimizing exposure as low as reasonably achievable is crucial. Our preliminary results showed the possibility of using low-dose CT (LdCT) images for proton therapy dose calculation and plan optimization. In this study, we aim to assess the effect of reducing CT imaging dose on proton therapy dose calculation, plan optimization, and delineation of target volumes and organs at risk based on the planning 4DCT of four esophageal and thirteen lung cancer patients. The results show that LdCT can be used not only for proton therapy dose calculation and plan optimization but also for the delineation of target volumes and organs at risk. The gamma passing rate (3%/3 mm) is 100% and above 97% respectively for the doses re-calculated and optimized on LdCTs after reducing the CT imaging dose by

90%. Furthermore, a strong overlap between the contours based on the low-dose and standard-dose CT was observed where the error is smaller than inter-observer variability. However, a lower feeling of certainty was reported for the manual delineation of target volumes on the LdCT, therefore, less dose reduction should be implemented in clinical routine if manual delineation is involved.

5.1 Introduction

Proton therapy is a highly conformal radiotherapy technique which employs proton beams to destroy cancer cells. Compared to photons, proton beams offer a more accurate dose delivery to the target volume and significantly mitigate the toxicity of surrounding critical structures in "ideal conditions". However, proton treatment plans are sensitive to anatomical changes during the course of fractionated radiotherapy. Even a slight change in the density of tissue in the beam path can affect the radiological path length, resulting not only in overshooting or undershooting in target volumes but also in increased dose to the surrounding healthy tissues [142, 143].

Anatomical variations can occur during the course of treatment due to tumor shrinkage, weight loss, organ motion, variation in organ filling, etc. These changes can significantly impair the physical advantages of proton beams [125]. In fact, anatomical changes over the course of treatment are one of the largest and least predictable sources of uncertainty in proton therapy [35]. Adaptive approaches, e.g. daily adaptive proton therapy, can be employed to minimize range uncertainties in the presence of anatomical variations. Adaptive approaches employ a closed-loop imaging system to systematically detect changes in patient anatomy and adjust the plan accordingly [39].

Proton therapy treatment planning requires a volumetric image of the patient, first, to precisely delineate anatomical structures such as target volume and OARs and, second, to calculate particle stopping-power ratios (SPRs). In the current clinical workflow, CT images are considered the best imaging modality that provides accuracy for SPR calculation [35]. Using an MRI image would increase the range uncertainty of the proton beam. On the other hand, the image quality of CBCT is typically lower than that of the in-room CT. In-room CT provides 3D images with similar quality to those of the planning CT images which could make it the most practical modality for adaptive proton therapy application [47]. To this end, a diagnostic-quality CT scan directly before each treatment session would be paramount in order to exploit the full potential of proton therapy by allowing accurate dose calculation and subsequent plan adaptation.

The need for a new CT image acquisition at every treatment session is

increasing. However, performing a new daily (repeated) CT scan comes at the cost of substantial additional accumulated patient dose, especially if a 4DCT scan is required. The cumulative effective dose from the imaging system can sometimes exceed 100 mSv for patients who undergo repeated CT examinations [59, 60], sparking concerns about the potential lifetime radiation-related cancer risk. This is contrary to the primary goal of proton therapy which is minimizing the radiation dose to healthy tissues.

Reducing CT imaging dose by performing LdCT and thereby decreasing the potential risk of radiation dose to patients is desirable, however, there is a compromise between the radiation dose and image quality. A lower imaging dose results in a lower signal-to-noise ratio and in reduced image quality. We believe that CT imaging dose can be sacrificed without having an adverse effect on proton therapy treatment planning. Our preliminary results [144] (Chapter 4) indicated the possibility of using LdCT for accurate proton therapy dose calculation and plan optimization where the estimated doses based on LdCTs, with up to 90% reduction in CT imaging dose, were clinically equivalent to doses estimated based on the standard-dose CTs.

The adaptive workflow established by Nenoff et al. [133] at the Paul Scherrer Institute (PSI, Switzerland) also considered a LdCT acquisition protocol. Using an anthropomorphic phantom, daily repeated CTs were performed on in-room CT-on-rails by considering two acquisition protocols: the clinical standard protocol (120 kVp, quality reference mAs: 320, care dose, pitch 0.6, rotation time 1s) and a LdCT protocol (120 kVp, quality reference mAs: 20, care dose, pitch 1, rotation time 0.5s). The $CTDI_{vol}$ (volume CT dose index) of the LdCT protocol was roughly one-third of the standard protocol. A comparison was made between the dose distributions calculated on the LdCT and the standard-dose CT, indicating the possibility of using the LdCT protocol for daily adaptive proton therapy.

Nesteruk et al. [145] evaluated the impact of LdCT protocols on daily adaptation using patient cases. In their study, LdCTs (by a factor of up to 40 with respect to the standard-dose CT) were simulated by adding Gaussian noise to the standard-dose CT. The contours were propagated from the planning CT to the CT-of-the-day (simulated LdCT) by employing deformable image registration. The plan adaptation was then performed by adjusting the weights of the beamlets based on the dose-influence matrix (dose-influence matrix represents the dose distribution received at each voxel from each beamlet per unit fluence). The contours based on LdCT were almost identical to those of the standard-dose CT (Dice score above 0.98). The dose distributions recalculated on LdCT and the standard-dose CT (using the Monte Carlo engine) were clinically equivalent, with the gamma pass rates (2%/2 mm) over 99.95%. It should be noted that different acquisition protocols are in use by different centers. Compared to our study,

the $CTDI_{vol}$ values reported for the standard-dose CT protocols in the paper by Nesteruk et al. [145] are higher than those in our study. The $CTDI_{vol}$ values corresponding to LdCT protocols after reducing the CT dose to a factor of 40 in this paper are consistent with ours after reducing the imaging dose to a factor of 10.

The treatment planning process starts with the delineation of anatomical structures. Following that, a set of dose objectives and constraints are defined for target volumes and OARs. After specifying the number of beams and their direction, the objectives and constraints can be defined for target volumes and OARs. A treatment planning system is then employed to establish machine parameters that minimize the objective function while obeying the constraints. Once the optimization process is complete, the plan can be evaluated by assessing the fulfillment of clinical goals for target volumes and OARs. Consequently, the accurate delineation of target volumes and OARs is a fundamental prerequisite for defining a high-quality proton plan. Volume delineation is a source of potential inaccuracy in radiotherapy [146], which might be affected by the higher level of CT noise on LdCT. However, in our previous study [144] (Chapter 4), the effect of CT imaging dose reduction was examined without involving contour adjustment.

Contours can be propagated from the planning CT to the repeated CT using image registration. It has been shown in previous studies [15, 145] that CT noise does not significantly affect contour propagation. Alternatively, anatomical structures can be delineated manually or with the aid of auto-segmentation software. This chapter aims to assess the effect of reducing CT imaging dose on the delineation of target volumes and OARs, as well as proton therapy dose calculation and plan optimization for 4DCTs.

This chapter focuses on lung and esophagus cases. This is due to several reasons: lung and esophageal cancer are ranked as the first and seventh cause of cancer incidence worldwide [147]. Approximately, 2.1 million new lung cancer cases (1.8 million deaths) and 572,000 new esophageal cancer cases (509,000 deaths) are predicted in 2018 worldwide [147]. There is a growing body of evidence demonstrating potential clinical advantages of proton therapy for lung [148, 149, 150, 40] and esophageal [151, 152, 153, 154] cancer. In addition, the target volumes are highly prone to intra- and inter-fractional changes in esophageal [154] and lung cancer, therefore, plan adaptation through the course of treatment is of utmost importance. Moreover, a 4DCT is required to define the treatment plan for lung and esophageal cancers. Minimizing the CT imaging dose for 4DCT is crucial. This is due to the fact that the effective dose from a 4DCT is approximately four to ten times higher than that from a 3DCT [82, 83] which makes daily 4DCT acquisition almost impossible.

The rest of this chapter is structured as follows. The proposed framework

to quantify the effect of reducing CT imaging dose on the delineation of OARs and target volume is described in Section 5.2.1 and Section 5.2.2, respectively. Section 5.2.3 discusses the possible approaches to quantify the effect of reducing CT dose on proton therapy dose calculation and plan optimization. Experimental results are presented in Section 5.3, followed by a discussion in Section 5.4. Finally, some concluding remarks are made in Section 5.5.

5.2 Materials and Methods

In order to quantify the effect of reducing CT imaging dose on proton therapy treatment planning, the standard-dose CT and the corresponding LdCTs are needed. The in-house LdCT simulator [134] (Chapter 3) was employed to generate synthetic LdCTs (with a gradual reduction in imaging dose) by adding an appropriate amount of position-dependent and correlated noise to the standard-dose scan. In the first step, the LdCT simulator was calibrated for different scanners, as described in Appendix B. Performing several phantom studies on the different scanners using different acquisition protocols confirmed the accuracy of the developed tool in generating realistic LdCTs [113, 155, 156, 134]. The texture and magnitude of the simulated LdCTs matched measurements in both the image and sinogram domains. This tool enables an accurate, reliable, and patient-dependent assessment of the effect of reducing CT imaging dose.

The plan can be redefined based on these simulated LdCTs. Comparing the results with that of the standard-dose CT can quantify the effect of reducing CT imaging dose on different tasks in proton therapy treatment planning. The rest of this section discusses the proposed framework to evaluate the possibility of using LdCT for the delineation of OAR and target volumes as well as for the proton therapy dose calculation.

5.2.1 Delineation of OARs

Accurate delineation of OARs is essential for accurate proton therapy planning. The delineation of OARs can be performed manually, yet it is very time-demanding (up to two hours [157]) and prone to observer variability. There is a growing body of evidence showing that inter- and intra-observer variability can be reduced by using atlas-based segmentation [158], deep learning-based contouring [159], auto-contouring software, and attending live contouring workshops [160, 161].

Manual delineation can be replaced by auto-contouring softwares not only to reduce inter- and intra-observer variability but also to speed up the planning process. This is highly relevant for daily adaptive proton therapy regimens

where a new CT will be acquired every day and the plan adaptation needs to be done in a few minutes. Nevertheless, the automatic segmentations must still be corrected or approved manually.

In this study, syngo.via RT Image Suite [Siemens Healthineers] is employed for the automatic delineation of OARs on the standard and LdCTs. For esophagus cases, 6 OARs (Heart, kidney, liver, lung, spinal cord, and spleen) are delineated. Brachial plexus and esophagus are added to this list for lung cases. The automated contours were then manually reviewed, corrected, and approved by an expert using MIM Software Inc., OH, US. The effect of CT dose reduction can then be quantified by comparing the contours based on the LdCTs with those of the standard-dose image.

The overlap between OARs (and also target volume in Section 5.2.2) delineated on the standard-dose and LdCT images is quantified using Dice Similarity Coefficient (DSC) and Hausdorff Distance (HD). The DSC measures volumetric overlap between volume A and B. Mathematically, it can be written as:

$$DSC = \frac{2 \mid A \cap B \mid}{\mid A \mid + \mid B \mid} \tag{5.1}$$

The value of DSC is always between 0 and 1. It gets closer to 1 as the overlap between the two contours increases.

HD measures the surface-based distance between two contours. It represents the largest distance between two structures [162] and is defined as follows to measure the distance between contours A and B:

$$HD(A, B) = \max(h(A, B), h(B, A)) \tag{5.2}$$

where

$$h(A, B) = \max_{a \in A} \min_{b \in B} \|A - B\| \tag{5.3}$$

where a and b represent the contour points. HD is highly sensitive to even a single outlier point. HD-95 can be used instead which is more robust and eliminates the impact of a very small subset of the outliers. HD-95 represents the largest distance that falls within the 95% confidence interval for the set of distances in HD [163]. Throughout the rest of this chapter, HD-95 will be used to report the distance between two contours.

5.2.2 Delineation of target volume

Target volume delineation uncertainty is one of the dominant sources of uncertainty in radiotherapy as delineation uncertainties could contribute to systematic errors [164]. The effect of reducing CT imaging dose on the delineation of the target volume is assessed by manually delineating the target volume on the LdCTs and standard-dose CTs using MIM Software.

The target volume was manually delineated by a radiation oncologists, first, on the LdCTs with 10% of the standard imaging dose, then on LdCTs with 30% of the standard imaging dose, and finally on the standard-dose CT. Delineation sessions were separated by several weeks so that previous contours would not influence the delineator.

The target volume delineation protocol is based on the guideline proposed by Thomas et al [165]. For the delineation of the target volume in esophagus cases, the fluorodeoxyglucose positron emission tomography with integrated CT image (FDG-PET/CT) was first registered to the mid-ventilation phase of the planning 4DCT (with 10 breathing phases). This FDG-PET/CT image was acquired several days before the planning CT. The mid-ventilation phase of the planning 4DCT scan was used for the delineation of the gross tumor volume of the primary tumor (GTVp) and pathological lymph nodes (GTVn), the clinical target volume of the primary tumor (CTVp) and the nodes (CTVn). The total volume CTV (CTVtotal) was defined by adding CTVp and CTVn and by filling any possible gaps. The CTVtotal was then delineated on all respiratory phases using deformable image registration between each phase and then corrected manually. Finally, the internal clinical target volume (iCTV) was defined by the summation of all phases CTVtotal to account for respiratory motion [165, 166] and then projected on the average CT for planning. The effect of CT noise on the delineation of target volumes will only be investigated for esophagus cases. Due to time restrictions, lung cases have been excluded from the manual delineation of target volumes.

5.2.3 Dose calculation and plan optimization

LdCTs along with the standard-dose CTs were used for proton therapy dose calculation and plan optimization. The procedure is similar to the workflow described in Chapter 4 [144]. In the first step, the standard-dose CT is used to optimize the treatment plan (OptHigh) and to calculate the final dose (CalcHigh). OptHigh-CalcHigh is considered as the ground truth because it represents the closest approximation of the delivered dose to the patient from the optimal plan.

The effect of CT noise on proton therapy dose calculation and plan optimization is investigated separately. For the dose calculation error, the plan is first optimized on the standard-dose CT image (OptHigh) and the dose distributions are recomputed on the LdCTs (CalcLow) using the same optimized plan. For the plan optimization error, the plan is reoptimized separately on LDCTs (OptLow) and the final doses are recalculated on the standard-dose scans (CalcHigh). Dose distributions are then compared using the gamma analysis to quantify the effect of CT noise on proton therapy dose calculation (OptHigh-CalcLow vs OptHigh-CalcHigh) and plan optimization (OptLow-CalcHigh vs OptHigh-CalcHigh).

5.2.4 Patient cases

Planning CT scans of 4 esophageal and 10 lung cancer patients were used to investigate the possibility of using LdCTs for proton therapy treatment planning. All the patients were scanned with a routine clinical protocol on Siemens SOMATOM EDGE or DRIVE scanners [120 kVp] at the Radiation Oncology Department of the University Hospital of Leuven in Belgium. All patients provided written informed consent for the collection and for the anonymous use of their data for educational and research purposes.

The raw CT data of the planning CTs were collected prospectively and analyzed retrospectively. It should be mentioned that all these patients underwent photon treatment, therefore, a new realistic proton plan was defined for each case by an expert. Unfortunately, no proton patient was included in this study due to the limited number of adult patients undergoing proton therapy in our center.

Table 5.1 shows the standard acquisition protocol and the approximate effective dose received by the patients from the imaging system. The effective dose was computed using CT-Expo (version 2.5) in accordance with ICRP103 [167]. The average effective dose from planning CT was 23.7 $\pm$ 8 mSv. Assuming that a patient could undergo up to 30 treatment sessions, the average effective dose from daily CT images with the current clinical protocol could sum up to 700 mSv, increasing the risks related to radiation exposure.

5.3 Results

In the first step, LDCT scans with gradual reduction in the imaging dose (from 75% down to 10% of the tube load reported for the standard-dose CT) were simulated by adding synthetic noise to the standard-dose CT scan. The simulated scans were then reconstructed using Siemens offline reconstruction software [ReconCT 14.2.0.40998]. Figure 5.1 represents the standard-dose CT images (average image) and the corresponding simulated LdCTs with 10% and 30% of the standard imaging dose. As shown in Figure 5.1, the CT imaging noise increases by reducing the CT imaging dose, resulting in a poorer image quality.

5.3.1 Delineation of OARs

After reconstructing LdCTs, the average image was derived from the 4DCT images (with 10 breathing phases) and used for OARs delineation. The OARs were delineated automatically using syngo.via RT Image Suite for the standard-dose CTs and for the corresponding simulated LdCTs with 10%, 30%, and

50% of the standard imaging dose. The contours were then corrected and verified manually for each case. The auto-segmentation software successfully contoured the OARs on the standard-dose and low-dose CT images where minor corrections were made to the original contours. In total, 6 OARs (heart, kidney, liver, lung, spinal cord, and spleen) were delineated for esophagus cases. Figure 5.2 and 5.3 compare the delineations based on the LdCTs with those of the standard-dose CTs for esophagus cases (In Figure 5.2 - 5.10, different markers represent different cases). It can be seen that the error increases by lowering the CT imaging dose, however, the HD-95 (Figure 5.2) is smaller than 2.5 mm for

Table 5.1: This table reports the CT acquisition protocol and the approximate effective dose received by patients from the imaging system (acquisition of planning CT).

Cancer type	#Case	Eff. mAs (mAs)	Pitch	$CTDI_{vol}$* (mGy)	DLP* (mGy cm)	Eff. dose (mSv)
Esophageal	1	48	0.09	29.50	1261	20.5
	2	64	0.14	24.97	1295	22.6
	3	61	0.14	23.80	1189	21.6
	4	84	0.14	32.77	1769	29.2
Lung	5	50	0.14	19.56	931	17.7
	6	78	0.14	29.92	1238	21.0
	7	89	0.09	53.21	2136	37.6
	8	80	0.14	30.68	1264	21.8
	9	42	0.09	25.54	1168	18.2
	10	89	0.09	53.21	2199	38.0
	11	80	0.09	47.83	2073	34.2
	12	62	0.14	24.19	1112	16.9
	13	52	0.14	19.94	805	14.3
	14	35	0.09	21.29	744	14.8
	15	67	0.09	40.36	1539	28.7
	16	75	0.09	44.84	1708	31.7
	17	33	0.09	20.38	801	14.2

* $CTDI_{vol}$ (volume CT dose index) and DLP (dose-length product) values refer to 32cm body phantom.

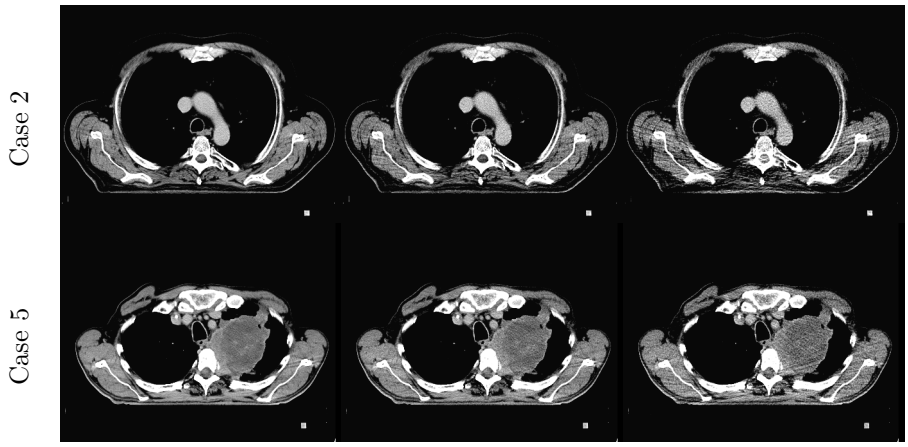

Figure 5.1: Representation of the standard-dose CT images and the corresponding simulated LdCTs for the esophagus (first row) and lung (second row) cases. It can be seen that the CT noise increases by lowering the CT imaging dose (window level: 50 HU, window width: 200 HU).

all the OARs, indicating a good agreement between contours based on LdCT and the standard-dose CT. The DSC (Figure 5.3) indicates that the OARs are well aligned where a DSC above 0.975 is observed for all OARs except for the spinal cord, which is above 0.93 after reducing the CT imaging dose by 90%.

For lung cases, the brachial plexus and esophagus were also delineated. Figure 5.4 and 5.5 compares the contours using HD-95 and DSC, respectively. The HD-95 (Figure 5.4) is smaller than 3 mm for all the OARs after 90% dose reduction, except for the brachial plexus which is around 6 cm in one case. The DSC (Figure 5.5) shows the same profile where it is above 0.94 for the majority of OARs except for the spinal cord (above 0.86) and the brachial plexus (above 0.50).

It should be noted that the majority of the corrections and also the dominant source of the error for OARs contouring occurred in the cranio-caudal direction. As already mentioned, delineated contours are based on the average image derived from the 4DCT images. Selecting the upper and lower limits of the OARs is a challenging task on the average image, even for manual delineation. This is due to the blurring effect which is caused by heart and respiratory motion.

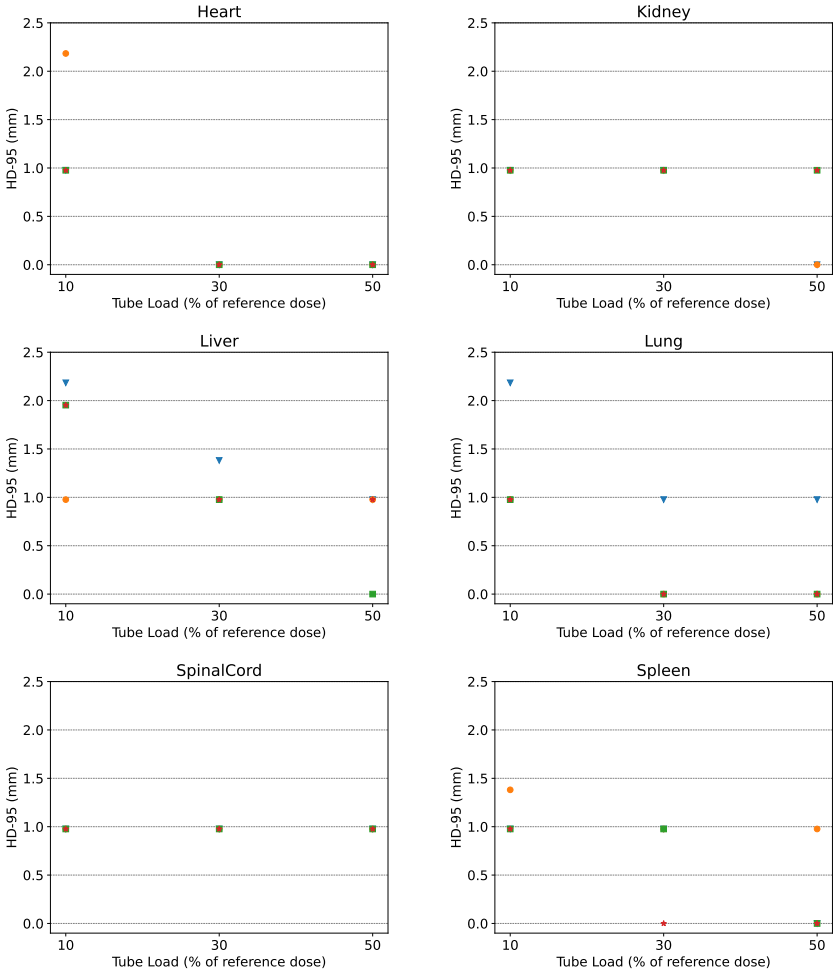

Figure 5.2: Comparing the distance (HD-95) between contours delineated on the LdCTs with those of the standard-dose CT for esophagus cases. HD-95 is smaller than 2.5 mm, showing strong agreement between the contours.

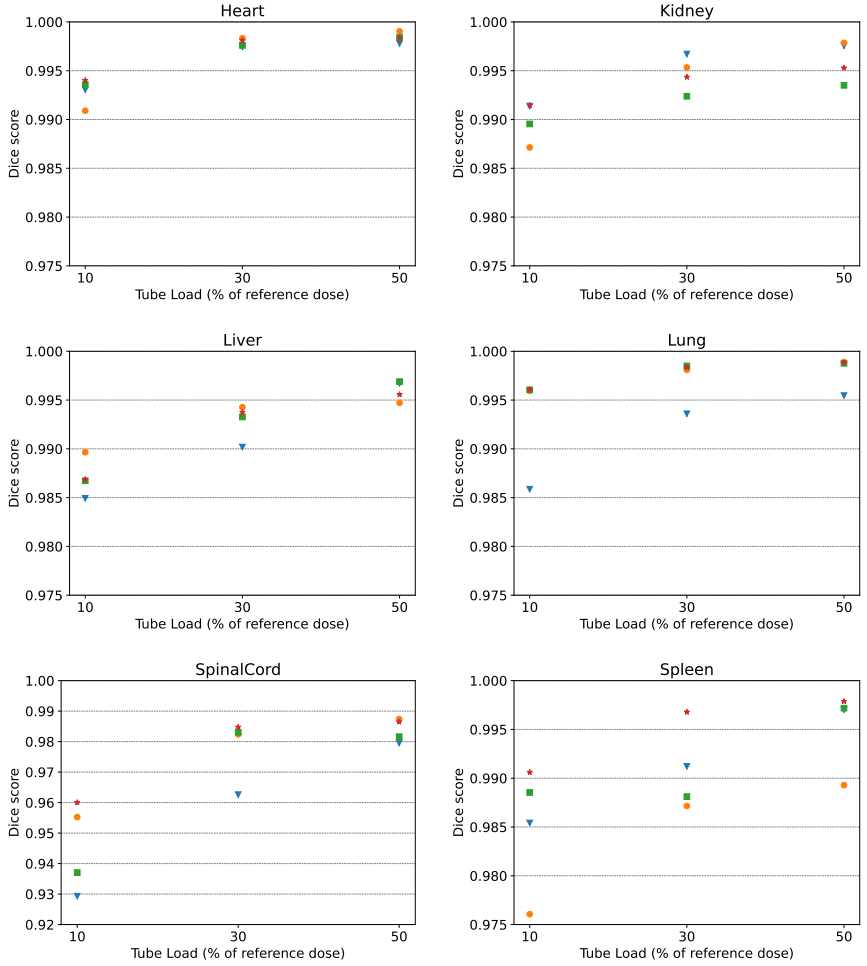

Figure 5.3: Comparing the overlap (DSC) between OARs delineated on the LdCTs with those of the standard-dose CT for esophagus cases. The DSC is above 93%, showing a strong overlap between OARs based on the LdCTs and those of the standard-dose image.

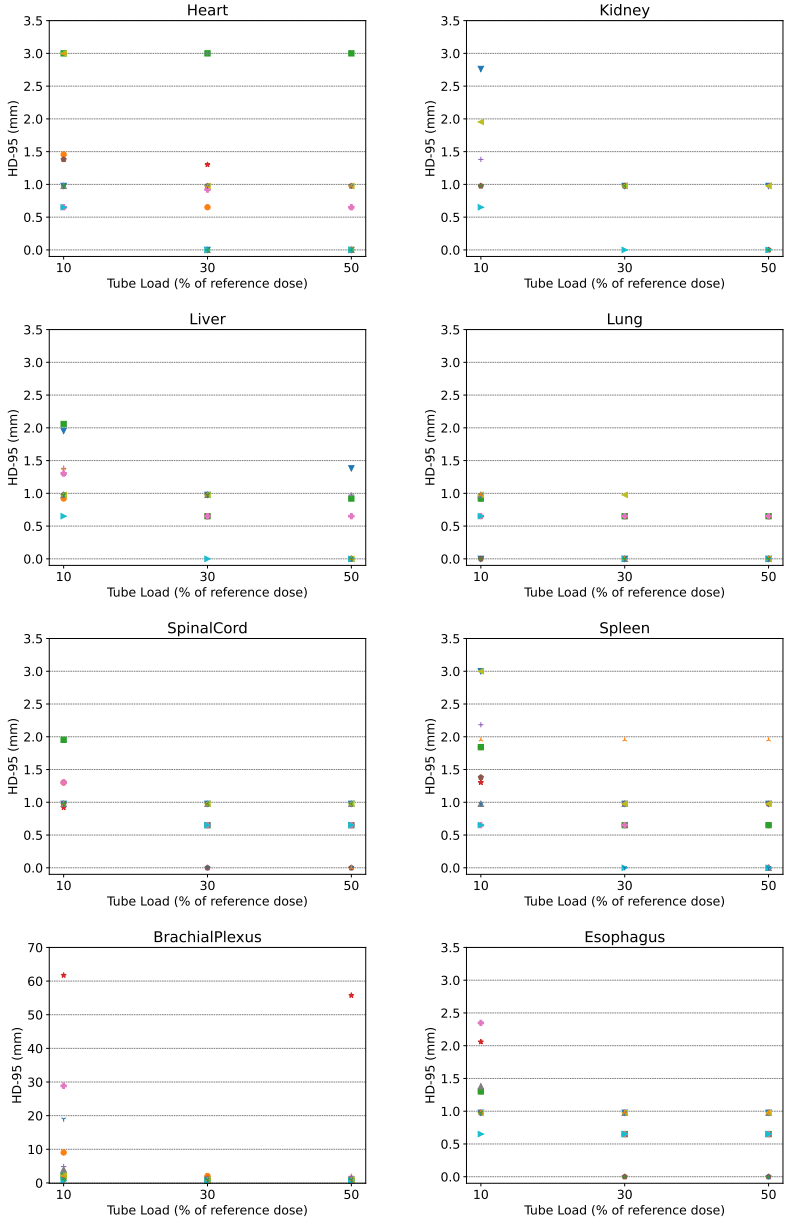

Figure 5.4: Comparing the distance (HD-95) between contours delineated based on the LdCTs with those of the standard-dose CT for lung cases. The distance is smaller then 3 mm (except for the brachial plexus), showing a good agreement between contours delineated on the LdCTs and the standard-dose CT.

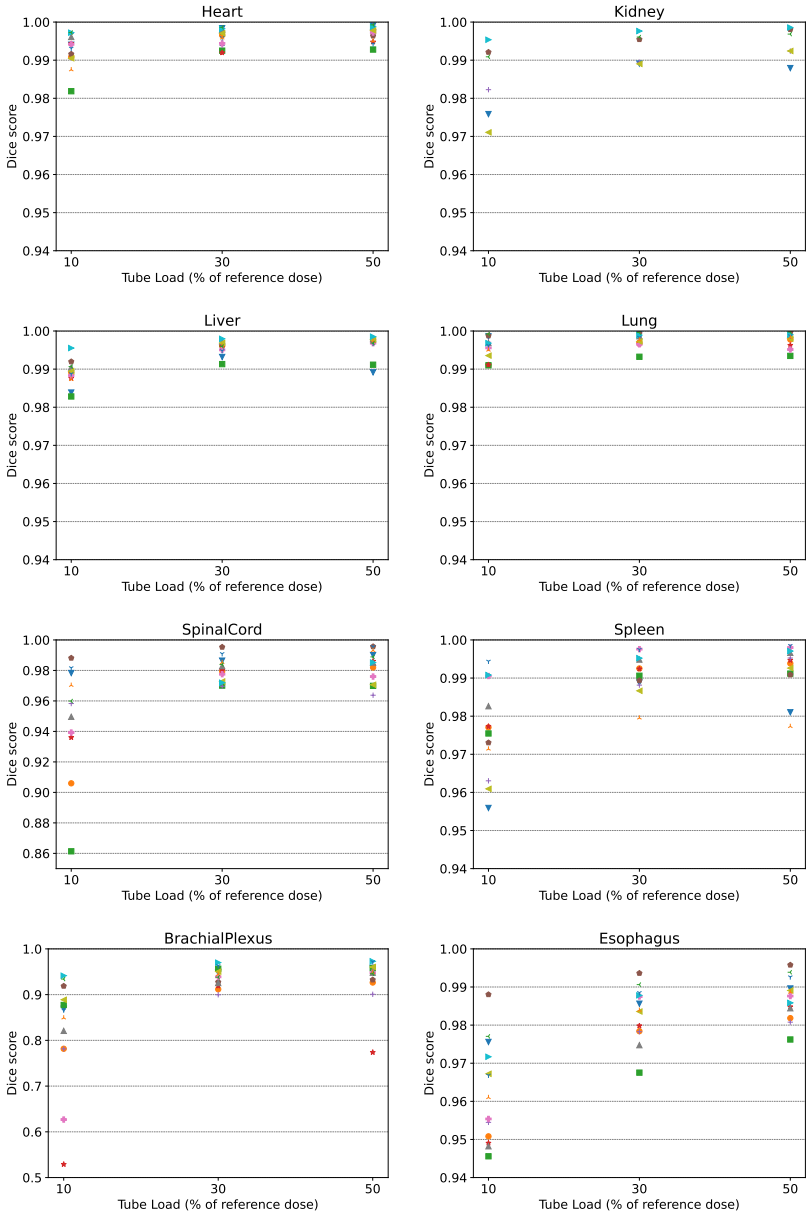

Figure 5.5: Comparing the overlap (DSC) between OARs delineated on the LdCTs with those of the standard-dose CT for lung cases. The results show a strong overlap between contours except for the brachial plexus in some of the cases.

5.3.2 Delineation of target volume

Delineation of target volumes was done manually for esophagus cases, first on LdCTs with 90% dose reduction (LdCT 10%), then on LdCTs with 70% dose reduction (LdCT 30%), and finally on the standard-dose CT. At least a two weeks gap between each session was maintained to ensure that the delineator was not biased by previous contours. As already mentioned, manual delineation is labor-intensive. For the lung cases, we could not find an expert to delineate the target volume. Therefore, this part only focuses on the esophagus cases.

The contours based on the LdCTs were compared with those of the standard-dose CT. The contours delineated on the standard-dose CT were also compared with those that were already defined in the clinic by the second observer for photon therapy. Comparing two independent delineations on the standard-dose CT helps to make a rough estimate of the inter-observer variability. Table 5.2 compares the target volume contours using DSC and HD-95. The DSC is above 0.77 and 0.80 for LdCT 10% and 30%. The HD-95 is less than 1.5 cm after reducing the CT imaging dose by 90%. It can be seen that the error caused by CT imaging dose reduction is in the same order as the inter-observer variability, suggesting the possibility of using LdCTs for target volume delineation. Figure 5.6 illustrates the target volumes delineated based on the standard-dose CT and the corresponding LdCTs for the cases with the highest disagreement.

Table 5.2: Comparing the target volume contours (iCTV) delineated on the LdCTs with those of the standard-dose CT using DSC and HD-95. The contours based on the standard-dose CT were also compared with the contours delineated by the second observer (on the standard-dose CT) to obtain a rough estimate of the inter-observer variability.

	#Case	LdCT 10%	LdCT 30%	Second observer
Dice Score	1	0.83	0.84	0.84
	2	0.84	0.90	0.84
	3	0.80	0.89	0.86
	4	0.77	0.80	0.50
HD-95 (mm)	1	12.0	12.0	8.7
	2	8.1	5.8	7.6
	3	15.0	6.0	9.0
	4	14.6	8.2	30.3

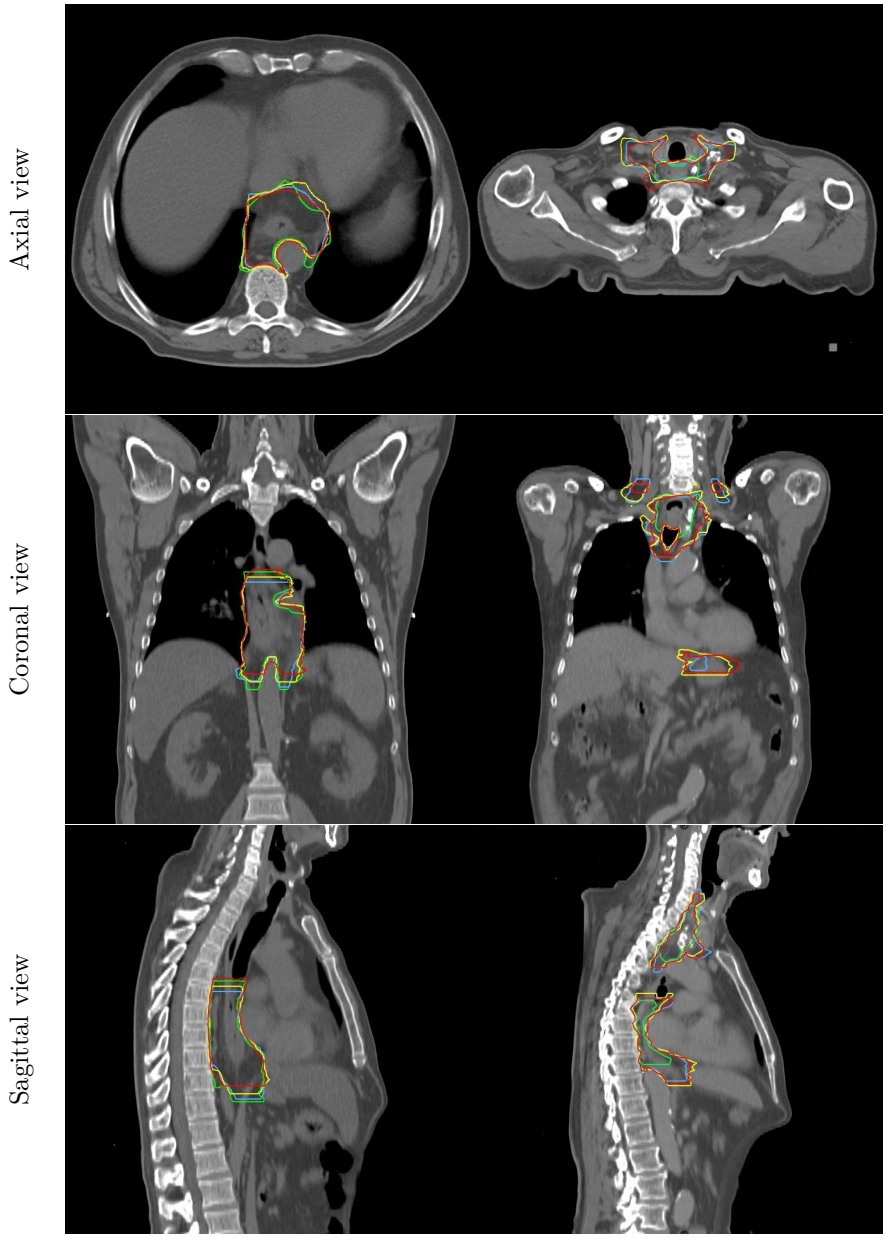

Figure 5.6: Illustration of target volumes delineated on the standard-dose CT (blue), LdCT 30% (yellow), and LdCT 10% (red). The green contours were delineated based on the standard-dose CT by the second observer and were used in the clinic for photon therapy.

5.3.3 Dose calculation and plan optimization

LdCTs, along with the standard-dose CT, were employed to assess the effect of CT imaging dose reduction on proton therapy dose calculation and plan optimization. As already mentioned, all the patient cases that were used in this study were treated with photon radiation therapy, therefore, a realistic proton plan was defined for each case. An IMPT plan was generated in RayStation V9B (for esophagus cases) and V11A (for lung cases) based on the average image derived from the standard-dose 4DCT as planning CT.

For esophagus cases, an IMPT plan with two posterior beams (150° and 180°) was defined. The prescribed dose was optimized on the Internal Clinical Target Volume (iCTV) using robustness settings of 7 mm setup error and 2.6% range error. For lung cases, an IMPT plan (with 2 or 3 beams) was generated and optimized on the PTV (non-robust optimization). Therefore, the plans for lung cases are more sensitive to the noise in the CT images. A Pencil Beam Scanning (PBS) technique was employed for proton dose delivery. Moreover, a pencil beam engine was used for dose calculation and plan optimization to eliminate additional variation caused by the statistical uncertainty of a Monte Carlo simulation.

Figure 5.7 compares OptHigh-CalcLow with the reference dose (OptHigh-CalcHigh) for esophagus cases, showing the effect of CT noise on the proton therapy dose calculation. The effective mAs of the standard-dose CTs vary for each case. Therefore, the gamma passing rates were plotted as a function of the percentage of the standard imaging dose and also as a function of the effective mAs. This facilitates the optimization of the acquisition protocol within and across different institutions by providing the required effective mAs as well as the percentage of imaging dose reduction. The dose calculation error increases when the CT imaging dose is reduced. Considering the 3%/1 mm criteria, the gamma passing rate is around 100% for all the cases after 90% CT imaging dose reduction, except for case 4. In case 4, the gamma passing rate is 100% after 70% dose reduction, but the gamma passing rate is respectively around 99.5% and 93.5% for the LdCTs after 80% and 90% dose reduction. For lung cases, represented in Figure 5.8, the the gamma passing rate is around 100%, after CT imaging dose reduction of up to 90%, showing a strong agreement between doses calculated on the LdCT and the standard-dose CT.

Simulated LdCTs were also used for plan optimization but the final doses were recalculated on the standard-dose CT. Figure 5.9 and 5.10 compare the plans optimized on the LdCTs (OptLow-CalcHigh) with those of the standard-dose CT (OptHigh-CalcHigh) for the esophagus and lung cases, respectively. Compared to the dose calculation test, a larger error is expected for the plan optimization test. This is due to the fact that this test is affected not only by CT noise but also by other sources of variability. Nevertheless, considering the 3%/3 mm criteria, the gamma passing rate is always above 95% for all the cases

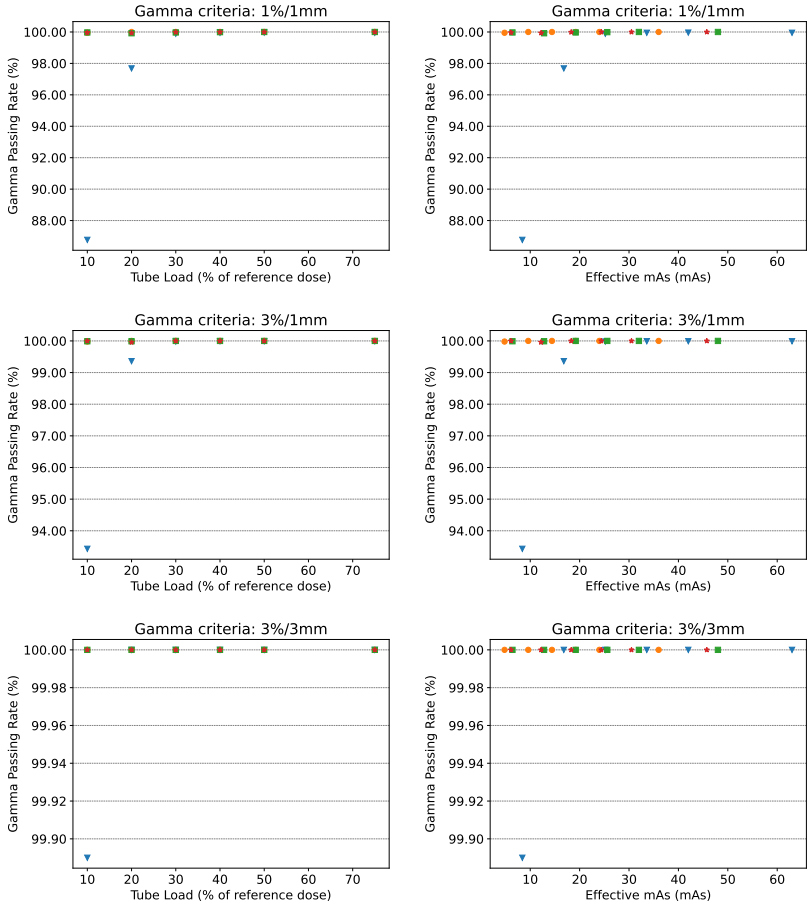

Figure 5.7: Comparison of the doses calculated based on the LDCTs with those of the standard-dose CT for esophagus cases using the gamma analysis. This test quantifies the effect of reducing CT imaging dose on proton therapy dose calculation (OptHigh-CalcLow vs OptHigh-CalcHigh). Using LDCTs for dose calculation results in doses similar to the ground truth.

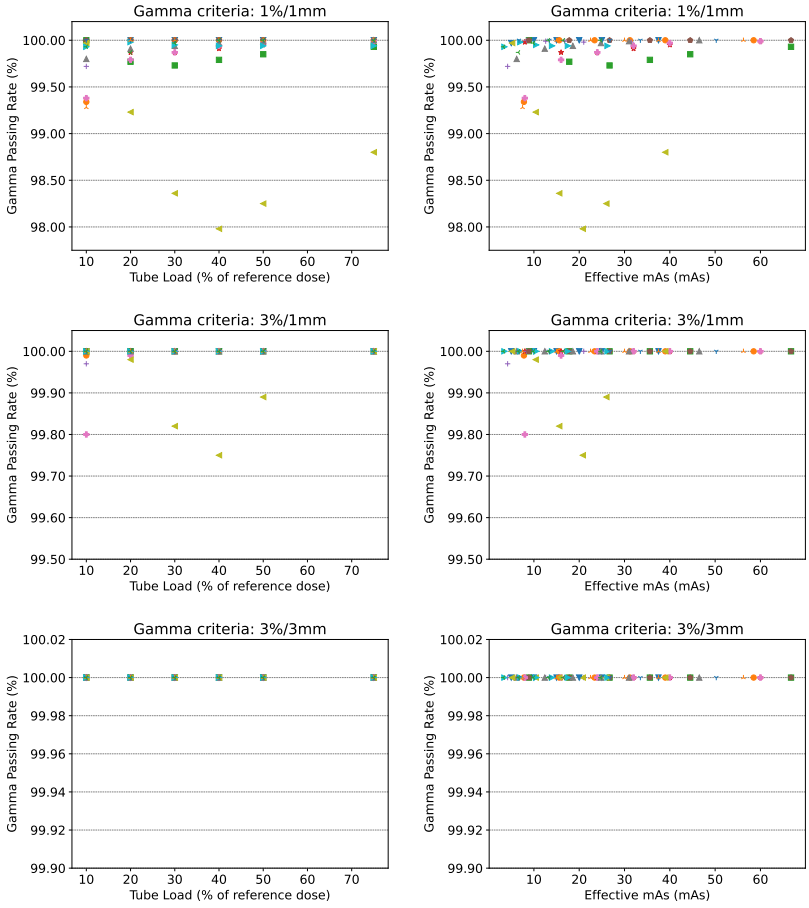

Figure 5.8: Comparison of the doses calculated based on the LDCTs with those of the standard-dose CT for lung cases using the gamma test. This test quantifies the effect of reducing CT imaging dose on proton therapy dose calculation (OptHigh-CalcLow vs OptHigh-CalcHigh). Using LDCTs for dose calculation results in doses similar to the ground truth.

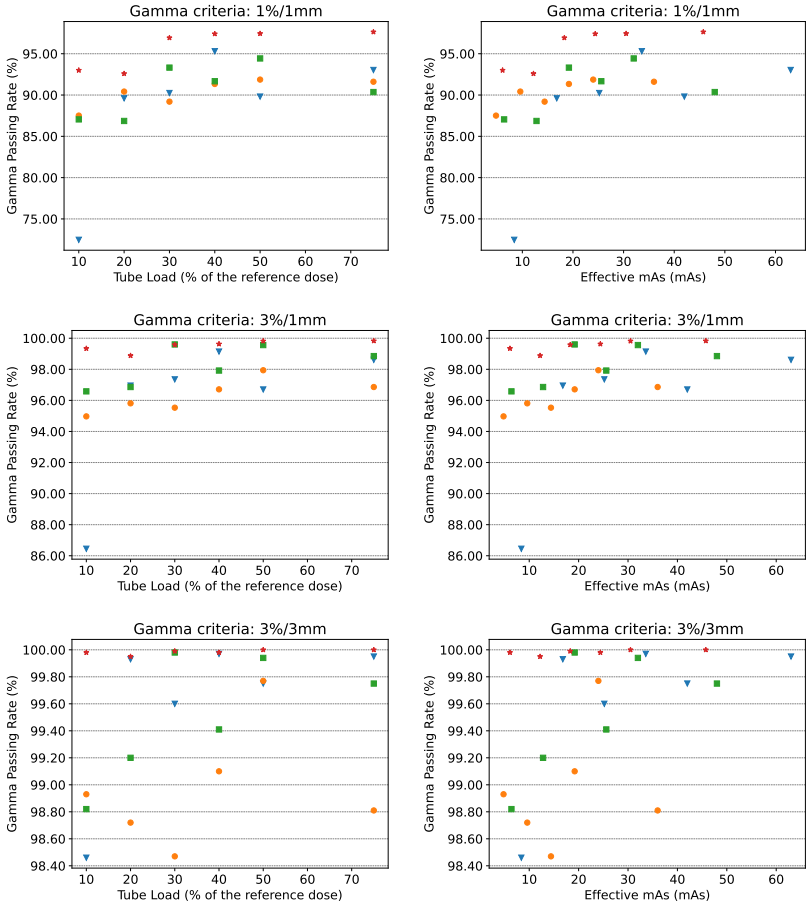

Figure 5.9: Comparison of the plans optimized on the LDCTs with those of the standard-dose CT for the esophagus cases using the gamma test. This test quantify the CT noise on proton therapy plan optimization (OptLow-CalcHigh vs OptHigh-CalcHigh).

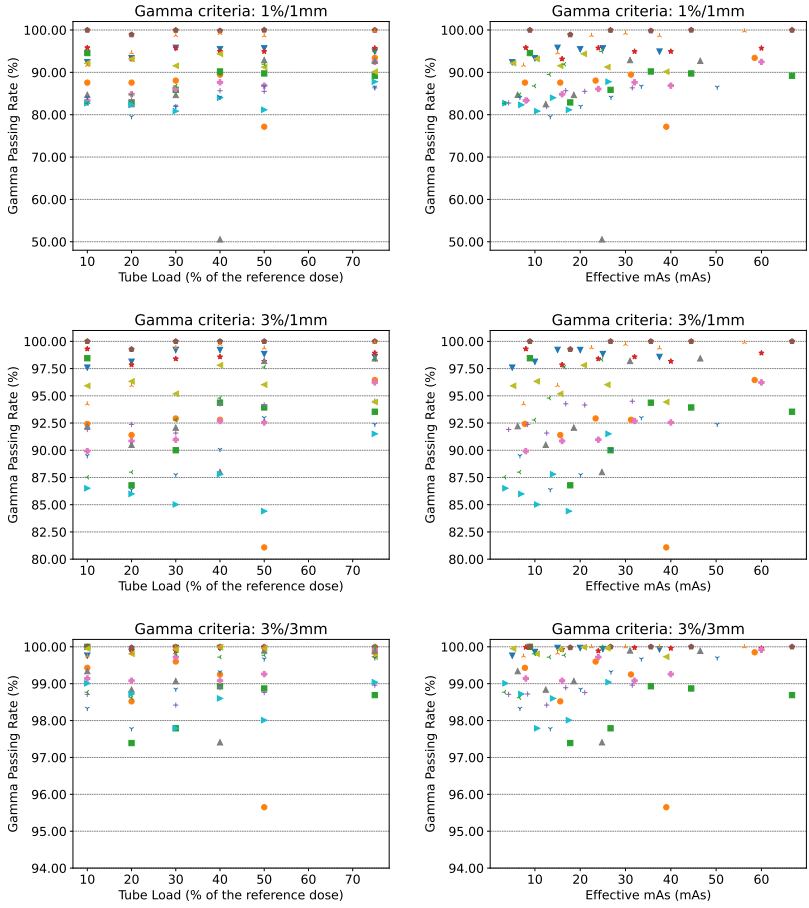

Figure 5.10: Comparison of the plans optimized on the LDCTs with those of the standard-dose CT for the lung cases using the gamma test. This test quantify the CT noise on proton therapy plan optimization (OptLow-CalcHigh vs OptHigh-CalcHigh).

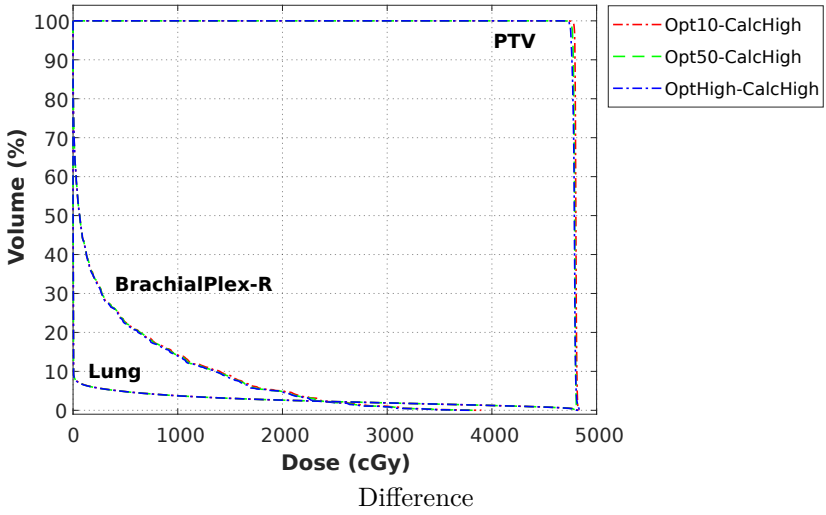

Figure 5.11: Comparison of the DVHs for the target volume and OARs based on the plans optimized on the standard-dose CT and LdCTs to assess the effect of reducing CT imaging dose on plan optimization.

which is above the required 90% threshold to consider two dose distributions clinically equivalent.

Figure 5.11 uses the DVH analysis to compare the plans optimized based on the LdCTs with that of the standard-dose CT for one of the cases with the lowest gamma passing rate (case 14: the cyan triangle in Figure 5.10). Accordingly, the DVHs are well aligned for the target volume and OARs (as defined in Figure 5.12(a)), indicating that the plans based on LdCTs and the standard-dose CT are clinically equivalent. Figure 5.12 illustrates the dose based on the standard-dose CT (OptHigh-CalcHigh), the dose based on LdCT 10% (Opt10-CalcHigh), the difference between them, and the line dose for case 14. The line dose represents the dose across the dose line as defined in Figure 5.12(a). As can be seen, the plan based on LdCT 10% delivers a conformal dose to the target volume which is in close agreement with the dose based on the standard-dose CT. In addition, a large portion of the error occurs outside of the target volume and OARs where the optimizer is more insensitive to the dose. Furthermore, the effective mAs reported for the standard-dose CT in case 14 is 35 mAs, which is among the lowest reported for standard-dose CTs. This accounts for the larger error observed in the plan optimization test for case 14.

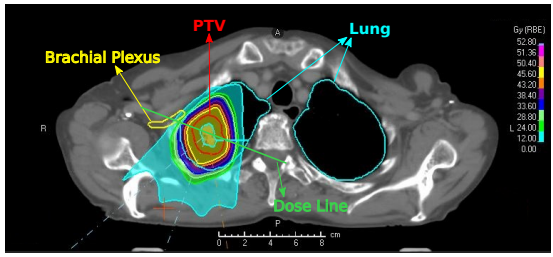

(a) OptHigh-CalcHigh

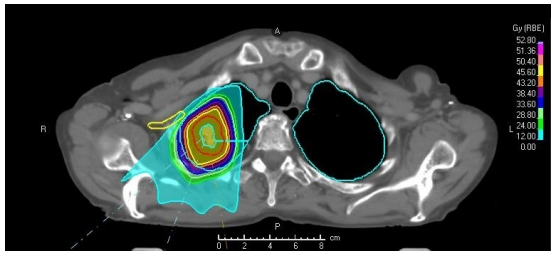

(b) Opt10-CalcHigh

(c) Difference: Opt10-CalcHigh - OptHigh-CalcHigh

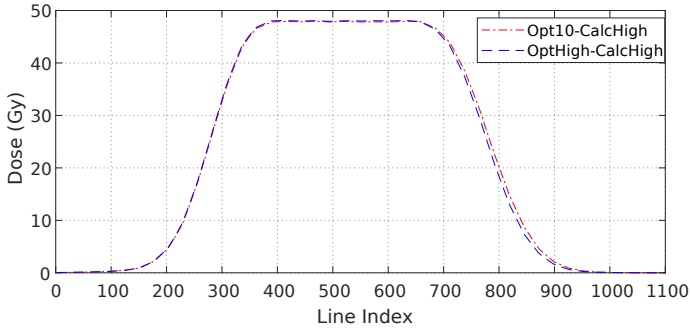

(d) Dose line

Figure 5.12: Illustration of the doses based on the plans optimized on (a) the standard-dose CT image, (b) LdCT 10%, and (c) the difference between them for case 14 (one of the cases with the lowest gamma passing rate). (d) The line doses for the plans optimized on the standard-dose and LdCT images.

5.4 Discussion

In proton therapy, daily CT image acquisition is paramount to ensure accurate dose calculation and subsequent plan adaptation. However, performing a new CT at every treatment session results in additional patient dose, increasing radiation-related risks to the patient. Reducing CT imaging dose is therefore crucial, especially if a 4DCT is required for plan adaptation. In this study, we investigated the effect of reducing CT imaging dose on proton therapy dose calculation.

Each experiment started by defining the treatment plan based on the standard-dose CT. The treatment plan was redefined for the corresponding LdCTs (with gradual reduction in imaging dose) and the results were compared with those of the standard-dose CT image.

The result shows the possibility of using LdCT for accurate proton therapy treatment planning. In the first step, OARs were delineated on the LdCTs and the standard-dose CT using an auto-contouring software. The results showed a strong overlap between the contours delineated on the LdCTs and the reference contours. In addition, the distance (HD-95) between contours is a few millimeters.

For the heart, kidney, liver, lung, and spleen the contours based on the LdCTs and the standard-dose CT image are almost identical. For the spinal cord, the error is larger (DSC mean: 0.94, lowest DSC: 0.86), however, it is smaller than the inter-observer variability reported in the previous studies. The spinal cord is hardly visible in CT images and its delineation is mainly based on guessing by using surrounding information, such as the spinal canal. Therefore, a larger error is expected even for manual delineation by an expert. Table 5.3 represents the DSC values reported from previous studies on inter-observer variability and also on auto-delineation approaches. The inter-observer variability is calculated by comparing contours that are manually delineated by two independent observers. For auto-delineation approaches, the (manually corrected) automated contours are compared with the contours delineated manually by an expert (ground truth). The results show that the effect of CT noise on the delineation of OARs is smaller than the inter-observer variability.

For the brachial plexus, however, the error is more pronounced, with the DSC of around 50% and HD-95 of around 6cm in the worst case. The brachial plexus is regularly contoured for upper-located lung tumors (3 out of 13 lung cases in this study). Delineation of the brachial plexus on CT images is challenging (with high inter-observer variability) due to its narrow elongated structure. Manual delineation is usually performed with the help of other surrounding structures as references (such as the vascular bundle, the scalene muscles, and the intervertebral foramina). MR images should be used instead, however, MR images are not always available. Reducing the CT imaging dose

might make the delineation of the brachial plexus even more challenging. Therefore, reducing the CT imaging dose might have a more profound impact on upper-located lung tumors (where the brachial plexus is an OAR) and therefore should be avoided. It should be noted that only 3 out of 13 lung cases were upper-located lung tumors with the need for the delineation of the brachial plexus. Interestingly, there was a good overlap between contours based on the LdCT with those of the standard-dose CT in these 3 cases. For the cases in which the HD-95 was several centimeters, there was no need to contour the brachial plexus. In addition, clinical tests in our center revealed that syngo.via has a mediocre performance for contouring the brachial plexus (even on standard-dose CTs) where larger margins are usually delineated.

For target volume delineation, the error due to the CT noise is in the same order as the inter-observer variability. Comparing the DSC with the inter-observer variability reported in the previous studies (DSC between 0.70 to 0.85 [165]) also shows that the error due to CT noise is smaller than the inter-observer variability. Although the DSC and HD-95 indicate a close

Table 5.3: Comparing the DSC (mean ± standard deviation) for contours based on LdCTs with the DSC reported in previous studies on auto-delineation approaches (automated delineation versus manual delineation) and inter-observer variability (manual delineation by two independent observers), showing that the effect of CT noise is smaller than inter-observer variability.

OAR	LdCT 10%	LdCT 30%	Previous studies on auto-delineation	Previous studies on inter-observer variability
Esophagus	0.962 ± 0.013	0.983 ± 0.007	0.72 ± 0.15 [159]	0.66 ± 0.06 [160]
			0.71 ± 0.05 [168]	0.83 ± 0.05 [168]
			0.75 ± 0.08 [169]	0.64 ± 0.13 [170]
Heart	0.993 ± 0.004	0.996 ± 0.002	0.91 ± 0.06 [159]	0.91 ± 0.02 [160]
			0.91 ± 0.03 [168]	0.94 ± 0.03 [168]
			0.87 ± 0.05 [169]	0.92 ± 0.04 [170]
Liver	0.988 ± 0.003	0.994 ± 0.002	0.89 ± 0.02 [168]	0.92 ± 0.04 [168]
				0.93 ± 0.01 [160]
Lungs	0.995 ± 0.003	0.998 ± 0.001	0.98 ± 0.01 [159]	0.72 ± 0.15 [160]
			0.95 ± 0.01 [168]	0.95 ± 0.01 [168]
			0.97 ± 0.01 [169]	0.97 ± 0.01 [170]
Spinal cord	0.947 ± 0.03	0.978 ± 0.009	0.80 ± 0.06 [159]	0.80 ± 0.06 [160]
			0.79 ± 0.03 [168]	0.80 ± 0.06 [168]
			0.90 ± 0.04 [169]	0.74 ± 0.12 [170]

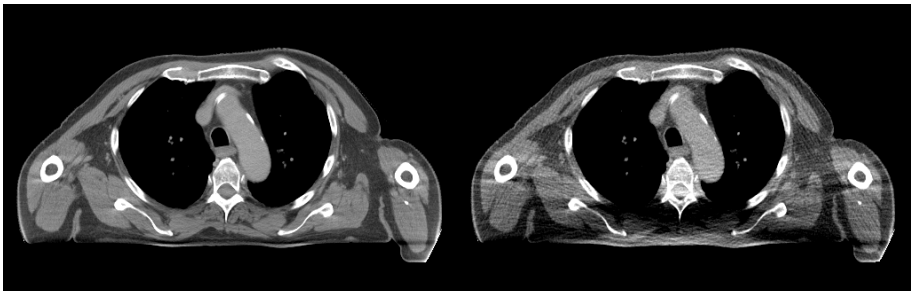

Standard-dose CT LdCT 10%

Figure 5.13: Illustration of the standard-dose CT and the corresponding LdCT 10% for case 4 (blue triangle in Figure 5.7) where the most severe dose calculation error was observed (window level: 50 HU, window width: 200 HU).

agreement between target volume contours, the radiation oncologist reported a lower feeling of certainty for contours delineated on the LdCT compared to the standard-dose CT images.

The effect of CT noise on proton therapy dose calculation and plan optimization confirms our previous findings in Chapter 4. The gamma passing rate (3%/1 mm) for the dose calculation test is around 100% after a 90% reduction in imaging dose, except for case 4 (blue triangle in Figure 5.7) where the gamma passing rate is around 94%. However, lowering the CT imaging dose up to 70% did not have a profound impact on dose calculation. Figure 5.13 illustrates the standard-dose CT and the corresponding LdCT 10%. This CT image was obtained from an obese patient. Lowering the CT imaging dose resulted in photon starvation at the detector and therefore in a strong streak artifact in the images. This led to a significant degradation in image quality. The lower gamma passing rate in case 4 can be explained by the fact that two posterior beams were used in the presence of severe streak artifacts, therefore, a lower dose reduction is recommended for this case. A major advantage of employing a LdCT simulator is that it allows us to estimate the appropriate CT imaging dose reduction for each individual based on patient anatomy, treatment site, beam angle, etc.

For the plan optimization, the errors are larger, even for LdCT 75%. However, the gamma passing rate (3%/3 mm) was always above 90%, showing the plans based on the LdCT and the standard-dose CT are clinically equivalent. Considering the 3%/1 mm criteria, the gamma passing rate is above 90% for the LdCTs with effective mAs of 25 mAs or higher. It should be noted that the errors at much lower doses are only slightly higher than the error for LdCT 75%. In another word, optimizing on LdCTs led to a

constant negative effect on the gamma passing rate in the majority of cases. That indicates that the other effects of random variation are dominating in the plan optimization test and the CT noise is not the only cause of the plan optimization error. Our previous findings on the plan optimization test in Chapter 4 support this conclusion.

To summarize our findings, we believe that LdCTs with aggressive dose reduction can be used for proton therapy dose calculation and plan optimization. For example, CT imaging dose can be reduced dramatically for dose restoration techniques [79, 80, 81], without having a significant adverse impact on the outcome. In some cases, however, aggressive dose reduction should be avoided. For example, the doses recalculated on LdCTs may no longer be accurate in the presence of severe photon starvation.

Organ contouring is more sensitive to dose reduction than dose calculation. Yet, LdCTs can still be used in a wide variety of cases where the delineation of anatomical structures is needed, for example for esophageal cancer patients. This is especially true if auto-segmentation tools are employed for the delineation of anatomical structures. There are, however, some OARs that are more sensitive to dose reduction, such as the brachial plexus and spinal canal. We believe that this also holds true for head and neck cases where the delineation of soft tissues is involved. Therefore, less dose reduction is expected to be achievable in these cases.

Better results might be achieved by denoising the LdCT images before using them for proton therapy treatment planning. LdCT denoising techniques and the possibility of using them for different tasks in proton therapy will be discussed in Chapter 6.

5.5 Conclusion

Our results suggest the possibility of using LdCT imaging protocols for proton therapy treatment planning where the plans based on LdCTs with a 90% reduction in CT imaging dose were clinically equivalent to those based on the standard-dose CTs. LdCTs can be used for target volume and OARs delineation where the error due to CT noise is in the same order as (or even smaller than) the inter-observer variability. For proton dose calculation and plan optimization, the results were in line with our previous findings where the doses based on LdCTs and the standard-dose CTs were clinically equivalent. Larger errors were observed in some of the cases. As an example, the higher level of CT noise on LdCTs might hinder the delineation of the brachial plexus or spinal cord. In addition, the dose calculation based on LdCTs might be inaccurate in the presence of severe photon starvation. Consequently, less dose reduction is probably recommended for these cases (up to 70%).

6

Suppressing the (already small) effects of CT dose reduction with a convolutional neural network

6.1 Introduction

There is a growing body of evidence that suggests LdCT protocols are suitable for several tasks in proton therapy treatment planning. This includes proton therapy dose calculation [144, 133, 145], plan optimization [144], target volume delineation (Chapter 5), contours propagation [145], and OARs delineation (Chapter 5). However, human intervention in the process of plan adaptation is inevitable. For example, automated contours must be corrected and reviewed manually by an expert. In the event of significant tumor shrinkage, target volumes should be manually redefined. A higher level of CT noise on LdCTs may hamper plan adaptation, especially if human intervention is required. It is due to the fact that the human visual system is unable to optimally deal with the correlated noise [171] in tomographic images. This problem can be addressed by employing a LdCT denoiser to suppress CT noise on LdCTs.

CT denoising can be performed during image reconstruction, usually by employing advanced iterative image reconstruction techniques [172, 173, 174, 175], for example by defining a penalty term [176, 177, 173]. Despite their

effectiveness, iterative techniques are rarely used in clinical practice due to their long computation time. This is especially true in situations where time is of the essence, such as in adaptive proton therapy. Faster LdCT denoising can be achieved by pre-processing sinograms [178] or by post-processing reconstructed images [179].

Convolutional Neural Network (CNN) has been shown to be effective for LdCT denoising [180, 181, 182, 183, 141, 184]. CNN is a type of deep-learning model for analyzing and identifying textures and patterns in structured data such as images. CNN is computationally more efficient than traditional fully connected approaches in terms of memory and complexity. CNN is composed of a series of convolution layers usually in combination with a non-linear operator and subsampling layers. Convolution layers aim to automatically extract the appropriate features from the image.

The common way to train a CNN-based LdCT denoiser is to feed the noisy LdCT image as the training input and the clean image as the training label to the network. Therefore, the so-called Low-dose-to-High-dose (Ld2Hd) CT denoiser requires the noisy LdCT image along with the (clean) high-dose CT image. Simulating realistic LdCT images from the high-dose scans using a LdCT simulator is an effective and safe way to generate the training pairs. Nevertheless, the correlation between the noise in the label (high-dose CT) and on the sample (low-dose CT) could have an adverse impact on training.

Training can also be performed without the need for clean images (label). Lehtinen et al. [185] showed the possibility of training a denoiser using only noisy pairs. The so-called Noise2Noise network requires two noisy images of the same object which have a zero-mean noise. Noise2Noise networks cannot eliminate image artifacts that cannot be removed by ensemble averaging due to the fact that the training pairs should meet the assumption of zero-mean noise [141].

Yuan et al. [186, 141] showed that the Low-dose-to-Low-dose (Ld2Ld) networks achieved comparable results to Ld2Hd for LdCT denoising. However, Ld2Ld approaches still require two independent (noisy) measurements of the same subject. The Half2Half [141] model splits the high-dose image into two LdCT scans which guarantees independent noise distribution between the two pairs and eliminates the correlation between training pairs. In the cases where generating training pairs (Ld2Hd, Ld2Ld, or Half2Half) is not possible, Noise2Void [187] approaches (blind-spot network) can be employed. Noise2Void networks enable image denoising using only a single noisy image, however, fall behind the networks that use training pairs because more information is provided if the training pairs are available.

Training can be performed in both sinogram and image domains. Noise2Noise approaches are more effective in the sinogram domain. This is due to the fact that it is easier to obtain a zero-mean noise in the sinogram

domain. Noise in the image may not be zero-mean at extremely LdCTs due to the logarithm transformation [141] and nonlinear smoothing filter. However, sinogram-based denoising can cause inconsistencies in the sinograms, resulting in severe artifacts in the reconstructed images. Furthermore, training a network in the image domain is much faster, does not require projection data (usually not available), and does not involve image reconstruction.

A thorough comparison of Ld2Hd and Ld2Ld approaches by Yuan et al. [141] demonstrated that Ld2Hd networks are more robust and outperform Ld2Ld networks (including Noise2Noise or Half2Half) in real-life scenarios. Therefore, a Ld2Hd network in the image domain appears to be a promising option for the adaptive proton therapy regimen.

As can be seen, appropriate training pairs are paramount for the training of an efficient LdCT denoiser. CNN-based CT denoisers might be hampered by the lack of high-quality training data. The in-house LDCT simulator [134] (Chapter 3) can be used to generate high-dose (clean) and low-dose (noisy) training pairs. Training can then be carried out using these training pairs.

In this chapter, we aim to develop and train a CNN to denoise LdCT images. The architecture of the LdCT denoiser and the details on the generation of training pairs are discussed in Section 6.2.1 and 6.2.2, respectively. The denoised LdCT images will then be used for proton therapy treatment planning, as described in Section 6.2.4. Section 6.3 presents experimental results. The discussion and concluding remarks are presented in Section 6.4 and 6.5.

6.2 Materials and Methods

Implementing a CNN-based denoiser can be divided into two main tasks: designing the network architecture and generation training pairs. The following sections will discuss these two tasks in more detail. Finally, the denoised images will be used for proton therapy dose calculation, plan optimization, and OARs delineation. Results based on (noisy) LdCTs and denoised LdCTs can be compared with those from standard-dose CTs to determine the feasibility of CNN-based denoising techniques in proton therapy.

6.2.1 Network architecture

The network architecture adopted in this study is ResUNet [188, 189] which combines two well-known CNN architectures: UNet [190] and ResNet [191]. Figure 6.1(a) represents the network architecture. The network has a UNet [190] encoder-decoder architecture with skip connections, in combination with, pre-activated residual connections (also known as shortcut

connection) [191]. The skip connections concatenate the features (directly) from the encoder path to the decoder path, aiming to recover spatial information lost during down-sampling and also to tackle the vanishing gradient problem. The residual connections allow the network to focus on learning just the residual (the difference between the input and the output), which is suitable for CT denoising applications. For example, a "unit" transformation (identity mapping) can be implemented more effectively by a residual network (by setting residuals to zero) instead of learning a "full" transformation by a stack of nonlinear layers.

The main branch of each building block consists of two convolution layers (kernel size 3×3) each of which is followed by batch normalization [192] and Parametric Rectified Linear Unit (PReLU) activation [193]. The convolutional layers are the main component on a CNN. They consist of a set of filters (kernels) to scan the image and extract appropriate features from the image. The parameters of these filters are learned throughout the training process. Batch normalization layers enable faster and more stable training by standardizing the feature maps to maintain the mean output close to 0 and the output standard deviation close to 1. Activation layers, such as PReLU, introduce non-linearity to the model, allowing the network to learn complex non-linear functions.

UNet architecture, shown in Figure 6.1(a), consists of several down-samplings using a Max Pooling operation. Max Pooling is a form of downsampling that selects the maximum value for 2×2 patches of a feature map, intended to identify the most prominent features of the feature map. By including downsampling layers, multi-resolution level feature extraction and a larger receptive field can be obtained. In addition, the number of trainable parameters is reduced, helping to speed up the training process. The number of features is doubled after each downsampling. Finally, upsampling layers are carried out. Upsampling layers increase the resolution of the feature maps progressively to generate feature maps with the size of the original input image. A transposed convolutional layer [194] (sometimes wrongfully called deconvolution layer) with stride 2 is commonly employed for upsampling.

Residual connection means that the input of each building block is propagated to its output, as shown in Figure 6.1(b). The residual connection has a convolution layer (kernel size 1×1) to assure an equal amount of feature maps before summation. A UNet architecture can be designed by simply removing the residual connections.

After the final building block, two additional convolution layers, followed by PReLU activation, are applied to the feature maps. Finally, the output of the network is cropped to include only relevant voxels to contribute to the loss function.

Training can be performed with 2D or 3D images as input. 2D models

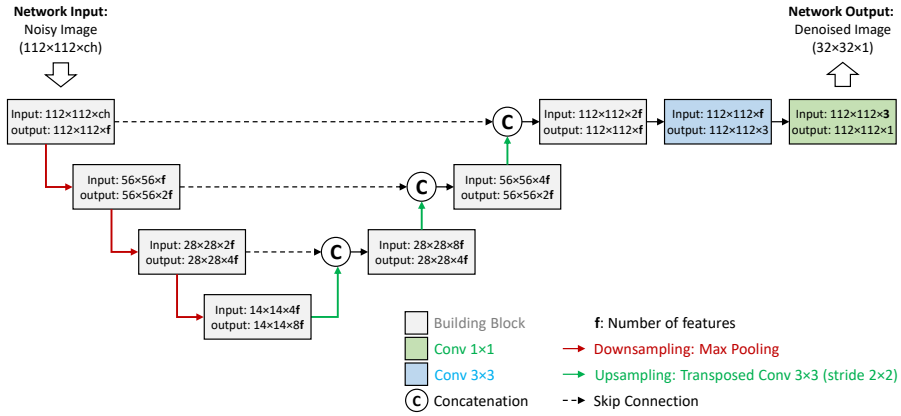

(a): Network architecture

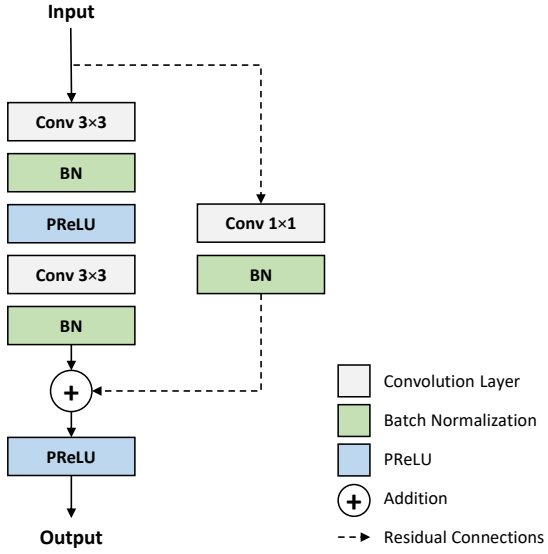

(b): Building block

Figure 6.1: The architecture of the CT denoiser. (a) The network has a UNet structure (encoder-decoder architecture) with residual connections. (b) A building block consists of a series of convolution layers, batch normalization, and PReLU combined with residual connections.

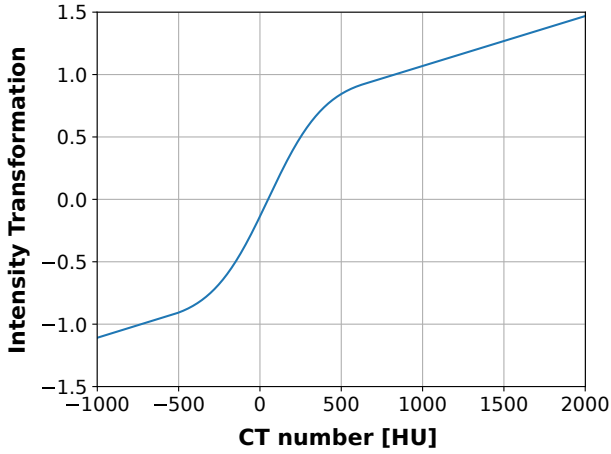

Figure 6.2: u
sing a logistic-like function]The contribution of soft tissue in the training process can be emphasized by transforming CT numbers [HU] using a logistic-like function.

are faster to train but suffer from a lack of spatial information. This problem can be addressed using 3D images, however, it increases training time and requires sufficient computation resources. A better solution can be achieved using a stack of a few transaxial slices (2.5D network) which incorporates spatial information from adjacent slices in the training and is fast at the same time.

As already mentioned, we aim to denoise LdCT images to make it easier for human operators to review and correct automated contours. Highly attenuated structures are clearly visible in LdCTs and are not severely affected by CT noise. Therefore, the input images are normalized to focus on soft tissues since delineated OARs are mostly composed of soft tissues. The images are normalized using a logistic-like function with a smooth tail as presented in Figure 6.2.

CT denoisers rely heavily on the selection of appropriate loss functions. The loss function evaluates the performance of the network during training. During training, network parameters are optimized to minimize the loss function. The appropriate loss function must be chosen based on the application. For example, Mean Absolute Error (MAE) has been shown to be more robust to outliers and could be a suitable option if the denoised CT will be used for dose calculation. On the other hand, if the denoised images will be used for reviewing or correcting automated contours, the structural similarity index measure (SSIM) [195] might be a better option. Employing

conventional pixel-based losses usually results in image over-smoothing [196]. Perceptual (feature-level) losses [197, 198] can be employed instead to preserve structural details. For instance, VGG perceptual loss [199] compares the feature maps of the ReLU activation layers, produced by passing the input and reference image through the pre-trained VGG network. Perceptual losses, however, tend to introduce CT number bias in the denoised images [196, 200, 201]. The combination of MAE and SSIM losses has been shown to be effective for CT denoising applications [201]. Therefore, the loss function is defined by combining the MAE and SSIM losses (same weight) as follows:

$$\text{Loss function} = \text{MAE} + (1 - \text{SSIM}) \tag{6.1}$$

The model was optimized through the Adam optimizer [202]. The initial learning rate was set to 5e-4 and it was gradually reduced by 80% once the training loss stopped reducing for 50 epochs. The denoiser was implemented with Keras Tensorflow (version 2.5.0) and trained on the NVIDIA TITAN Xp GPU (12GB).

6.2.2 Training data

The planning CTs of 13 esophageal and lung cancer patients were used to train and validate the CT denoiser. The raw CT data of these patients were collected prospectively and processed retrospectively to generate high- and low-dose CT pairs. The in-house LdCT simulator (Chapter 3) was used to simulate LdCTs with an 80% reduction in CT imaging dose (LdCT 20%). The simulated LdCTs were reconstructed with Siemens offline reconstruction software [ReconCT 14.2.0.40998] and the average image was derived from the 4DCT images (with 10 breathing phases, voxel size $0.97\times0.97\times3$ mm^3). The acquisition protocols for the reference CT scans are described in Table 5.1. The available dataset was split into training and test sets. The training set consists of 3D images of 9 patient cases (in total 915 2D slices) and was split into three sets. Half of the data (every second slice) was used for training the network. The other half was divided into the validation set (to save the model with the lowest validation loss during training) and the test set (to evaluate model performance in the early phases). The input images had the size of [image width $\times$ image height $\times$ number of channels] and were comprised of the central slice and the corresponding adjacent slices (for 2.5D training). The final comparison between different networks was carried out using 4 patient cases (in total 515 2D slices) that were not observed by the network during network implementation. These 4 cases were also used for proton treatment planning to assess whether the denoised images can be used for proton therapy treatment planning.

6.2.3 Evaluation metrics

The CT denoiser network was evaluated using Mean Absolute Error (MAE), Peak Signal-to-Noise Ratio (PSNR), and Structural Similarity Index Measure (SSIM). The MAE of the Hounsfield unit compares the denoised images by taking the absolute value of the voxel-by-voxel difference between the denoised image (x) and the reference dose CT (y). It is calculated as:

$$MAE = \frac{1}{N}\sum_{i=1}^{N}|y_i - x_i| \tag{6.2}$$

where i represents the voxel index in the image domain. The lower the MAE, the better the quality of the denoised images. However, for training the MAE was computed from the normalized HU values focusing on soft tissues. It is possible that one image has a better MAE on HU-values, whereas another one has a better MAE on normalized values. The PSNR is calculated as:

$$PSNR = 10\log(\frac{R^2}{MSE}) \tag{6.3}$$

where R represents the range of the pixel values and was set to 300 HU in this study. MSE represents the Mean Square Error (MSE) and is calculated the same as the MAE but uses the squared difference instead of the absolute difference. The higher the PSNR, the better. It is a logarithmic quantity and is expressed in decibels (dB).

SSIM compares the structural information to quantify the structural similarity between two images. The SSIM ranges from -1 (no agreement) to +1 (complete agreement) and is calculated as:

$$SSIM = \frac{(2\mu_x\mu_y + c_1)(2\sigma_{xy} + c_2)}{(\mu_x^2 + \mu_y^2 + c_1)(\sigma_x^2 + \sigma_y^2 + c_2)} \tag{6.4}$$

where μ_x and μ_y represent the mean value of the images, σ_x^2 and σ_y^2 represent the image variance, and σ_{xy} denotes the covariance of the two images. c_1 and c_2 are constant values given by $c_1 = (0.01R)^2$ and $c_2 = (0.03R)^2$ where R denotes the range of the image (R = 300 HU).

The Wilcoxon signed-rank test [203] was used to see if the results of two networks (for instance two networks with different architectures or training parameters) are different from one another in a statistically significant manner. The Wilcoxon test is a nonparametric statistical test. The null hypothesis is that two related paired samples are from the same population. The null hypothesis can be rejected if the p-value is lower than the significance level (usually 0.05), indicating that there is enough evidence that the results of two sets are statistically significant.

6.2.4 Denoised LdCT for proton therapy

The denoised LdCTs are then used for proton therapy dose calculation, plan optimization, and OARs delineation to see if a better result can be achieved by replacing (noisy) LdCT with the denoised image.

For the dose calculation and plan optimization, the experiment design is similar to that described in Sections 4.2.1 and 5.2.3. The standard-dose CT is first used for the plan optimization (OptHigh) and final dose calculation (CalcHigh). The results from the standard-dose CT are considered to be the ground truth. Then LdCT images (noisy and denoised images) are used for the dose calculation (OptHigh-CalcLow) and plan optimization (OptLow-CalcHigh). Finally, the results based on denoised and (also) noisy LdCT are compared with OptHigh-CalcHigh to explore the feasibility of using LdCT denoiser for proton therapy dose calculation and plan optimization.

To explore the possibility of using the denoised images for OARs delineation, OARs were delineated on the (noisy) LdCTs and the denoised images using an automated delineation approach. The results were then compared with those of the standard-dose CT image (similar to the methods described in Section 5.2.1). A CNN-based automated delineation tool was employed to delineate OARs. This tools was developed and validated at the Department of Electrical Engineering (ESAT), KU Leuven University, in collaboration with the Radiation Oncology Department of the University Hospital of Leuven in Belgium. The probability of belonging to a specific organ class for each voxel was estimated by employing a 3D CNN based on the DeepMedic architecture [204]. Planning CTs of 60 esophagus patients with the corresponding delineations were used to train and validate this tool [205, 157]. The results showed the efficiency of automatic delineation where only minor correction was required for approval.

6.3 Results

The model was trained using different parameters to tune the most suitable network design for denoising LdCT images. The number of epochs was fixed at 2000 in all experiments. The validation loss curve was monitored to ensure that no over-fitting was observed. Figure 6.3 represents an example of the training and validation loss as a function of the epoch. The loss decreases as the training proceeds and no over-fitting is observed.

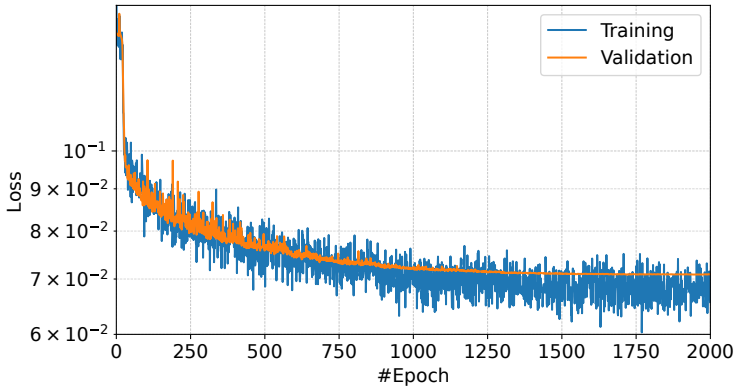

Figure 6.3: The training and validation loss as a function of the training epoch.

6.3.1 Evaluation of LdCT denoiser network

In the first step, the CT denoiser was trained using two different architectures: UNet and ResUNet. The only difference between these two networks is the addition of residual connections in ResUNet. The networks were trained using different initial (starting) feature sizes, from 16 up to 128. Figure 6.4 represents the results based on these two architectures and as a function of initial number of features. First, lower MAE and higher PSNR and SSIM were achieved with ResUNet architecture showing that ResUNet architecture outperforms the UNet for CT denoising tasks (p-value for MAE : 6e-85, p-value for PSNR : 2e-60, p-value for SSIM : 8e-39). In addition, better results were achieved by increasing the number of features. However, it came at the cost of longer training time. For example, comparing the ResUNet networks with 16 and 128 features shows that the network with 128 features significantly outperforms the network with 16 features (p-value for MAE : 1e-22, p-value for PSNR : 1e-22, p-value for SSIM : 1e-22).

Typically, denoising strategies use image averaging techniques to reduce noise, mainly by incorporating local information. Therefore, a sort of image averaging is expected to be learned by the network for image denoising. Consequently, a deep network (several downsamplings) is usually not required for denoising applications as the contribution of local information is larger. On the other hand, more complex features are included in the training as the number of features increases, resulting in a better performance.

The network was trained using different depths and initial number of features. Figure 6.5 illustrates the results based on networks with different depths and initial number of features. It can be seen that the network with a down-sampling depth of 3 outperforms the network with depth 2 where lower

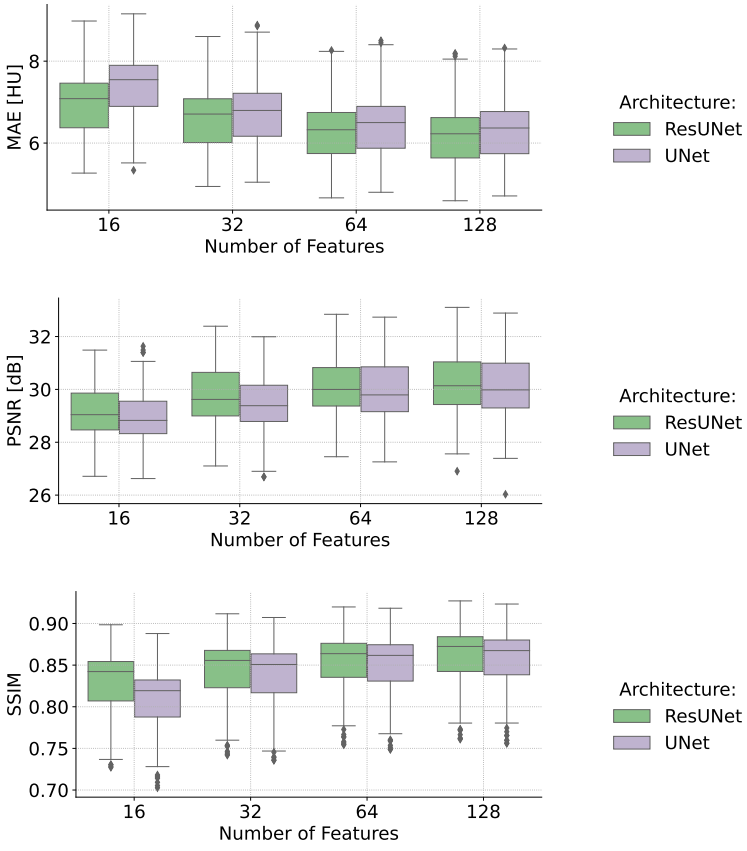

Figure 6.4: Comparing the ResUNet and UNet architectures for LdCT denoising. In addition, a larger initial feature size improves the performance of the LdCT denoiser.

MAE and higher PSNR and SSIM were observed (p-value for MAE : 6e-85, p-value for PSNR : 1e-69, p-value for SSIM : 1e-23). However, increasing the depth of the network beyond 3 does not make the predictions increasingly more accurate. On the other hand, increasing the number of features was found to have a stronger impact than increasing the depth of the network. Increasing the number of features for both shallow and deep networks resulted in lower MAE and higher SSIM and PSNR.

In order to accelerate the training process, training is usually performed using 2D slices. However, better performance might be achieved by

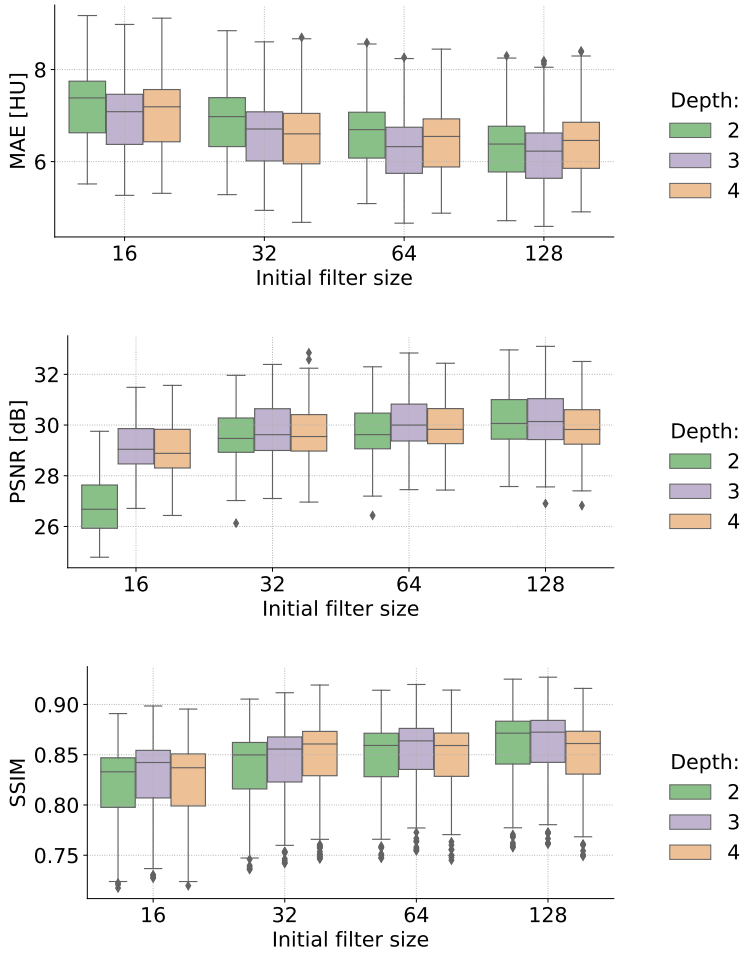

Figure 6.5: A comparison of networks with different depths and initial number of features.

incorporating information from adjacent slices. The model was trained (ResUNet, depth = 3, initial number of features = 128) using single channel (2D network) and multiple channels (2.5D network). For the 2.5D networks, the central slice along with the adjacent slices on the right and left construct the network input. Figure 6.6 compares the 2D and 2.5D networks. Accordingly, the denoiser performs slightly better when adjacent slices were included. For example, MAE for the network with 5 slices was only 0.08 HU

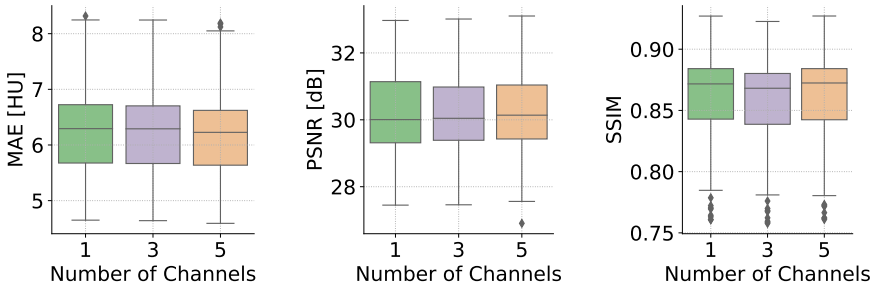

Figure 6.6: Comparing the 2D (1 input channel) and 2.5D (3 and 5 input channels) networks. Including information from adjacent slices did not have a significant impact on the CT denoiser.

smaller than the 2D network, which is very small for many applications. However, the difference was statistically significant (p-value for MAE : 1e-22, p-value for PSNR : 1e-13, p-value for SSIM : 1e-6). The small difference between 2D and 2.5D networks could be due to the fact that the slice thickness (3 mm) was approximately three times higher than the X and Y pixel size (0.97 mm). Therefore, the relevance of pixel information in 2D planes is expected to be higher. We believe that adjacent slices should be included in denoising as they contain useful information, especially for images with small slice thicknesses.

The final analysis was conducted by comparing noisy LdCTs and denoised images with the reference-dose CT images (ground truth). First, the model was re-trained using the combination of LdCT 10% and LdCT 20% as the training samples. The denoising network had ResUNet architecture with 3 down-sampling stages, an initial number of features of 128, and 5 input channels. Table 6.1 compares MAE, PSNR, and SSIM for the noisy LdCT and the denoised CT images. It can be seen that the denoiser network successfully suppressed the CT noise where lower MAE (by around 2 HU) and higher PSNR and SSIM were observed for the denoised image (p-value for MAE : 1e-22, p-value for PSNR : 1e-22, p-value for SSIM : 1e-22). Figure 6.7 and 6.8 illustrate the examples of the LdCT (input), the denoised image (prediction), and the reference CT (label) for a lung and esophageal cancer patient. It can be seen that the denoiser network reduced the CT noise while preserving edges and soft-tissue information in the denoised images.

Table 6.1: Quantitative comparison of the noise level (mean ± standard deviation) in the noisy LdCT and the denoised image.

		noisy LdCT	denoised CT
LdCT 20%:	MAE [HU]	8.16 ± 1.19	6.20 ± 0.82
	PSNR [dB]	27.8 ± 1.31	30.2 ± 1.18
	SSIM	0.79 ± 0.05	0.86 ± 0.04
LdCT 10%:	MAE [HU]	9.96 ± 1.62	7.59 ± 1.14
	PSNR [dB]	25.4 ± 1.58	27.7 ± 1.84
	SSIM	0.72 ± 0.05	0.82 ± 0.04

6.3.2 Denoised LdCT for proton therapy

Two lung (cases 1 and 2) and two esophageal (cases 3 and 4) cancer patients were used to explore the possibility of using denoised LdCTs for proton therapy dose estimation. In each test, the noisy and denoised LdCTs were used for proton therapy dose calculation and plan optimization. The doses estimated based on these LdCTs were then compared with those based on the standard-dose CTs using the gamma analysis. Table 6.2 and 6.3 report the gamma passing rate (1%/1 mm) for doses based on the noisy and denoised images. Accordingly, the doses calculated based on the denoised images slightly outperform those based on the noisy LdCTs (Table 6.2). However, we have already shown that the dose calculation test is not dramatically affected by the CT noise and even noisy LdCTs produce satisfactory results. In addition, the plans optimized on the denoised images outperform the plans optimized on the noisy LdCT where a higher gamma passing rate was observed (Table 6.3).

The denoised images were also used for the delineation of OARs. A CNN-based auto-contouring software was employed to delineate OARs (including brachial plexus, fundus, heart, spinal cord, liver, kidney, and lung) on the noisy LdCT images, denoised LdCT images, and standard-dose images. The results acquired from the LdCT images (noisy and denoised images) were then compared with those based on the standard-dose CT images. The agreement between the contours was quantified using Dice Similarity Coefficient (DSC) and Hausdorff Distance (HD), as described in Section 5.2.1. Figure 6.9 illustrates the DSC and HD-95 values acquired from the noisy and denoised LdCT images for different OARs for two lung and two esophageal cancer patients. In this figure, different colors represent different cases. The X-axis represents the results based on the noisy LdCT images and the Y-axis represents the corresponding value based on the denoised image.

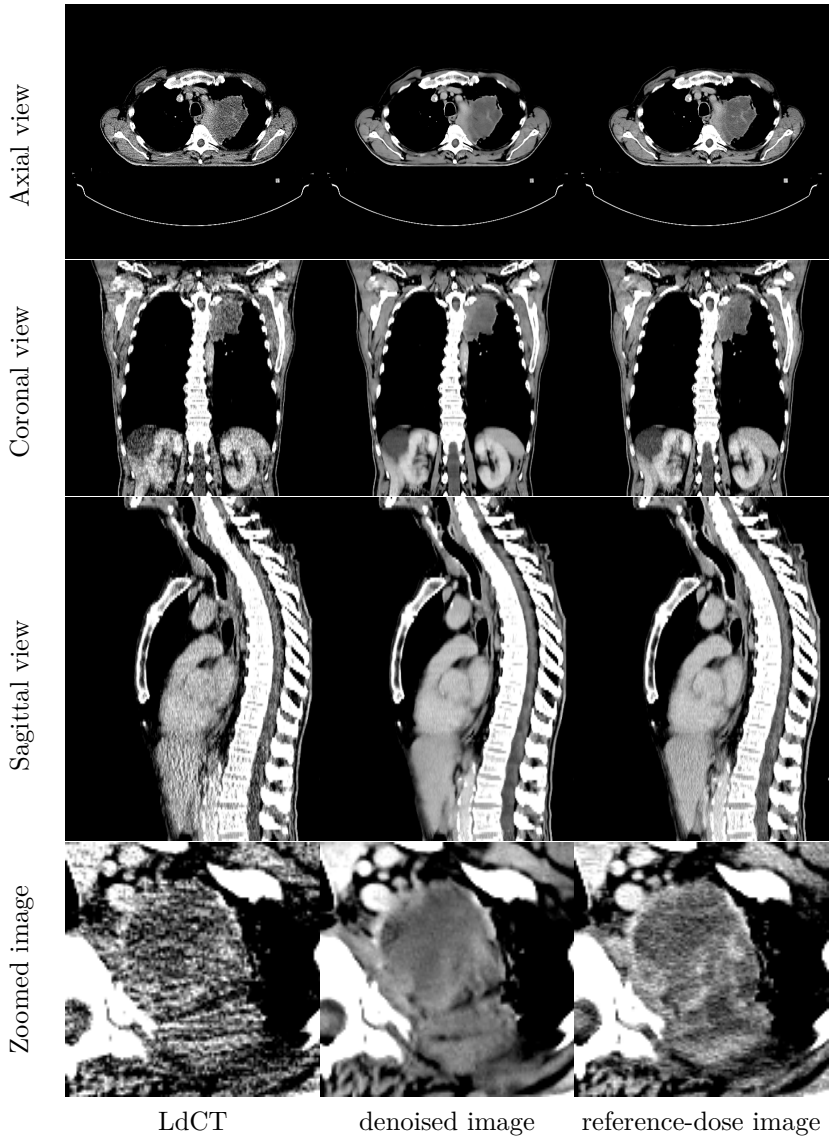

Figure 6.7: Representation of the LdCT 10%, the denoised image using ResUNet network, and the reference-dose CT image for a lung cancer patient. The results show that the network successfully suppressed LdCT noise (window level: 50 HU, window width: 200 HU (row 1 to 3) and 100 HU (row 4)).

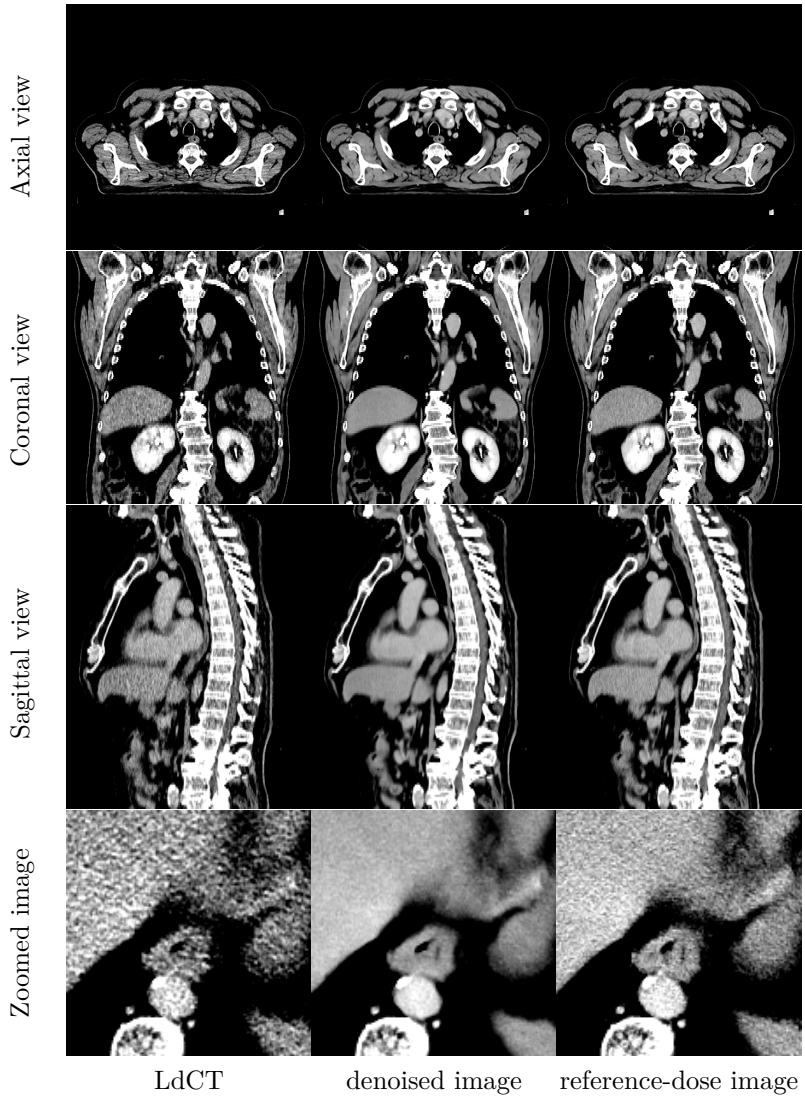

Figure 6.8: Representation of the LdCT 20%, the denoised image using ResUNet network, and the reference-dose CT image for a esophagus cancer patient. The results show that the network successfully suppressed LdCT noise (window level: 50 HU, window width: 200 HU (row 1 to 3) and 100 HU (row 4)).

Table 6.2: Comparison of the doses calculated based on the noisy and denoised LdCTs (OptHigh-CalcLow) with doses calculated on the standard-dose CT (OptHigh-CalcHigh). This table reports the gamma passing rate (GPR) and the mean value of the gamma test.

	LdCD 10%		Denoised image		LdCD 20%		Denoised image	
case	GPR	mean	GPR	mean	GPR	mean	GPR	mean
1	100	0.09	100	0.09	100	0.07	100	0.07
2	99.61	0.18	99.43	0.21	100	0.13	99.84	0.14
3	100	0.10	100	0.05	100	0.08	100	0.05
4	100	0.13	100	0.08	99.88	0.13	100	0.06

Table 6.3: Comparison of the plans optimized based on the noisy and denoised LdCTs (OptLow-CalcHigh) with plans optimized on the standard-dose CT (OptHigh-CalcHigh). This table reports the gamma passing rate (GPR) and the mean value of the gamma test.

	LdCD 10%		Denoised image		LdCD 20%		Denoised image	
case	GPR	mean	GPR	mean	GPR	mean	GPR	mean
1	94.68	0.32	97.08	0.26	95.34	0.29	97.22	0.25
2	89.65	0.47	92.41	0.42	92.98	0.41	94.25	0.38
3	97.07	0.26	97.90	0.20	97.70	0.22	97.78	0.21
4	99.27	0.24	99.92	0.17	99.49	0.22	99.93	0.15

Accordingly, the majority of the points are above the line of identity (gray line) for DSC, especially for LdCT 10%. This shows that the DSCs acquired from the denoised images are higher than those based on the noisy LdCT images. For HD-95, the majority of points are below the line of identity, showing that HD-95 values are smaller for contours acquired from the denoised images. In some cases, however, the results based on noisy LdCTs outperformed those based on the corresponding denoised image.

6.4 Discussion

In the study, a LdCT denoiser based on the ResUNet architecture was implemented and trained to suppress CT noise in LdCTs. The network was trained using the standard-dose CT (training label) and the realistic

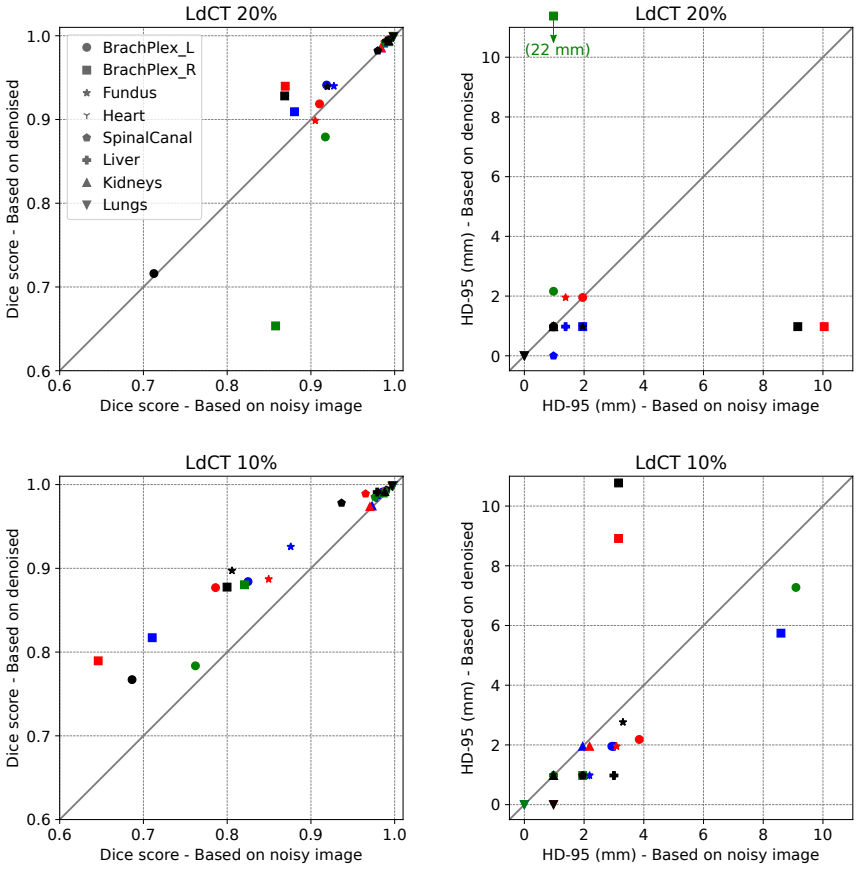

Figure 6.9: Comparing the OARs delineation based on the denoised images with those obtained from noisy LdCTs. The X-axis represents DSC (left) and HD-95 (right) acquired from LdCTs. The Y-axis shows the corresponding points based on the denoised images. For DSC the points above the line of identity (gray line) and for HD-95 the points below the line of identity indicate better performance in the delineation of OARs.

simulated LdCT (training sample) pairs. It was shown that the ResUNet network outperforms the UNet network for CT denoising applications. Better results were achieved by increasing the number of features. On the other hand, increasing the depth of the network did not have a notable impact on the results.

The final results showed the capability of the network in reducing CT noise on LdCT images where a lower MAE and higher PSNR and SSIM were observed

after denoising. In addition, the edges were well preserved in the denoised image.

The denoised LdCT images were then used for proton therapy dose calculation, plan optimization, and OARs delineation. Using the denoised images for the dose calculation slightly improved the results. However, it was already shown that the dose calculation test is robust against CT imaging dose reduction where the doses calculated based on LdCTs and standard-dose CTs were almost identical (Chapter 4 and 5). This suggests that denoising LdCTs is not critical for proton dose calculation.

The denoised LdCT images were also used for plan optimization. The results showed that the plans optimized on the denoised images outperformed the plans based on the noisy LdCT images. Denoising LdCTs resulted in a higher gamma passing rate, reported in Tabel 6.3, showing the applicability of CNN-based denoisers in proton therapy treatment planning.

Finally, OARs were delineated on the LdCT (noisy and denoised) images and then compared with those based on the standard-dose CTs. Comparing the results based on the noisy and denoised LdCT images showed that image denoising has a positive impact on the delineation of OARs. Higher DSC and lower HD-95 were observed after denoising the CT images. However, the delineation of the brachial plexus was still challenging in the denoised images (circle and square points in Figure 6.9). In one of the cases (green square in top-right image in Figure 6.9), the delineation of the brachial plexus was dramatically better on the noisy LdCT 20%. This point can be seen as an outlier because the software successfully delineated the brachial plexus on LdCT 10% where HD-95 is around 1 mm.

It should also be noted that the results in Figure 6.9 are in line with our previous finding in Chapter 5 where a larger error was observed for the delineation of the brachial plexus. It suggests that less dose reduction is recommended if the brachial plexus must be delineated as an OAR.

6.5 Conclusion

In this chapter, a CNN-based LdCT denoiser was developed and validated based on the ResUNet architecture. The results indicated that the network successfully suppressed CT noise. Comparing LdCTs (noisy and denoised images) with standard-dose CT images showed that denoising LdCT images led to a lower MAE and a higher PSNR and SSIM. In addition, using the denoised images for proton therapy dose calculation, plan optimizations, and OARs delineation yielded better results.

7 Discussion

The key benefit of proton therapy is its ability to tailor the therapeutic radiation dose closer to the target volume, resulting in a highly conformal dose to the target volume and in better sparing of surrounding healthy tissues. The radiation is usually delivered over multiple weeks during the course of fractionated proton therapy. Anatomical variations throughout the course of radiation may lead to substantial dose distortions, compromising the physical advantages of proton beams. Plan adaptation is an effective strategy to account for these changes. Plan adaptation involves detecting anatomical changes and adjusting the plan according to the patient's new anatomy.

There is a growing body of evidence suggesting that adaptation will shape the future of proton therapy. Adaptation employs an imaging feedback loop to detect anatomical changes and adjust the plan to the patient's new anatomy. Thus, new CT images are needed in the adaptive regimen. Performing repeated CTs results in an accumulated additional patient dose, increasing radiation-related risks. This problem can be addressed by employing LdCT protocols. Lowering the CT imaging dose comes at the cost of a higher level of CT noise and might be a source of potential inaccuracy.

We hypothesized that the CT imaging dose can be reduced for different tasks in proton therapy. In addition, we believe that the errors introduced by CT noise are usually similar to (or even smaller than) other sources of uncertainty such as patient setup variation, tissue assignment, or statistical uncertainty of the Monte Carlo simulation.

To this end, a LdCT simulator was developed and validated to simulate

LdCTs from standard-dose CT, as described in Chapter 3. This tool enabled us to explore the possibility of reducing CT imaging dose and to make a patient-dependent dose reduction. The idea was, first, to simulate LdCTs with a gradual reduction in the imaging dose and, second, to use them for different tasks in proton therapy. Comparing the results based on LdCTs with those of standard-dose CT allowed us to quantify the impact of reducing CT imaging dose.

7.1 LdCT simulation

The LdCTs were simulated by adding an appropriate amount of position-dependent and correlated noise to the standard-dose scan to make a noisier image. The LdCTs were simulated in the sinogram domain because CT noise characteristics can be accurately described in the sinogram domain. The LdCT simulator accounted for the bowtie filter, for the quantum and electronic system noise, for the correlation (crosstalk) between detector elements, for the beam hardening effect, and for the non-linear smoothing filter in very low-dose scans. In several studies, LdCTs were simply modeled by adding Gaussian noise to the standard-dose CT image. As presented in Figure 3.4, different components in CT scanners can significantly affect the characteristics of CT noise, therefore, should be taken into account when simulating LdCTs.

Several phantom studies were conducted to compare the simulated noise with the measurement. Comparing the magnitude (Tables 3.2 to 3.6) and spatial frequency (Figures 3.6 and 3.14) of the simulated noise with the measurements verified the accuracy of the proposed LdCT simulator in generating realistic LdCTs.

It should be pointed out that the imaging noise in measured LdCT may slightly differ from the simulation due to two facts. First, tube current modulation is commonly used in routine diagnostic CT examinations. The tube current modulation component did not exhibit predictable behavior. For example, the behavior of the system was not consistent when two scans were performed on the same object using the same acquisition protocol. In this study, LdCT reduction was conducted by dividing the tube current by a constant value, as illustrated in Figure 3.13. In real scenarios, however, a threshold might be considered to avoid very low tube load, therefore, the simulated LdCTs might be slightly noisier than the measured. Second, in order to account for the effect of beam hardening we assumed that the attenuation of the photons was due to water. In real scenarios, however, attenuation could also be due to denser materials such as bone. Nevertheless, comparing the simulations with the measurements showed that the relative error is less than 3%, showing the accuracy of the simulated LdCT.

7.2 LdCT for proton therapy

Employing the LdCT simulator enabled us to explore the effect of reducing CT imaging dose for each individual patient on different scanners using different acquisition protocols. LdCTs were first simulated and then used for different tasks in proton therapy, including proton therapy dose calculation and plan optimization, WET estimation, automated delineation of OARs, and manual delineation of the target volume.

We started by exploring the effect of CT noise on cases that required 3D planning CT in Chapter 4 and then moved to the esophageal and lung cancer cases that required 4DCT, in Chapter 5. Generally, reducing the CT imaging dose is more critical if a 4DCT is performed.

In total, one phantom study and twenty patient studies were conducted to assess the effect of reducing CT imaging dose, as discussed in Chapters 4 and 5. Each test started with simulating LdCTs with up to 90% reduction in the imaging dose. The dose reductions are relative to the standard clinical acquisition protocols that are currently used at the University Hospital in Leuven. The ground truth for each case was established by using the standard-dose CTs for the treatment planning. Subsequently, the same experiments were performed based on the simulated LdCTs. Comparing the results based on the simulated LdCTs with those based on the standard-dose CT images (ground truth) indicated the impact of reducing the CT imaging dose.

7.2.1 Dose calculation

The results suggested the possibility of using LdCTs for proton therapy dose calculation and plan optimization. Reducing CT imaging dose by 90% does not have a noticeable impact on proton therapy dose calculation. The doses based on LdCTs were almost identical to doses based on the standard-dose CTs where a gamma passing rate of around 100% was observed (Table 4.1 and Figures 5.7 and 5.8). For one of the cases (case 4 in Chapter 5), a larger error was observed. This was due to strong streak artifacts caused by photon starvation on the LdCTs, as shown in Figure 5.13. However, the results showed that 70% CT imaging dose reduction could still be achieved for this case.

7.2.2 Plan optimization

The plans optimized on LdCT were clinically equivalent to those optimized on the standard-dose CT. First, the DVHs based on LdCTs and standard-dose CTs were well aligned for the target volume and OARs, as represented in Figure 4.3 and 5.11. Second, the gamma passing rate (3%/3 mm) was above the required 90% threshold which is commonly used in clinics to consider two

doses equivalent (Table 4.2 and Figures 5.9 and 5.10). Third, the plans based on the LdCT (OptLow-CalcHigh) met the clinical goals. It should be noted that the plan optimization error was larger than the dose calculation test. This is due to the fact that this test is also affected by other random variations. In addition, plan optimization involved many iterations, therefore, a larger error was expected.

7.2.3 Delineation of anatomical structures

For the delineation of OARs, an auto-segmentation tool was employed. This is highly relevant for adaptive regimens where time is a constraint. For target volume delineation, the FDG-PET/CT images, which were acquired several days before the planning CT, were first registered to the planning CTs. A manual delineation of target volumes was then performed by an expert. Comparing the contours acquired from the LdCTs with the reference contours indicated that LdCTs can also be used for image delineation tasks (Figures 5.2 to 5.5 and Table 5.2). The errors due to CT noise (after reducing the CT imaging dose by 90%) were in the same order as the inter-observer variability for the majority of the anatomical structures (reported in Table 5.3), except for the brachial plexus (HD-95 of up to 6 cm in on case).

It should be noted that the delineation of the brachial plexus on CT images (even on standard-dose CT) can be challenging. The manual delineation of the brachial plexus on CT images can often only be done by relying on the surrounding structures as landmarks. It is recommended to use MR images instead, however, MR images are not always available. The higher level of CT noise on LdCTs might make the delineation of the brachial plexus even more challenging, therefore, less CT imaging dose reduction is recommended for the cases that require the delineation of the brachial plexus. In other words. the delineation of the brachial plexus can be considered a critical task. A critical task is the weakest link in the chain and ultimately determines how much dose can be reduced.

7.2.4 Final conclusion

It can be seen that reducing CT imaging dose by 90% does not have a significant impact on proton therapy treatment planning. However, the radiation oncologist (who manually delineated target volumes for esophageal cancer cases) reported a lower level of certainty for contours delineated on the LdCT than on the standard-dose CT. Therefore, less CT imaging dose reduction should be applied if manual delineation is performed.

Our findings were in close agreement with the findings of other teams investigating the possibility of using LdCT in adaptive proton therapy workflows [133, 145]. Unlike our study, these two studies mapped OARs and

target volumes from the planning CT using deformable image registration. According to their studies, LdCT protocols are also suitable for image registration tasks. As compared to these studies, our study has the advantage of, first, using realistic LdCTs (simulated from patient data using a more accurate noise model) and, second, exploring the effect of CT noise on different tasks in proton therapy.

To sum up, our results suggest the possibility of using LdCT protocols for adaptive workflows. This is mainly due to the fact that conventional CT protocols have been optimized to detect small CT-number [HU] differences at a high spatial resolution. This is not necessarily a requirement for adaptive proton therapy. For example, proton therapy dose calculation uses a voxel size of 3 mm, which indicates that the resolution of standard CT images (0.6 to 1 mm) is actually higher than needed. The second reason is that the accumulation of CT noise through integration along a beam (which is a key quantity in proton therapy) is small. For example, the WET maps estimated from the LdCT were almost identical to those calculated from the standard-dose CT. As shown in Figure 4.6 and Table 4.3, the absolute and relative errors were smaller than 1 mm and 1%, respectively.

7.3 LdCT denoiser

In Chapter 6, a CNN for CT denoising, based on ResUNet architecture, was developed and trained to denoise LdCTs. The training was performed using standard-dose CT and the corresponding simulated LdCT pairs. The results demonstrated that the developed network can successfully suppress CT noise, as shown in Figures 6.7 and 6.8. Denoising LdCTs with the developed network resulted in lower MAE and higher SSIM and PSNR, reported in Table 6.1. Subsequently, the denoised LdCTs were used for proton therapy dose calculation, plan optimization, and the delineation of OARs. Results based on denoised LdCTs (slightly) outperformed those based on (non-denoised) LdCTs. This suggests that further dose reduction might be achieved by employing a sophisticated LdCT denoiser.

7.4 Future Perspectives

In this thesis, the possibility of using LdCT imaging protocols for accurate proton therapy treatment planning was explored. The topic still needs to be addressed in several ways. This section discusses different directions and related questions to be further explored in future research.

7.4.1 LdCT simulation

The effect of reducing the CT imaging dose by up to 90% was explored in this study. Reducing the CT dose beyond 90% is theoretically possible, however, performing a clinical CT scan below that level is usually not possible and requires access to the service mode. More aggressive dose reduction might be achievable by increasing the CT gantry speed (a shorter acquisition time) or increasing pitch in helical CTs. A promising direction is to reduce the CT imaging dose beyond 90% (until the model fails) to determine the lowest CT imaging dose that produces accurate proton dose calculations.

As discussed in Section 3.2.6, if the number of detected photons is smaller than a predefined threshold, the transmitted signals will be smoothed by the signal-dependent filter (SDF). This filter is applied in the sinogram domain. Applying this filter may result in underestimation of HU in the high attenuated areas (bone) and the overestimation of HU in the low attenuated areas (air cavities). Bias in estimating HU can severely affect proton therapy dose calculation. In Section 5.2.3 and 4.3.1, it was shown that the effect of reducing CT imaging dose, and therefore the effect of applying the SDF, is negligible for proton therapy dose calculation. Yet, it is worth investigating the effect of applying the smoothing filter on HU estimation. This requires access to the service mode on the scanners. It is discussed in Section 3.3.2 that switching off this filter results in noisier LdCT images. Yet, the results on proton dose calculation might be improved if deactivating this filter results in a lower bias on the estimation HU.

The effect of the smoothing filter can be tested by scanning a Gammex phantom. The Gammex phantom is a large circular disk of "solid water". It consists of a matrix of 16 holes in the disk that hold cylinders with tissue-mimicking materials, as shown in Figure 7.1. The Gammex phantom is commonly used in radiotherapy centers to estimate the HU-to-density curve. A small test was carried out to explore the effect of the smoothing filter. The Gammex phantom was scanned twice using the standard-dose and LdCT protocols. The HU measured from the LdCT was then compared with that of the standard-dose CT for each cylinder. Each cylinder can be divided into two parts: the part that is located in the disk (surrounded by the disk), and the part that pops out of the disk (surrounded by the air). The results showed that lowering the CT imaging dose does not have any impact on the estimation of the HU for the part of the cylinder that is surrounded by the air. However, as expected, a bias was observed for the part of the cylinder that is surrounded by the water disk. The HU was underestimated for the high attenuated cylinder and overestimated for the low attenuated cylinder. In addition, the bias was increased by lowering the CT imaging dose. This could be due to the smoothing filter and also photon starvation and needs further investigation.

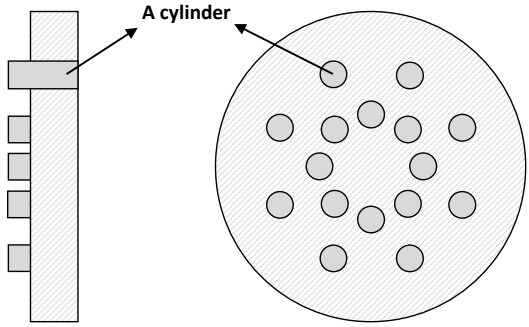

Figure 7.1: Illustration of the Gammex phantom. The Gammex phantom is commonly used in the clinical routine to calibrate CT-to-density conversion curve.

7.4.2 Proton therapy treatment planning

All the patient cases that were employed in this study were adult cases who underwent photon therapy. This was due to the limited number of adult patients in our proton therapy center. As the first step, a realistic proton plan was defined for each case by an expert. We strongly believe that our findings can be generalized to adult cancer patients receiving proton therapy. As already mentioned, pediatric cases benefit more from LdCT protocols and it is highly recommended to minimize the CT imaging dose for children. However, generalizing the findings for pediatric cases needs further investigation. This is especially true for the delineation of target volumes and OARs due to the differences in the anatomy of pediatric and adult cases. That being said, the findings for the dose calculation and plan optimization tests can be generalized to pediatrics. However, a detailed study on the effect of lowering CT imaging dose for children would benefit the proton therapy community.

This thesis explores the effects of reducing CT imaging dose on different tasks in adaptive proton therapy. It is important to mention that image registration could be affected by CT noise, but this has not been discussed in this thesis due to the lack of data. In adaptive workflows, image registration is often required, for example, to map the contours from the planning CT to the repeated CTs. Our hypothesis is that CT noise would not affect the rigid image registration dramatically, for example for head and neck cases. However, it could impact deformable image registration to some extent. The impact of CT noise on image registration could be another interesting direction that needs further investigation. It should be noted that for the manual delineation of target volumes, the FDG-PET/CT images were first

registered to the planning CTs (standard-dose and low-dose CTs). Therefore the effect of reducing CT imaging dose on deformable image registration was partially included in the manual delineation of target volumes.

In this study, the effect of CT imaging noise on robustness evaluation has not been investigated. Robustness evaluation assesses the robustness of a plan against uncertainties in density and patient setup. Typically, several scenarios with different uncertainty settings are defined. A robust plan is expected to produce acceptable dose distribution under most of the potential scenarios. Higher level of noise on LdCTs may make it more challenging to meet clinical goals if robustness evaluation is employed.

Finally, the effect of CT noise on different tasks was examined separately. The effect of CT noise is small for different tasks in the majority of cases. Nevertheless, it would be interesting to combine all these errors to investigate the effect of CT noise on proton therapy treatment planning.

7.4.3 Delineation of anatomical structures

Automated image delineation softwares are typically trained using standard-dose CT images (training samples) and manual contours (training labels). It would be, however, beneficial to include realistic LdCT images in the training. In order to improve the robustness of the models, Gaussian noise is typically added to the training samples (a process also known as data augmentation). However, a simple Gaussian noise is not a good representation of the CT noise. We believe that the results on the auto-delineation of OARs can be improved by incorporating realistic LdCT images in the training.

7.4.4 LdCT denoising

For training the CT denoiser, the loss function was defined by combining two conventional losses: MAE and SSIM. It is important to select the loss function based on the application of the denoised image because CT denoisers are heavily affected by the loss function. For example, edge-preserving losses might be a better option if the denoised images are used for manual image delineation. It would therefore be interesting to study the most effective loss function for proton therapy in future studies.

The CNN-based LdCT denoiser was trained using standard-dose and LdCT pairs. In adaptive proton therapy, however, the CT images will be repeated several times through the course of treatment. The sequence of these repeated CT images provides substantial patient-specific prior information which can be used for image denoising. Denoising can be achieved during image reconstruction by incorporating the prior information into a prior-image-based tomographic reconstruction [206, 207] or even by

training a CNN-based LdCT denoiser [208]. This would be particularly beneficial for LdCTs with severe photon starvation.

In prior-image-based reconstruction methods, the objective function is generally defined by combining the data-fidelity term (projection data) with the regularization term (prior knowledge). Combining these two terms requires manual tuning. For example, the data-fidelity term should be given a higher weight if the reconstructed images will be used for proton therapy dose calculation. This is due to the fact that the reconstructed images should be a faithful representation of the current patient geometry. On the other hand, a higher weight for the regularization term might be desirable if the reconstructed images are used for the delineation of soft tissue. Therefore, tuning the weights to reconstruct one image that is suitable for different applications might be challenging and needs further investigation.

Bibliography

[1] P. Christopher, E. Weiderpass, and W. S. Bernard, "World cancer report cancer research for cancer prevention," *International Agency for Research on Cancer: Lyon, France*, 2020.

[2] B. Cao, F. Bray, A. Ilbawi, and I. Soerjomataram, "Effect on longevity of one-third reduction in premature mortality from non-communicable diseases by 2030: a global analysis of the sustainable development goal health target," *The Lancet Global Health*, vol. 6, no. 12, pp. e1288–e1296, 2018.

[3] T. Dyba, G. Randi, F. Bray, C. Martos, F. Giusti, N. Nicholson, A. Gavin, M. Flego, L. Neamtiu, N. Dimitrova, *et al.*, "The european cancer burden in 2020: Incidence and mortality estimates for 40 countries and 25 major cancers," *European Journal of Cancer*, vol. 157, pp. 308–347, 2021.

[4] T. Dyba, G. Randi, C. Martos, F. Giusti, R. Calvalho, L. Neamtiu, N. Nicholson, M. Flego, N. Dimitrova, and M. Bettio, "Long-term estimates of cancer incidence and mortality for the eu and efta countries according to different demographic scenarios," *Annals of Oncology*, vol. 32, p. S1102, 2021.

[5] P. Ahluwalia, B. Gupta, *et al.*, "Can we dream of an integrated pain management app for cancer patients?," *Indian Journal of Cancer*, vol. 59, no. 1, p. 132, 2022.

[6] R. A. Patchell, P. A. Tibbs, J. W. Walsh, R. J. Dempsey, Y. Maruyama, R. J. Kryscio, W. R. Markesbery, J. S. Macdonald, and B. Young, "A randomized trial of surgery in the treatment of single metastases to the brain," *New England Journal of Medicine*, vol. 322, no. 8, pp. 494–500, 1990.

[7] G. Delaney, S. Jacob, C. Featherstone, and M. Barton, "The role of radiotherapy in cancer treatment: estimating optimal utilization from a review of evidence-based clinical guidelines," *Cancer: Interdisciplinary International Journal of the American Cancer Society*, vol. 104, no. 6, pp. 1129–1137, 2005.

[8] A. C. Begg, F. A. Stewart, and C. Vens, "Strategies to improve radiotherapy with targeted drugs," *Nature Reviews Cancer*, vol. 11, no. 4, pp. 239–253, 2011.

[9] R. Baskar, K. A. Lee, R. Yeo, and K.-W. Yeoh, "Cancer and radiation therapy: current advances and future directions," *International journal of medical sciences*, vol. 9, no. 3, p. 193, 2012.

[10] I. M. R. T. C. W. Group *et al.*, "Intensity-modulated radiotherapy: current status and issues of interest," *International Journal of Radiation Oncology*Biology*Physics*, vol. 51, no. 4, pp. 880–914, 2001.

[11] C. Nutting, D. Dearnaley, and S. Webb, "Intensity modulated radiation therapy: a clinical review.," *The British journal of radiology*, vol. 73, no. 869, pp. 459–469, 2000.

[12] E. J. Hall, "Intensity-modulated radiation therapy, protons, and the risk of second cancers," *International Journal of Radiation Oncology* Biology* Physics*, vol. 65, no. 1, pp. 1–7, 2006.

[13] D. Followill, P. Geis, and A. Boyer, "Estimates of whole-body dose equivalent produced by beam intensity modulated conformal therapy.," *International journal of radiation oncology, biology, physics*, vol. 38, no. 3, pp. 667–672, 1997.

[14] S. F. Kry, M. Salehpour, D. S. Followill, M. Stovall, D. A. Kuban, R. A. White, and I. I. Rosen, "The calculated risk of fatal secondary malignancies from intensity-modulated radiation therapy," *International Journal of Radiation Oncology* Biology* Physics*, vol. 62, no. 4, pp. 1195–1203, 2005.

[15] L. Nenoff, *Daily adaptive proton therapy: challenges and clinical potential*. PhD thesis, ETH Zurich, 2020.

[16] R. R. Wilson, "Radiological use of fast protons," *Radiology*, vol. 47, no. 5, pp. 487–491, 1946.

[17] PTCOG, "Statistics of patients treated in particle therapy facilities worldwide," 2022.

[18] H. Paganetti, *Proton Beam Therapy*. 2399-2891, IOP Publishing, 2017.

[19] K. A. Higgins, K. O'Connell, Y. Liu, T. W. Gillespie, M. W. McDonald, R. N. Pillai, K. R. Patel, P. R. Patel, C. G. Robinson, C. B. Simone II, *et al.*, "National cancer database analysis of proton versus photon radiation therapy in non-small cell lung cancer," *International Journal of Radiation Oncology* Biology* Physics*, vol. 97, no. 1, pp. 128–137, 2017.

[20] H. Paganetti, "Range uncertainties in proton therapy and the role of monte carlo simulations," *Physics in Medicine & Biology*, vol. 57, no. 11, p. R99, 2012.

[21] H. Paganetti, P. Botas, G. C. Sharp, and B. Winey, "Adaptive proton therapy," *Physics in Medicine & Biology*, vol. 66, no. 22, p. 22TR01, 2021.

[22] M. Engelsman, S. J. Rosenthal, S. L. Michaud, J. A. Adams, R. J. Schneider, S. G. Bradley, J. B. Flanz, and H. M. Kooy, "Intra-and interfractional patient motion for a variety of immobilization devices," *Medical physics*, vol. 32, no. 11, pp. 3468–3474, 2005.

[23] A. J. Wroe, D. A. Bush, and J. D. Slater, "Immobilization considerations for proton radiation therapy," *Technology in Cancer Research & Treatment*, vol. 13, no. 3, pp. 217–226, 2014.

[24] S. Michiels, A. D'Hollander, N. Lammens, M. Kersemans, G. Zhang, J.-M. Denis, K. Poels, E. Sterpin, S. Nuyts, K. Haustermans, *et al.*, "Towards 3d printed multifunctional immobilization for proton therapy: initial materials characterization," *Medical Physics*, vol. 43, no. 10, pp. 5392–5402, 2016.

[25] U. Schneider, E. Pedroni, and A. Lomax, "The calibration of ct hounsfield units for radiotherapy treatment planning," *Physics in Medicine & Biology*, vol. 41, no. 1, p. 111, 1996.

[26] A. Meijers, J. Free, D. Wagenaar, S. Deffet, A.-C. Knopf, J. A. Langendijk, and S. Both, "Validation of the proton range accuracy and optimization of ct calibration curves utilizing range probing," *Physics in Medicine & Biology*, vol. 65, no. 3, p. 03NT02, 2020.

[27] H. H. Lee, B. Li, X. Duan, L. Zhou, X. Jia, and M. Yang, "Systematic analysis of the impact of imaging noise on dual-energy ct-based proton stopping power ratio estimation," *Medical physics*, vol. 46, no. 5, pp. 2251–2263, 2019.

[28] C. Richter and P. Wohlfahrt, "Dual-energy ct in radiation oncology," in *Spectral Imaging*, pp. 333–346, Springer, 2022.

[29] P. Wohlfahrt and C. Richter, "Status and innovations in pre-treatment ct imaging for proton therapy," *The British journal of radiology*, vol. 93, no. 1107, p. 20190590, 2020.

[30] B. Perumal, H. E. Sundaresan, and R. Vaitheeswaran, "A pilot study on the comparison between planning target volume-based intensity-modulated proton therapy plans and robustly optimized intensity-modulated proton therapy plans," *Journal of Medical Physics*, vol. 43, no. 3, p. 179, 2018.

[31] M. Cubillos-Mesías, E. G. Troost, F. Lohaus, L. Agolli, M. Rehm, C. Richter, and K. Stützer, "Including anatomical variations in robust optimization for head and neck proton therapy can reduce the need of adaptation," *Radiotherapy and Oncology*, vol. 131, pp. 127–134, 2019.

[32] R. Malyapa, M. Lowe, A. Bolsi, A. J. Lomax, D. C. Weber, and F. Albertini, "Evaluation of robustness to setup and range uncertainties for head and neck patients treated with pencil beam scanning proton therapy," *International Journal of Radiation Oncology* Biology* Physics*, vol. 95, no. 1, pp. 154–162, 2016.

[33] S. McGowan, N. Burnet, and A. Lomax, "Treatment planning optimisation in proton therapy," *The British journal of radiology*, vol. 86, no. 1021, pp. 20120288–20120288, 2013.

[34] F. Albertini, M. Matter, L. Nenoff, Y. Zhang, and A. Lomax, "Online daily adaptive proton therapy," *The British Journal of Radiology*, vol. 93, p. 20190594, Mar. 2020.

[35] A. J. Lomax, "Myths and realities of range uncertainty," *The British Journal of Radiology*, vol. 93, p. 20190582, Mar. 2020.

[36] J.-J. Sonke, M. Aznar, and C. Rasch, "Adaptive radiotherapy for anatomical changes," *Seminars in Radiation Oncology*, vol. 29, pp. 245–257, July 2019.

[37] A. Lalonde, M. Bobić, B. Winey, J. Verburg, G. C. Sharp, and H. Paganetti, "Anatomic changes in head and neck intensity-modulated proton therapy: Comparison between robust optimization and online adaptation," *Radiotherapy and Oncology*, vol. 159, pp. 39–47, 2021.

[38] Z. Yang, X. Zhang, X. Wang, X. R. Zhu, B. Gunn, S. J. Frank, Y. Chang, Q. Li, K. Yang, G. Wu, *et al.*, "Multiple-ct optimization: an adaptive optimization method to account for anatomical changes in intensity-modulated proton therapy for head and neck cancers," *Radiotherapy and Oncology*, vol. 142, pp. 124–132, 2020.

[39] D. Yan, F. Vicini, J. Wong, and A. Martinez, "Adaptive radiation therapy," *Physics in Medicine and Biology*, vol. 42, pp. 123–132, Jan. 1997.

[40] L. Hoffmann, M. Alber, M. F. Jensen, M. I. Holt, and D. S. Møller, "Adaptation is mandatory for intensity modulated proton therapy of advanced lung cancer to ensure target coverage," *Radiotherapy and Oncology*, vol. 122, no. 3, pp. 400–405, 2017.

[41] T. Lomax, "Treatment planning for scanned particle beams," in *Proton and Carbon Ion Therapy*, pp. 167–188, CRC Press, 2012.

[42] A. J. van de Schoot, P. de Boer, K. F. Crama, J. Visser, L. J. Stalpers, C. R. Rasch, and A. Bel, "Dosimetric advantages of proton therapy compared with photon therapy using an adaptive strategy in cervical cancer," *Acta Oncologica*, vol. 55, no. 7, pp. 892–899, 2016.

[43] J. Heukelom and C. D. Fuller, "Head and neck cancer adaptive radiation therapy (art): conceptual considerations for the informed clinician," in *Seminars in radiation oncology*, vol. 29, pp. 258–273, Elsevier, 2019.

[44] C. L. Brouwer, R. J. Steenbakkers, J. A. Langendijk, and N. M. Sijtsema, "Identifying patients who may benefit from adaptive radiotherapy: Does the literature on anatomic and dosimetric changes in head and neck organs at risk during radiotherapy provide information to help?," *Radiotherapy and Oncology*, vol. 115, no. 3, pp. 285–294, 2015.

[45] O. Hamming-Vrieze, S. R. van Kranen, W. D. Heemsbergen, C. A. Lange, M. W. van den Brekel, M. Verheij, C. R. Rasch, and J. J. Sonke, "Analysis of gtv reduction during radiotherapy for oropharyngeal cancer: Implications for adaptive radiotherapy," *Radiotherapy and Oncology*, vol. 122, no. 2, pp. 224–228, 2017.

[46] H. Paganetti, C. Beltran, S. Both, L. Dong, J. Flanz, K. Furutani, C. Grassberger, D. R. Grosshans, A.-C. Knopf, J. A. Langendijk, *et al.*, "Roadmap: proton therapy physics and biology," *Physics in Medicine & Biology*, vol. 66, no. 5, p. 05RM01, 2021.

[47] K. P. Nesteruk, M. Bobić, A. Lalonde, B. A. Winey, A. J. Lomax, and H. Paganetti, "CT-on-rails versus in-room CBCT for online daily adaptive proton therapy of head-and-neck cancers," *Cancers*, vol. 13, p. 5991, Nov. 2021.

[48] C.-M. C. Ma and K. Paskalev, "In-room ct techniques for image-guided radiation therapy," *Medical dosimetry*, vol. 31, no. 1, pp. 30–39, 2006.

[49] W. van Elmpt, G. Landry, M. Das, and F. Verhaegen, "Dual energy ct in radiotherapy: current applications and future outlook," *Radiotherapy and Oncology*, vol. 119, no. 1, pp. 137–144, 2016.

[50] A. Thummerer, P. Zaffino, A. Meijers, G. G. Marmitt, J. Seco, R. J. Steenbakkers, J. A. Langendijk, S. Both, M. F. Spadea, and A. C. Knopf, "Comparison of cbct based synthetic ct methods suitable for proton dose calculations in adaptive proton therapy," *Physics in Medicine & Biology*, vol. 65, no. 9, p. 095002, 2020.

[51] V. Giacometti, A. R. Hounsell, and C. K. McGarry, "A review of dose calculation approaches with cone beam ct in photon and proton therapy," *Physica Medica*, vol. 76, pp. 243–276, 2020.

[52] J. Uh, C. Wang, S. Acharya, M. J. Krasin, and C.-h. Hua, "Training a deep neural network coping with diversities in abdominal and pelvic images of children and young adults for cbct-based adaptive proton therapy," *Radiotherapy and Oncology*, vol. 160, pp. 250–258, 2021.

[53] L. Koivula, L. Wee, and J. Korhonen, "Feasibility of mri-only treatment planning for proton therapy in brain and prostate cancers: dose calculation accuracy in substitute ct images," *Medical Physics*, vol. 43, no. 8Part1, pp. 4634–4642, 2016.

[54] A. Hoffmann, B. Oborn, M. Moteabbed, S. Yan, T. Bortfeld, A. Knopf, H. Fuchs, D. Georg, J. Seco, M. F. Spadea, *et al.*, "Mr-guided proton therapy: a review and a preview," *Radiation Oncology*, vol. 15, no. 1, pp. 1–13, 2020.

[55] S. Kazemifar, S. McGuire, R. Timmerman, Z. Wardak, D. Nguyen, Y. Park, S. Jiang, and A. Owrangi, "Mri-only brain radiotherapy: Assessing the dosimetric accuracy of synthetic ct images generated using a deep learning approach," *Radiotherapy and Oncology*, vol. 136, pp. 56–63, 2019.

[56] S. Kazemifar, A. M. Barragán Montero, K. Souris, S. T. Rivas, R. Timmerman, Y. K. Park, S. Jiang, X. Geets, E. Sterpin, and A. Owrangi, "Dosimetric evaluation of synthetic ct generated with gans for mri-only proton therapy treatment planning of brain tumors," *Journal of applied clinical medical physics*, vol. 21, no. 5, pp. 76–86, 2020.

[57] R. Smith-Bindman, J. Lipson, R. Marcus, K.-P. Kim, M. Mahesh, R. Gould, A. B. De González, and D. L. Miglioretti, "Radiation dose associated with common computed tomography examinations and the associated lifetime attributable risk of cancer," *Archives of internal medicine*, vol. 169, no. 22, pp. 2078–2086, 2009.

[58] E. Hall and D. Brenner, "Cancer risks from diagnostic radiology," *The British journal of radiology*, vol. 81, no. 965, pp. 362–378, 2008.

[59] M. Brambilla, J. Vassileva, A. Kuchcinska, and M. M. Rehani, "Multinational data on cumulative radiation exposure of patients from recurrent radiological procedures: call for action," *European radiology*, vol. 30, no. 5, pp. 2493–2501, 2020.

[60] W. Rühm and R. Harrison, "High ct doses return to the agenda," 2020.

[61] A. B. De González, M. Mahesh, K.-P. Kim, M. Bhargavan, R. Lewis, F. Mettler, and C. Land, "Projected cancer risks from computed tomographic scans performed in the united states in 2007," *Archives of internal medicine*, vol. 169, no. 22, pp. 2071–2077, 2009.

[62] J. P. Sheppard, T. Nguyen, Y. Alkhalid, J. S. Beckett, N. Salamon, and I. Yang, "Risk of brain tumor induction from pediatric head CT procedures: A systematic literature review," *Brain Tumor Research and Treatment*, vol. 6, no. 1, p. 1, 2018.

[63] D. J. Brenner, C. D. Elliston, E. J. Hall, W. E. Berdon, *et al.*, "Estimated risks of radiation-induced fatal cancer from pediatric ct," *American journal of roentgenology*, vol. 176, no. 2, pp. 289–296, 2001.

[64] A. S. Brody, D. P. Frush, W. Huda, R. L. Brent, and S. on Radiology, "Radiation risk to children from computed tomography," *Pediatrics*, vol. 120, no. 3, pp. 677–682, 2007.

[65] M. S. Pearce, J. A. Salotti, M. P. Little, K. McHugh, C. Lee, K. P. Kim, N. L. Howe, C. M. Ronckers, P. Rajaraman, A. W. Craft, L. Parker, and A. B. de González, "Radiation exposure from CT scans in childhood and subsequent risk of leukaemia and brain tumours: a retrospective cohort study," *The Lancet*, vol. 380, pp. 499–505, Aug. 2012.

[66] R. De Jong, E. Lens, M. Van Herk, T. Alderliesten, M. Kamphuis, R. D. Fajardo, A. Bel, and N. Van Wieringen, "Oc-0282: Optimizing cone-beam ct presets for children to reduce imaging dose illustrated with craniospinal axis," *Radiotherapy and Oncology*, no. 111, pp. S109–S110, 2014.

[67] C. B. Hess, H. M. Thompson, S. H. Benedict, J. A. Seibert, K. Wong, A. T. Vaughan, and A. M. Chen, "Exposure risks among children undergoing radiation therapy: Considerations in the era of image guided radiation therapy," *International Journal of Radiation Oncology*Biology*Physics*, vol. 94, pp. 978–992, Apr. 2016.

[68] J. D. Mathews, A. V. Forsythe, Z. Brady, M. W. Butler, S. K. Goergen, G. B. Byrnes, G. G. Giles, A. B. Wallace, P. R. Anderson, T. A. Guiver, P. McGale, T. M. Cain, J. G. Dowty, A. C. Bickerstaffe, and S. C. Darby, "Cancer risk in 680 000 people exposed to computed tomography scans in

childhood or adolescence: data linkage study of 11 million australians," *BMJ*, vol. 346, pp. f2360–f2360, May 2013.

[69] M.-O. Bernier, H. Baysson, M. S. Pearce, M. Moissonnier, E. Cardis, M. Hauptmann, L. Struelens, J. Dabin, C. Johansen, N. Journy, *et al.*, "Cohort profile: the epi-ct study: a european pooled epidemiological study to quantify the risk of radiation-induced cancer from paediatric ct," *International Journal of Epidemiology*, vol. 48, no. 2, pp. 379–381g, 2019.

[70] M. M. Rehani, E. R. Melick, R. M. Alvi, R. Doda Khera, S. Batool-Anwar, T. G. Neilan, and M. Bettmann, "Patients undergoing recurrent ct exams: assessment of patients with non-malignant diseases, reasons for imaging and imaging appropriateness," *European radiology*, vol. 30, no. 4, pp. 1839–1846, 2020.

[71] W. Huang, C. Muo, C. Lin, Y. Jen, M. Yang, J. Lin, F. Sung, and C. Kao, "Paediatric head ct scan and subsequent risk of malignancy and benign brain tumour: a nation-wide population-based cohort study," *British journal of cancer*, vol. 110, no. 9, pp. 2354–2360, 2014.

[72] M. P. Little, R. Wakeford, S. D. Bouffler, K. Abalo, M. Hauptmann, N. Hamada, and G. M. Kendall, "Review of the risk of cancer following low and moderate doses of sparsely ionising radiation received in early life in groups with individually estimated doses," *Environment International*, vol. 159, p. 106983, 2022.

[73] F. Lück, D. Kolditz, M. Hupfer, and W. A. Kalender, "Effect of shaped filter design on dose and image quality in breast ct," *Physics in Medicine & Biology*, vol. 58, no. 12, p. 4205, 2013.

[74] N. Mail, D. Moseley, J. Siewerdsen, and D. Jaffray, "The influence of bowtie filtration on cone-beam ct image quality," *Medical physics*, vol. 36, no. 1, pp. 22–32, 2009.

[75] L. Yu, X. Liu, S. Leng, J. M. Kofler, J. C. Ramirez-Giraldo, M. Qu, J. Christner, J. G. Fletcher, and C. H. McCollough, "Radiation dose reduction in computed tomography: techniques and future perspective," *Imaging in medicine*, vol. 1, no. 1, p. 65, 2009.

[76] M. J. Willemink, M. Persson, A. Pourmorteza, N. J. Pelc, and D. Fleischmann, "Photon-counting ct: technical principles and clinical prospects," *Radiology*, vol. 289, no. 2, pp. 293–312, 2018.

[77] C. H. McCollough, "Automatic exposure control in ct: are we done yet?," *Radiology*, vol. 237, no. 3, pp. 755–756, 2005.

[78] J. R. Perks, J. Lehmann, A. M. Chen, C. C. Yang, R. L. Stern, and J. A. Purdy, "Comparison of peripheral dose from image-guided radiation therapy (IGRT) using kV cone beam CT to intensity-modulated radiation therapy (IMRT)," *Radiotherapy and Oncology*, vol. 89, pp. 304–310, Dec. 2008.

[79] T. Jagt, S. Breedveld, S. van de Water, B. Heijmen, and M. Hoogeman, "Near real-time automated dose restoration in IMPT to compensate for daily tissue density variations in prostate cancer," *Physics in Medicine and Biology*, vol. 62, pp. 4254–4272, May 2017.

[80] K. Bernatowicz, X. Geets, A. Barragan, G. Janssens, K. Souris, and E. Sterpin, "Feasibility of online IMPT adaptation using fast, automatic and robust dose restoration," *Physics in Medicine & Biology*, vol. 63, p. 085018, Apr. 2018.

[81] E. B. Villarroel, X. Geets, and E. Sterpin, "Online adaptive dose restoration in intensity modulated proton therapy of lung cancer to account for inter-fractional density changes," *Physics and Imaging in Radiation Oncology*, vol. 15, pp. 30–37, July 2020.

[82] S. Mori, S. Ko, T. Ishii, and K. Nishizawa, "Effective doses in four-dimensional computed tomography for lung radiotherapy planning," *Medical Dosimetry*, vol. 34, no. 1, pp. 87–90, 2009.

[83] R. A. Hälg, J. Besserer, and U. Schneider, "Systematic measurements of whole-body imaging dose distributions in image-guided radiation therapy," *Medical physics*, vol. 39, no. 12, pp. 7650–7661, 2012.

[84] S. Singh, M. K. Kalra, M. A. Moore, R. Shailam, B. Liu, T. L. Toth, E. Grant, and S. J. Westra, "Dose reduction and compliance with pediatric ct protocols adapted to patient size, clinical indication, and number of prior studies," *Radiology*, vol. 252, no. 1, pp. 200–208, 2009.

[85] L. S. Guimarães, J. G. Fletcher, W. S. Harmsen, L. Yu, H. Siddiki, Z. Melton, J. E. Huprich, D. Hough, R. Hartman, and C. H. McCollough, "Appropriate patient selection at abdominal dual-energy ct using 80 kv: relationship between patient size, image noise, and image quality," *Radiology*, vol. 257, no. 3, pp. 732–742, 2010.

[86] N. Sollmann, K. Mei, D. M. Hedderich, C. Maegerlein, F. K. Kopp, M. T. Löffler, C. Zimmer, E. J. Rummeny, J. S. Kirschke, T. Baum, *et al.*, "Multi-detector ct imaging: impact of virtual tube current reduction and sparse sampling on detection of vertebral fractures," *European radiology*, pp. 1–11, 2019.

[87] M. Cros, R. M. Joemai, J. Geleijns, D. Molina, and M. Salvadó, "Simdosect: dose reporting software based on monte carlo simulation for a 320 detector-row cone-beam ct scanner and icrp computational adult phantoms," *Physics in Medicine & Biology*, vol. 62, no. 15, p. 6304, 2017.

[88] A. Mittone, A. Bravin, and P. Coan, "Radiation dose in breast ct imaging with monochromatic x-rays: simulation study of the influence of energy, composition and thickness," *Physics in Medicine & Biology*, vol. 59, no. 9, p. 2199, 2014.

[89] C. Won Kim and J. H. Kim, "Realistic simulation of reduced-dose ct with noise modeling and sinogram synthesis using dicom ct images," *Medical physics*, vol. 41, no. 1, 2014.

[90] C. W. Kim and J. H. Kim, "Application of ct simulation technique for virtual ultra-low-dose trial in ct colonography," in *International MICCAI Workshop on Computational and Clinical Challenges in Abdominal Imaging*, pp. 49–57, Springer, 2012.

[91] A. S. Wang, C. Feng, and N. J. Pelc, "Image-based synthetic ct: simulating arbitrary low dose single and dual energy protocols from dual energy images," in *Medical Imaging 2012: Physics of Medical Imaging*, vol. 8313, p. 83131G, International Society for Optics and Photonics, 2012.

[92] A. Neverauskiene, M. Maciusovic, M. Burkanas, B. Griciene, L. Petkevicius, L. Zaleckas, A. Tamosiunas, and J. Venius, "Image based simulation of the low dose computed tomography images suggests 13 mas 120 kv suitability for non-syndromic craniosynostosis diagnosis without iterative reconstruction algorithms," *European journal of radiology*, vol. 105, pp. 168–174, 2018.

[93] P. Massoumzadeh, S. Don, C. F. Hildebolt, K. T. Bae, and B. R. Whiting, "Validation of ct dose-reduction simulation," *Medical physics*, vol. 36, no. 1, pp. 174–189, 2009.

[94] R. E. Naziroglu, V. F. van Ravesteijn, L. J. van Vliet, G. J. Streekstra, and F. M. Vos, "Simulation of scanner-and patient-specific low-dose ct imaging from existing ct images," *Physica Medica*, vol. 36, pp. 12–23, 2017.

[95] T. Takenaga, S. Katsuragawa, M. Goto, M. Hatemura, Y. Uchiyama, and J. Shiraishi, "A computer simulation method for low-dose ct images by use of real high-dose images: a phantom study," *Radiological physics and technology*, vol. 9, no. 1, pp. 44–52, 2016.

[96] B. R. Whiting, "Signal statistics in x-ray computed tomography," in *Medical Imaging 2002: Physics of Medical Imaging*, vol. 4682, pp. 53–61, International Society for Optics and Photonics, 2002.

[97] B. R. Whiting, P. Massoumzadeh, O. A. Earl, J. A. O'Sullivan, D. L. Snyder, and J. F. Williamson, "Properties of preprocessed sinogram data in x-ray computed tomography," *Medical physics*, vol. 33, no. 9, pp. 3290–3303, 2006.

[98] J. Nuyts, B. De Man, J. A. Fessler, W. Zbijewski, and F. J. Beekman, "Modelling the physics in the iterative reconstruction for transmission computed tomography," *Physics in Medicine & Biology*, vol. 58, no. 12, p. R63, 2013.

[99] J. R. Mayo, K. P. Whittall, A. N. Leung, T. E. Hartman, C. S. Park, S. L. Primack, G. K. Chambers, M. K. Limkeman, T. L. Toth, and S. H. Fox, "Simulated dose reduction in conventional chest ct: validation study.," *Radiology*, vol. 202, no. 2, pp. 453–457, 1997.

[100] D. P. Frush, C. C. Slack, C. L. Hollingsworth, G. S. Bisset, L. F. Donnelly, J. Hsieh, T. Lavin-Wensell, and J. R. Mayo, "Computer-simulated radiation dose reduction for abdominal multidetector ct of pediatric patients," *American Journal of Roentgenology*, vol. 179, no. 5, pp. 1107–1113, 2002.

[101] O. Amir, D. Braunstein, and A. Altman, "Dose optimization tool," in *Medical Imaging 2003: Visualization, Image-Guided Procedures, and Display*, vol. 5029, pp. 815–822, International Society for Optics and Photonics, 2003.

[102] P. Massoumzadeh, O. A. Earl, and B. R. Whiting, "Noise simulation in x-ray ct," in *Medical Imaging 2005: Physics of Medical Imaging*, vol. 5745, pp. 898–910, International Society for Optics and Photonics, 2005.

[103] L. Yu, M. Shiung, D. Jondal, and C. H. McCollough, "Development and validation of a practical lower-dose-simulation tool for optimizing computed tomography scan protocols," *Journal of computer assisted tomography*, vol. 36, no. 4, pp. 477–487, 2012.

[104] S. Žabić, Q. Wang, T. Morton, and K. M. Brown, "A low dose simulation tool for ct systems with energy integrating detectors," *Medical physics*, vol. 40, no. 3, 2013.

[105] D. Zeng, J. Huang, Z. Bian, S. Niu, H. Zhang, Q. Feng, Z. Liang, and J. Ma, "A simple low-dose x-ray ct simulation from high-dose scan," *IEEE transactions on nuclear science*, vol. 62, no. 5, pp. 2226–2233, 2015.

[106] A. S. Wang and N. J. Pelc, "Synthetic ct: Simulating low dose single and dual energy protocols from a dual energy scan," *Medical physics*, vol. 38, no. 10, pp. 5551–5562, 2011.

[107] A. S. Wang and N. J. Pelc, "Synthetic ct: Simulating arbitrary low dose single and dual energy protocols," in *Medical Imaging 2011: Physics of Medical Imaging*, vol. 7961, p. 79611R, International Society for Optics and Photonics, 2011.

[108] T. M. Benson and B. K. De Man, "Synthetic ct noise emulation in the raw data domain," in *IEEE Nuclear Science Symposuim & Medical Imaging Conference*, pp. 3169–3171, IEEE, 2010.

[109] J. Ma, Z. Liang, Y. Fan, Y. Liu, J. Huang, W. Chen, and H. Lu, "Variance analysis of x-ray ct sinograms in the presence of electronic noise background," *Medical physics*, vol. 39, no. 7Part1, pp. 4051–4065, 2012.

[110] J. Rong, P. Gao, W. Liu, Y. Zhang, T. Liu, and H. Lu, "Computer simulation of low-dose ct with clinical lung image database: a preliminary study," in *Medical Imaging 2017: Physics of Medical Imaging*, vol. 10132, p. 101322U, International Society for Optics and Photonics, 2017.

[111] E. Abadi, B. Harrawood, S. Sharma, A. Kapadia, W. P. Segars, and E. Samei, "Dukesim: A realistic, rapid, and scanner-specific simulation framework in computed tomography," *IEEE transactions on medical imaging*, vol. 38, no. 6, pp. 1457–1465, 2018.

[112] A. S. Wang, J. W. Stayman, Y. Otake, S. Vogt, G. Kleinszig, A. J. Khanna, G. L. Gallia, and J. H. Siewerdsen, "Low-dose preview for patient-specific, task-specific technique selection in cone-beam ct," *Medical physics*, vol. 41, no. 7, p. 071915, 2014.

[113] M. Elhamiasl and J. Nuyts, "Simulating lower-dose scans from an available CT scan," in *15th International Meeting on Fully Three-Dimensional Image Reconstruction in Radiology and Nuclear Medicine* (S. Matej and S. D. Metzler, eds.), SPIE, May 2019.

[114] P. J. La Riviere, "Penalized-likelihood sinogram smoothing for low-dose ct," *Medical physics*, vol. 32, no. 6Part1, pp. 1676–1683, 2005.

[115] I. A. Elbakri and J. A. Fessler, "Efficient and accurate likelihood for iterative image reconstruction in x-ray computed tomography," in *Medical Imaging 2003: Image Processing*, vol. 5032, pp. 1839–1851, International Society for Optics and Photonics, 2003.

[116] S. Strother, M. Casey, and E. Hoffman, "Measuring pet scanner sensitivity: relating countrates to image signal-to-noise ratios using noise equivalents counts," *Ieee transactions on nuclear science*, vol. 37, no. 2, pp. 783–788, 1990.

[117] J. Wang, H. Lu, Z. Liang, D. Eremina, G. Zhang, S. Wang, J. Chen, and J. Manzione, "An experimental study on the noise properties of x-ray ct sinogram data in radon space," *Physics in Medicine & Biology*, vol. 53, no. 12, p. 3327, 2008.

[118] M. Yavuz and J. A. Fessler, "Statistical image reconstruction methods for randoms-precorrected pet scans," *Medical Image Analysis*, vol. 2, no. 4, pp. 369–378, 1998.

[119] T. Flohr, K. Stierstorfer, R. Raupach, S. Ulzheimer, and H. Bruder, "Performance evaluation of a 64-slice ct system with z-flying focal spot," in *RöFo-Fortschritte auf dem Gebiet der Röntgenstrahlen und der bildgebenden Verfahren*, vol. 176, pp. 1803–1810, © Georg Thieme Verlag KG Stuttgart · New York, 2004.

[120] T. Flohr, K. Stierstorfer, S. Ulzheimer, H. Bruder, A. Primak, and C. H. McCollough, "Image reconstruction and image quality evaluation for a 64-slice ct scanner with-flying focal spot," *Medical physics*, vol. 32, no. 8, pp. 2536–2547, 2005.

[121] M. Kachelrieß, M. Knaup, C. Penßel, and W. A. Kalender, "Flying focal spot (ffs) in cone-beam ct," *IEEE transactions on nuclear science*, vol. 53, no. 3, pp. 1238–1247, 2006.

[122] K. Van Slambrouck and J. Nuyts, "Metal artifact reduction in computed tomography using local models in an image block-iterative scheme," *Medical physics*, vol. 39, no. 11, pp. 7080–7093, 2012.

[123] E. D. Hessen, L. D. van Buuren, J. A. Nijkamp, K. C. de Vries, W. K. Mok, L. Dewit, A. M. van Mourik, A. Berlin, U. A. van der Heide, and G. R. Borst, "Significant tumor shift in patients treated with stereotactic radiosurgery for brain metastasis," *Clinical and Translational Radiation Oncology*, vol. 2, pp. 23–28, Feb. 2017.

[124] M. Thomas, R. D. Roover, S. van der Merwe, M. Lambrecht, G. Defraene, and K. Haustermans, "The use of tumour markers in oesophageal cancer to quantify setup errors and baseline shifts during treatment," *Clinical and Translational Radiation Oncology*, vol. 26, pp. 8–14, Jan. 2021.

[125] A. J. Lomax, "Intensity modulated proton therapy and its sensitivity to treatment uncertainties 1: the potential effects of calculational

uncertainties," *Physics in Medicine and Biology*, vol. 53, pp. 1027–1042, Jan. 2008.

[126] L. Placidi, A. Bolsi, A. J. Lomax, R. A. Schneider, R. Malyapa, D. C. Weber, and F. Albertini, "Effect of anatomic changes on pencil beam scanned proton dose distributions for cranial and extracranial tumors," *International Journal of Radiation Oncology* Biology* Physics*, vol. 97, no. 3, pp. 616–623, 2017.

[127] J. Bertholet, G. Anastasi, D. Noble, A. Bel, R. van Leeuwen, T. Roggen, M. Duchateau, S. Pilskog, C. Garibaldi, N. Tilly, R. García-Mollá, J. Bonaque, U. Oelfke, M. C. Aznar, and B. Heijmen, "Patterns of practice for adaptive and real-time radiation therapy (POP-ART RT) part II: Offline and online plan adaption for interfractional changes," *Radiotherapy and Oncology*, vol. 153, pp. 88–96, Dec. 2020.

[128] L. Nenoff, M. Matter, A. G. Jarhall, C. Winterhalter, J. Gorgisyan, M. Josipovic, G. F. Persson, P. M. af Rosenschold, D. C. Weber, A. J. Lomax, and F. Albertini, "Daily adaptive proton therapy: Is it appropriate to use analytical dose calculations for plan adaption?," *International Journal of Radiation Oncology*Biology*Physics*, vol. 107, pp. 747–755, July 2020.

[129] S. Acharya, C. Wang, S. Quesada, M. A. Gargone, O. Ates, J. Uh, M. J. Krasin, T. E. Merchant, and C. ho Hua, "Adaptive proton therapy for pediatric patients: Improving the quality of the delivered plan with on-treatment MRI," *International Journal of Radiation Oncology*Biology*Physics*, vol. 109, pp. 242–251, Jan. 2021.

[130] C. Geng, Y. Han, X. Tang, D. Shu, C. Gong, and S. Altieri, "Evaluation of using the doppler shift effect of prompt gamma for measuring the carbon ion range in vivo for heterogeneous phantoms," *Nuclear Instruments and Methods in Physics Research Section A: Accelerators, Spectrometers, Detectors and Associated Equipment*, vol. 959, p. 163439, Apr. 2020.

[131] G. Anastasi, J. Bertholet, P. Poulsen, T. Roggen, C. Garibaldi, N. Tilly, J. T. Booth, U. Oelfke, B. Heijmen, and M. C. Aznar, "Patterns of practice for adaptive and real-time radiation therapy (POP-ART RT) part i: Intra-fraction breathing motion management," *Radiotherapy and Oncology*, vol. 153, pp. 79–87, Dec. 2020.

[132] T. Lomax, A. Bolsi, and F. Albertini, "Adaptive proton therapy utilizing an in-room ct," *Siemens Healthineers White Paper*, 2020.

[133] L. Nenoff, M. Matter, M. Charmillot, S. Krier, K. Uher, D. C. Weber, A. J. Lomax, and F. Albertini, "Experimental validation of daily adaptive

proton therapy," *Physics in Medicine & Biology*, vol. 66, p. 205010, Oct. 2021.

[134] M. Elhamiasl and J. Nuyts, "Low-dose x-ray CT simulation from an available higher-dose scan," *Physics in Medicine & Biology*, vol. 65, p. 135010, July 2020.

[135] S. Deffet, M. Cohilis, K. Souris, K. Salvo, T. Depuydt, E. Sterpin, and B. Macq, "openPR — a computational tool for CT conversion assessment with proton radiography," *Medical Physics*, vol. 48, pp. 387–396, Nov. 2020.

[136] M. Cohilis, E. Sterpin, J. A. Lee, and K. Souris, "A noise correction of the γ-index method for monte carlo dose distribution comparison," *Medical Physics*, vol. 47, pp. 681–692, Nov. 2019.

[137] G. A. Ezzell, J. W. Burmeister, N. Dogan, T. J. LoSasso, J. G. Mechalakos, D. Mihailidis, A. Molineu, J. R. Palta, C. R. Ramsey, B. J. Salter, J. Shi, P. Xia, N. J. Yue, and Y. Xiao, "IMRT commissioning: Multiple institution planning and dosimetry comparisons, a report from AAPM task group 119," *Medical Physics*, vol. 36, pp. 5359–5373, Oct. 2009.

[138] S. Brousmiche, K. Souris, J. O. de Xivry, J. A. Lee, B. Macq, and J. Seco, "Combined influence of CT random noise and HU-RSP calibration curve nonlinearities on proton range systematic errors," *Physics in Medicine & Biology*, vol. 62, pp. 8226–8245, Oct. 2017.

[139] V. S.-C. LEE, G. SchettIno, and A. Nisbet, "UK adaptive radiotherapy practices for head and neck cancer patients," *BJR|Open*, vol. 2, p. 20200051, Nov. 2020.

[140] E. Borderías-Villarroel, V. Taasti, W. V. Elmpt, S. Teruel-Rivas, X. Geets, and E. Sterpin, "Evaluation of the clinical value of automatic online dose restoration for adaptive proton therapy of head and neck cancer," *Radiotherapy and Oncology*, Mar. 2022.

[141] N. Yuan, J. Zhou, and J. Qi, "Half2half: deep neural network based CT image denoising without independent reference data," *Physics in Medicine & Biology*, vol. 65, p. 215020, Nov. 2020.

[142] M. Baumann, M. Krause, J. Overgaard, J. Debus, S. M. Bentzen, J. Daartz, C. Richter, D. Zips, and T. Bortfeld, "Radiation oncology in the era of precision medicine," *Nature Reviews Cancer*, vol. 16, no. 4, pp. 234–249, 2016.

[143] K. R. Gergelis, K. R. Jethwa, E. J. Tryggestad, J. B. Ashman, M. G. Haddock, and C. L. Hallemeier, "Proton beam radiotherapy for esophagus cancer: state of the art," *Journal of Thoracic Disease*, vol. 12, no. 11, p. 7002, 2020.

[144] M. Elhamiasl, K. Salvo, K. Poels, G. Defraene, M. Lambrecht, X. Geets, E. Sterpin, and J. Nuyts, "Low-dose ct allows for accurate proton therapy dose calculation and plan optimization," *Physics in Medicine & Biology*, vol. 67, no. 19, p. 195015, 2022.

[145] K. P. Nesteruk, M. Bobić, G. C. Sharp, A. Lalonde, B. A. Winey, L. Nenoff, A. J. Lomax, and H. Paganetti, "Low-dose computed tomography scanning protocols for online adaptive proton therapy of head-and-neck cancers," *Cancers*, vol. 14, no. 20, p. 5155, 2022.

[146] S. K. Vinod, M. G. Jameson, M. Min, and L. C. Holloway, "Uncertainties in volume delineation in radiation oncology: a systematic review and recommendations for future studies," *Radiotherapy and Oncology*, vol. 121, no. 2, pp. 169–179, 2016.

[147] F. Bray, J. Ferlay, I. Soerjomataram, R. L. Siegel, L. A. Torre, and A. Jemal, "Global cancer statistics 2018: Globocan estimates of incidence and mortality worldwide for 36 cancers in 185 countries," *CA: a cancer journal for clinicians*, vol. 68, no. 6, pp. 394–424, 2018.

[148] D. Boyce-Fappiano, Q.-N. Nguyen, B. V. Chapman, P. K. Allen, O. Gjyshi, T. A. Pezzi, B. De, D. Gomez, S. H. Lin, J. Y. Chang, *et al.*, "Single institution experience of proton and photon-based postoperative radiation therapy for non–small-cell lung cancer," *Clinical Lung Cancer*, vol. 22, no. 5, pp. e745–e755, 2021.

[149] C. G. Boer, K. Fjellanger, I. M. Sandvik, M. Ugland, G. M. Engeseth, and L. B. Hysing, "Substantial sparing of organs at risk with modern proton therapy in lung cancer, but altered breathing patterns can jeopardize target coverage," *Cancers*, vol. 14, no. 6, p. 1365, 2022.

[150] K. Yang, Y.-G. Suh, H. Shin, H. Pyo, S. H. Moon, Y. C. Ahn, D. Oh, E. Chung, K. Jo, and J. M. Noh, "Toxicity of proton therapy versus photon therapy on salvage re-irradiation for non-small cell lung cancer," *Life*, vol. 12, no. 2, p. 292, 2022.

[151] M. Xi, C. Xu, Z. Liao, J. Y. Chang, D. R. Gomez, M. Jeter, J. D. Cox, R. Komaki, R. Mehran, M. A. Blum, *et al.*, "Comparative outcomes after definitive chemoradiotherapy using proton beam therapy versus intensity modulated radiation therapy for esophageal cancer:

a retrospective, single-institutional analysis," *International Journal of Radiation Oncology* Biology* Physics*, vol. 99, no. 3, pp. 667–676, 2017.

[152] S. H. Lin, B. P. Hobbs, V. Verma, R. S. Tidwell, G. L. Smith, X. Lei, E. M. Corsini, I. Mok, X. Wei, L. Yao, *et al.*, "Randomized phase iib trial of proton beam therapy versus intensity-modulated radiation therapy for locally advanced esophageal cancer," *Journal of Clinical Oncology*, vol. 38, no. 14, p. 1569, 2020.

[153] B. C. Baumann, N. Mitra, J. G. Harton, Y. Xiao, A. P. Wojcieszynski, P. E. Gabriel, H. Zhong, H. Geng, A. Doucette, J. Wei, *et al.*, "Comparative effectiveness of proton vs photon therapy as part of concurrent chemoradiotherapy for locally advanced cancer," *JAMA oncology*, vol. 6, no. 2, pp. 237–246, 2020.

[154] L. Hoffmann, H. Mortensen, M. Shamshad, M. Berbee, N. Bizzocchi, R. Bütof, R. Canters, G. Defraene, M. L. Ehmsen, F. Fiorini, *et al.*, "Treatment planning comparison in the protect-trial randomising proton versus photon beam therapy in oesophageal cancer: Results from eight european centres," *Radiotherapy and Oncology*, vol. 172, pp. 32–41, 2022.

[155] M. Elhamiasl, K. Salvo, W. Coudyzer, and J. Nuyts, "Low-dose CT simulation from an available higher dose CT scan," in *2019 IEEE Nuclear Science Symposium and Medical Imaging Conference (NSS/MIC)*, IEEE, Oct. 2019.

[156] M. Elhamiasl, S. T. Rivas, K. Salvo, E. Sterpin, and J. Nuyts, "The effect of CT dose reduction on proton therapy dose calculation," in *6th International Conference on Image Formation in X-Ray Computed Tomography (CT Meeting)*, Aug. 2020.

[157] J. Van der Veen, S. Willems, S. Deschuymer, D. Robben, W. Crijns, F. Maes, and S. Nuyts, "Benefits of deep learning for delineation of organs at risk in head and neck cancer," *Radiotherapy and Oncology*, vol. 138, pp. 68–74, 2019.

[158] D. Ciardo, M. A. Gerardi, S. Vigorito, A. Morra, V. Dell'Acqua, F. J. Diaz, F. Cattani, P. Zaffino, R. Ricotti, M. F. Spadea, *et al.*, "Atlas-based segmentation in breast cancer radiotherapy: evaluation of specific and generic-purpose atlases," *The Breast*, vol. 32, pp. 44–52, 2017.

[159] N. Johnston, J. De Rycke, Y. Lievens, M. Van Eijkeren, J. Aelterman, E. Vandersmissen, S. Ponte, and B. Vanderstraeten, "Dose-volume-based evaluation of convolutional neural network-based auto-segmentation of thoracic organs at risk," *Physics and imaging in radiation oncology*, vol. 23, pp. 109–117, 2022.

[160] S. Arculeo, E. Miglietta, F. Nava, A. Morra, M. C. Leonardi, S. Comi, D. Ciardo, M. S. Fiore, M. A. Gerardi, M. Pepa, *et al.*, "The emerging role of radiation therapists in the contouring of organs at risk in radiotherapy: analysis of inter-observer variability with radiation oncologists for the chest and upper abdomen," *ecancermedicalscience*, vol. 14, 2020.

[161] S. K. Vinod, M. Min, M. G. Jameson, and L. C. Holloway, "A review of interventions to reduce inter-observer variability in volume delineation in radiation oncology," *Journal of medical imaging and radiation oncology*, vol. 60, no. 3, pp. 393–406, 2016.

[162] D. P. Huttenlocher, G. A. Klanderman, and W. J. Rucklidge, "Comparing images using the hausdorff distance," *IEEE Transactions on pattern analysis and machine intelligence*, vol. 15, no. 9, pp. 850–863, 1993.

[163] S. J. Gardner, N. Wen, J. Kim, C. Liu, D. Pradhan, I. Aref, R. Cattaneo, S. Vance, B. Movsas, I. J. Chetty, *et al.*, "Contouring variability of human-and deformable-generated contours in radiotherapy for prostate cancer," *Physics in Medicine & Biology*, vol. 60, no. 11, p. 4429, 2015.

[164] G. F. Persson, D. E. Nygaard, C. Hollensen, P. Munck af Rosenschöld, L. S. Mouritsen, A. K. Due, A. K. Berthelsen, J. Nyman, E. Markova, A. P. Roed, *et al.*, "Interobserver delineation variation in lung tumour stereotactic body radiotherapy," *The British journal of radiology*, vol. 85, no. 1017, pp. e654–e660, 2012.

[165] M. Thomas, H. R. Mortensen, L. Hoffmann, D. S. Møller, E. G. Troost, C. T. Muijs, M. Berbee, R. Bütof, O. Nicholas, G. Radhakrishna, *et al.*, "Proposal for the delineation of neoadjuvant target volumes in oesophageal cancer," *Radiotherapy and Oncology*, vol. 156, pp. 102–112, 2021.

[166] R. W. Underberg, F. J. Lagerwaard, B. J. Slotman, J. P. Cuijpers, and S. Senan, "Use of maximum intensity projections (mip) for target volume generation in 4dct scans for lung cancer," *International Journal of Radiation Oncology* Biology* Physics*, vol. 63, no. 1, pp. 253–260, 2005.

[167] R. Protection, "Icrp publication 103," *Ann ICRP*, vol. 37, no. 2.4, p. 2, 2007.

[168] J. Zhu, J. Zhang, B. Qiu, Y. Liu, X. Liu, and L. Chen, "Comparison of the automatic segmentation of multiple organs at risk in ct images of lung cancer between deep convolutional neural network-based and atlas-based techniques," *Acta Oncologica*, vol. 58, no. 2, pp. 257–264, 2019.

[169] X. Dong, Y. Lei, T. Wang, M. Thomas, L. Tang, W. J. Curran, T. Liu, and X. Yang, "Automatic multiorgan segmentation in thorax ct images using u-net-gan," *Medical physics*, vol. 46, no. 5, pp. 2157–2168, 2019.

[170] Y. Tsang, P. Hoskin, E. Spezi, D. Landau, J. Lester, E. Miles, and J. Conibear, "Assessment of contour variability in target volumes and organs at risk in lung cancer radiotherapy," *Technical Innovations & Patient Support in Radiation Oncology*, vol. 10, pp. 8–12, 2019.

[171] H. H. Barrett, J. Yao, J. P. Rolland, and K. J. Myers, "Model observers for assessment of image quality.," *Proceedings of the National Academy of Sciences*, vol. 90, no. 21, pp. 9758–9765, 1993.

[172] B. De Man, J. Nuyts, P. Dupont, G. Marchal, and P. Suetens, "An iterative maximum-likelihood polychromatic algorithm for ct," *IEEE transactions on medical imaging*, vol. 20, no. 10, pp. 999–1008, 2001.

[173] Z. Tian, X. Jia, K. Yuan, T. Pan, and S. B. Jiang, "Low-dose ct reconstruction via edge-preserving total variation regularization," *Physics in Medicine & Biology*, vol. 56, no. 18, p. 5949, 2011.

[174] L. L. Geyer, U. J. Schoepf, F. G. Meinel, J. W. Nance Jr, G. Bastarrika, J. A. Leipsic, N. S. Paul, M. Rengo, A. Laghi, and C. N. De Cecco, "State of the art: iterative ct reconstruction techniques," *Radiology*, vol. 276, no. 2, pp. 339–357, 2015.

[175] M. Beister, D. Kolditz, and W. A. Kalender, "Iterative reconstruction methods in x-ray ct," *Physica medica*, vol. 28, no. 2, pp. 94–108, 2012.

[176] E. Y. Sidky, C.-M. Kao, and X. Pan, "Accurate image reconstruction from few-views and limited-angle data in divergent-beam ct," *Journal of X-ray Science and Technology*, vol. 14, no. 2, pp. 119–139, 2006.

[177] E. Y. Sidky and X. Pan, "Image reconstruction in circular cone-beam computed tomography by constrained, total-variation minimization," *Physics in Medicine & Biology*, vol. 53, no. 17, p. 4777, 2008.

[178] J. Wang, H. Lu, T. Li, and Z. Liang, "Sinogram noise reduction for low-dose ct by statistics-based nonlinear filters," in *Medical Imaging 2005: Image Processing*, vol. 5747, pp. 2058–2066, SPIE, 2005.

[179] P. F. Feruglio, C. Vinegoni, J. Gros, A. Sbarbati, and R. Weissleder, "Block matching 3d random noise filtering for absorption optical projection tomography," *Physics in Medicine & Biology*, vol. 55, no. 18, p. 5401, 2010.

[180] H. Chen, Y. Zhang, W. Zhang, P. Liao, K. Li, J. Zhou, and G. Wang, "Low-dose ct via convolutional neural network," *Biomedical optics express*, vol. 8, no. 2, pp. 679–694, 2017.

[181] H. Chen, Y. Zhang, M. K. Kalra, F. Lin, Y. Chen, P. Liao, J. Zhou, and G. Wang, "Low-dose ct with a residual encoder-decoder convolutional neural network," *IEEE transactions on medical imaging*, vol. 36, no. 12, pp. 2524–2535, 2017.

[182] J. M. Wolterink, T. Leiner, M. A. Viergever, and I. Išgum, "Generative adversarial networks for noise reduction in low-dose ct," *IEEE transactions on medical imaging*, vol. 36, no. 12, pp. 2536–2545, 2017.

[183] E. Kang, W. Chang, J. Yoo, and J. C. Ye, "Deep convolutional framelet denosing for low-dose ct via wavelet residual network," *IEEE transactions on medical imaging*, vol. 37, no. 6, pp. 1358–1369, 2018.

[184] C. Tang, J. Li, L. Wang, Z. Li, L. Jiang, A. Cai, W. Zhang, N. Liang, L. Li, and B. Yan, "Unpaired low-dose ct denoising network based on cycle-consistent generative adversarial network with prior image information," *Computational and mathematical methods in medicine*, vol. 2019, 2019.

[185] J. Lehtinen, J. Munkberg, J. Hasselgren, S. Laine, T. Karras, M. Aittala, and T. Aila, "Noise2noise: Learning image restoration without clean data," *arXiv preprint arXiv:1803.04189*, 2018.

[186] N. Yuan, J. Zhou, and J. Qi, "Low-dose ct image denoising without high-dose reference images," in *15th International Meeting on Fully Three-Dimensional Image Reconstruction in Radiology and Nuclear Medicine*, vol. 11072, pp. 224–228, SPIE, 2019.

[187] A. Krull, T.-O. Buchholz, and F. Jug, "Noise2void-learning denoising from single noisy images," in *Proceedings of the IEEE/CVF conference on computer vision and pattern recognition*, pp. 2129–2137, 2019.

[188] Z. Zhang, Q. Liu, and Y. Wang, "Road extraction by deep residual u-net," *IEEE Geoscience and Remote Sensing Letters*, vol. 15, no. 5, pp. 749–753, 2018.

[189] F. I. Diakogiannis, F. Waldner, P. Caccetta, and C. Wu, "Resunet-a: A deep learning framework for semantic segmentation of remotely sensed data," *ISPRS Journal of Photogrammetry and Remote Sensing*, vol. 162, pp. 94–114, 2020.

[190] O. Ronneberger, P. Fischer, and T. Brox, "U-net: Convolutional networks for biomedical image segmentation," in *International Conference on Medical image computing and computer-assisted intervention*, pp. 234–241, Springer, 2015.

[191] K. He, X. Zhang, S. Ren, and J. Sun, "Deep residual learning for image recognition," in *Proceedings of the IEEE conference on computer vision and pattern recognition*, pp. 770–778, 2016.

[192] S. Ioffe and C. Szegedy, "Batch normalization: Accelerating deep network training by reducing internal covariate shift," in *International conference on machine learning*, pp. 448–456, PMLR, 2015.

[193] K. He, X. Zhang, S. Ren, and J. Sun, "Delving deep into rectifiers: Surpassing human-level performance on imagenet classification," in *Proceedings of the IEEE international conference on computer vision*, pp. 1026–1034, 2015.

[194] V. Dumoulin and F. Visin, "A guide to convolution arithmetic for deep learning," *arXiv preprint arXiv:1603.07285*, 2016.

[195] Z. Wang, A. C. Bovik, H. R. Sheikh, and E. P. Simoncelli, "Image quality assessment: from error visibility to structural similarity," *IEEE transactions on image processing*, vol. 13, no. 4, pp. 600–612, 2004.

[196] B. Kim, M. Han, H. Shim, and J. Baek, "A performance comparison of convolutional neural network-based image denoising methods: The effect of loss functions on low-dose ct images," *Medical physics*, vol. 46, no. 9, pp. 3906–3923, 2019.

[197] Q. Yang, P. Yan, Y. Zhang, H. Yu, Y. Shi, X. Mou, M. K. Kalra, Y. Zhang, L. Sun, and G. Wang, "Low-dose ct image denoising using a generative adversarial network with wasserstein distance and perceptual loss," *IEEE transactions on medical imaging*, vol. 37, no. 6, pp. 1348–1357, 2018.

[198] M. Gholizadeh-Ansari, J. Alirezaie, and P. Babyn, "Deep learning for low-dose ct denoising using perceptual loss and edge detection layer," *Journal of digital imaging*, vol. 33, no. 2, pp. 504–515, 2020.

[199] C. Ledig, L. Theis, F. Huszár, J. Caballero, A. Cunningham, A. Acosta, A. Aitken, A. Tejani, J. Totz, Z. Wang, *et al.*, "Photo-realistic single image super-resolution using a generative adversarial network," in *Proceedings of the IEEE conference on computer vision and pattern recognition*, pp. 4681–4690, 2017.

[200] C. You, Q. Yang, H. Shan, L. Gjesteby, G. Li, S. Ju, Z. Zhang, Z. Zhao, Y. Zhang, W. Cong, *et al.*, "Structurally-sensitive multi-scale deep neural network for low-dose ct denoising," *Ieee Access*, vol. 6, pp. 41839–41855, 2018.

[201] M. Han, H. Shim, and J. Baek, "Low-dose ct denoising via convolutional neural network with an observer loss function," *Medical physics*, vol. 48, no. 10, pp. 5727–5742, 2021.

[202] D. P. Kingma and J. Ba, "Adam: A method for stochastic optimization," *arXiv preprint arXiv:1412.6980*, 2014.

[203] F. Wilcoxon, "Individual comparisons by ranking methods," *Biometrics Bulletin*, vol. 1, p. 80, Dec. 1945.

[204] K. Kamnitsas, C. Ledig, V. F. Newcombe, J. P. Simpson, A. D. Kane, D. K. Menon, D. Rueckert, and B. Glocker, "Efficient multi-scale 3d cnn with fully connected crf for accurate brain lesion segmentation," *Medical image analysis*, vol. 36, pp. 61–78, 2017.

[205] S. Willems, J. Bertels, W. Crijns, E. Sterpin, K. Haustermans, and F. Maes, "Convolutional neural networks for dose prediction in radiotherapy: from segmentation to regression," *Technical Report: KUL/ESAT/PSI/2201*, 2022.

[206] J. W. Stayman, H. Dang, Y. Ding, and J. H. Siewerdsen, "Pirple: a penalized-likelihood framework for incorporation of prior images in ct reconstruction," *Physics in Medicine & Biology*, vol. 58, no. 21, p. 7563, 2013.

[207] H. Zhang, H. Han, Z. Liang, Y. Hu, Y. Liu, W. Moore, J. Ma, and H. Lu, "Extracting information from previous full-dose ct scan for knowledge-based bayesian reconstruction of current low-dose ct images," *IEEE transactions on medical imaging*, vol. 35, no. 3, pp. 860–870, 2015.

[208] Z. Huang, X. Liu, R. Wang, Z. Chen, Y. Yang, X. Liu, H. Zheng, D. Liang, and Z. Hu, "Learning a deep cnn denoising approach using anatomical prior information implemented with attention mechanism for low-dose ct imaging on clinical patient data from multiple anatomical sites," *IEEE Journal of Biomedical and Health Informatics*, vol. 25, no. 9, pp. 3416–3427, 2021.

A

Appendix: Supplementary materials for chapter 4

In chapter 4, an anthropomorphic head phantom and three patient cases were employed to evaluate the effect of reducing CT imaging dose on proton therapy dose calculation where the results were presented only for case 3. This section represents the results of three other cases. The effect of CT noise on proton therapy dose calculation and plan optimization are presented in Figures A1 and A2, respectively. The DVHs based on the LdCTs are well aligned with those of the standard dose CT. Figure A3 illustrates the energy layers (X axis) and the relative weights (Y axis) for plans optimized on the LdCT and the reference-dose CT. Figure A4 compares the WET maps estimated based on the LdCT with those of the standard-dose CT.

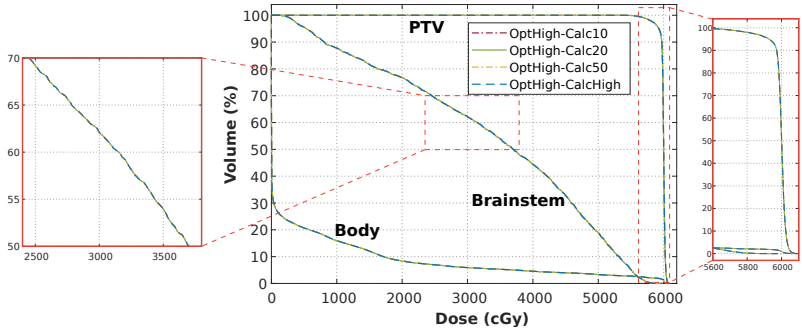

Case 1: Head Phantom

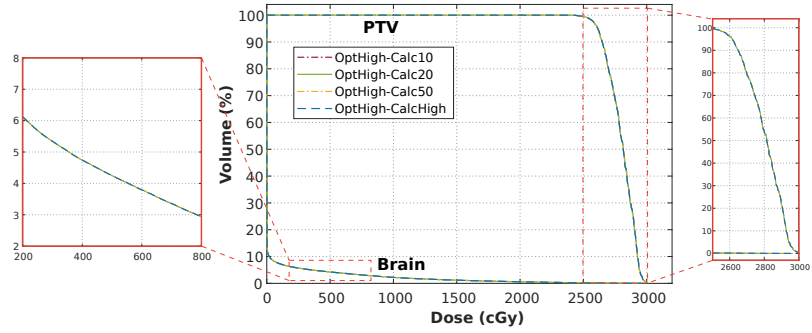

Case 2: Brain Metastasis

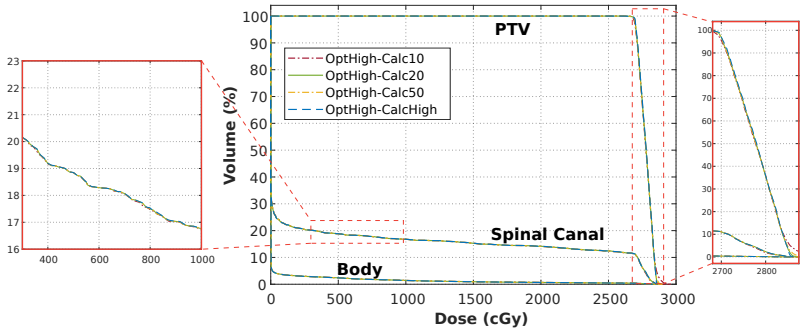

Case 4: Vertebral Metastases

Figure A1: Comparison of the DVHs for organs at risk and the target volume acquired from the standard and LDCTs showing the effect of CT dose reduction on dose calculation (OptHigh-CalcLow VS OptHigh-CalcHigh). Using LDCTs for dose calculation resulted in DVHs similar to the ground truth.

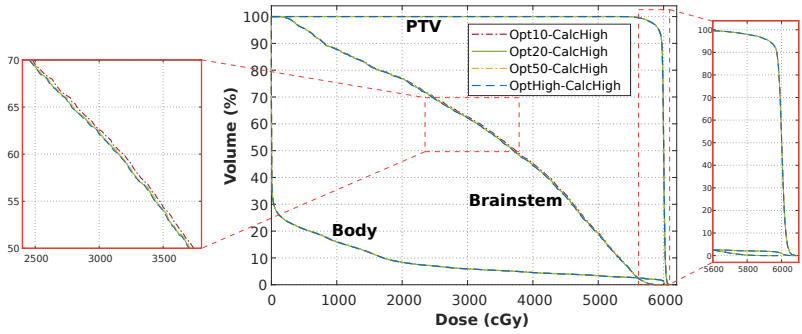

Case 1: Head Phantom

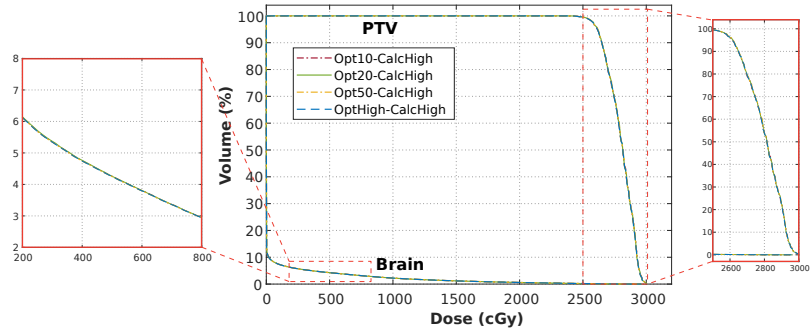

Case 2: Brain Metastasis

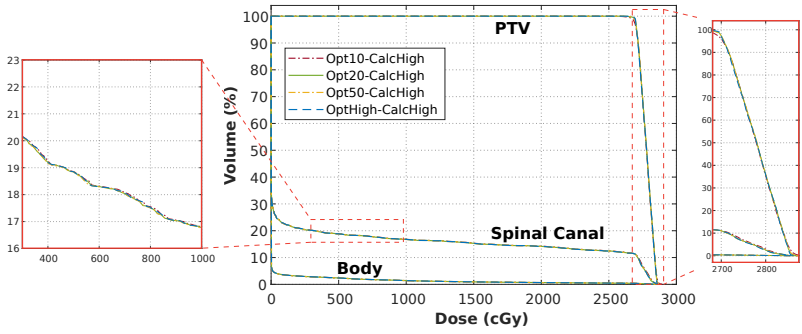

Case 4: Vertebral Metastases

Figure A2: Comparison of the DVHs for OARs and the target volume acquired from the standard and LDCTs showing the effect of CT dose reduction on plan optimization (OptLow-CalcHigh VS OptHigh-CalcHigh). Using LDCTs for plan optimization resulted in DVHs similar to the ground truth.

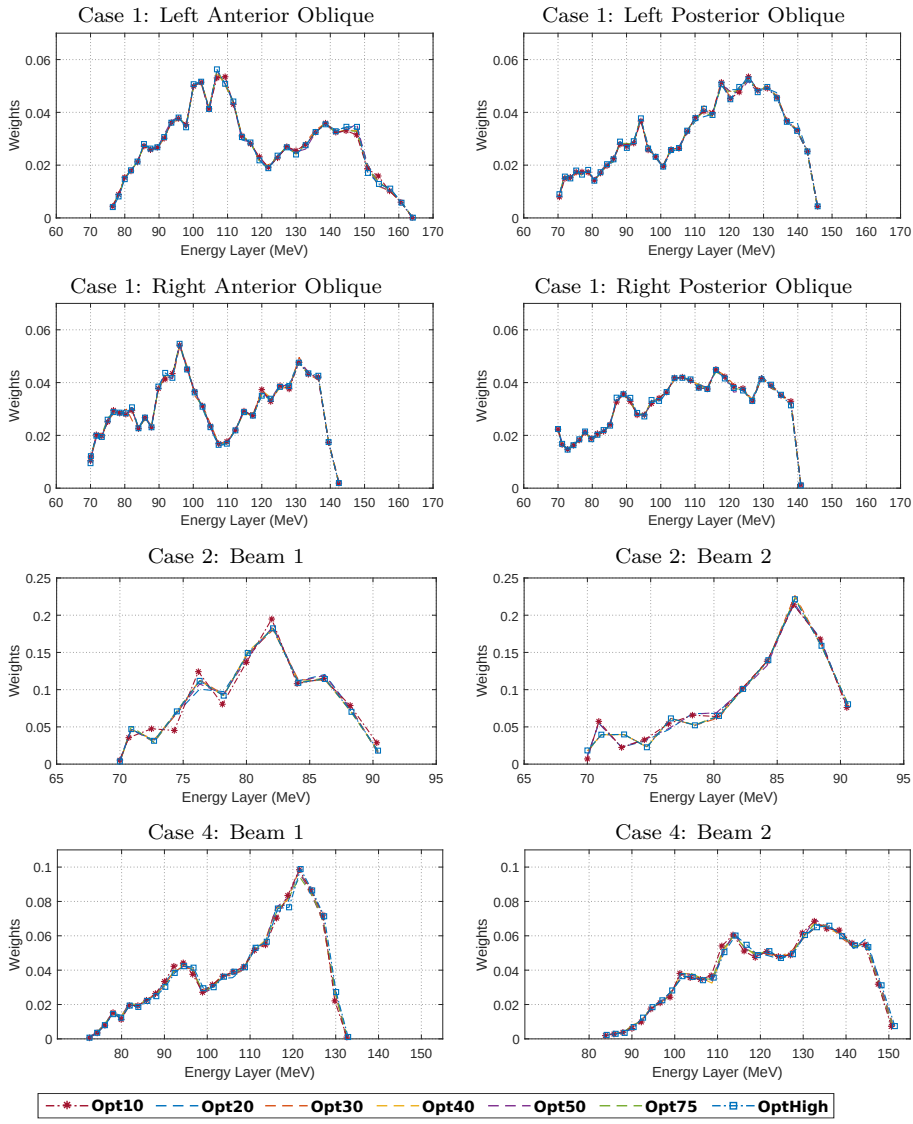

Figure A3: Representation of the energy layers and the corresponding relative weights. The plans are reoptimized on the standard-dose and LDCTs separately.

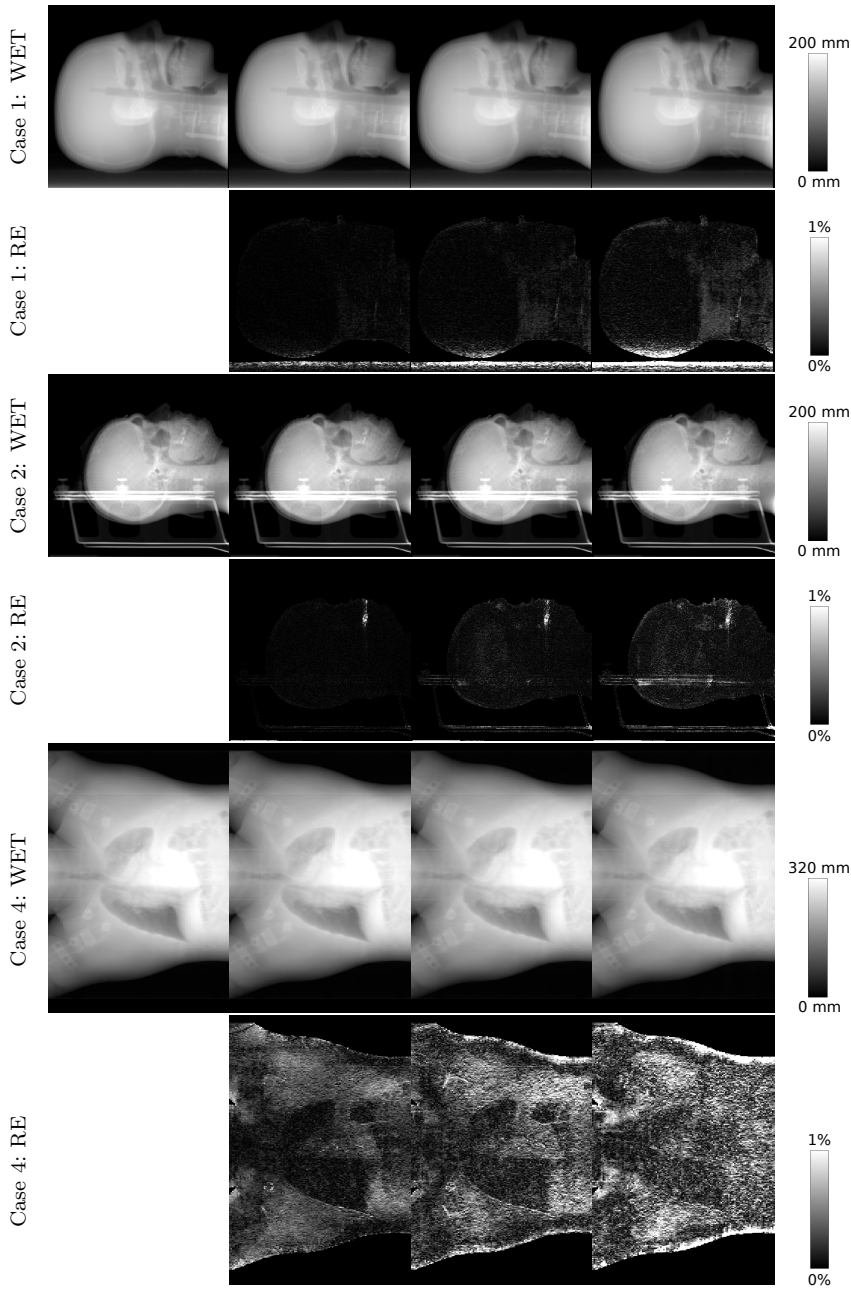

Figure A4: Representation of (first, third, and fifth rows) the WET maps calculated from the standard-dose and LDCTs and (second, forth, and sixth rows) the corresponding relative error (RE).

B

Appendix: Calibration of LdCT simulator

It is crucial to calibrate the LdCT simulator (Chapter 3) for each scanner, for example, to estimate the equivalent number of photons to represent the incident X-ray intensity, the correlation between detector pixels, the threshold to apply the SDF, etc. The general procedure for calibrating the LdCT simulator is described in this section.

First of all, it should be noted that the CT scanners used in this study were equipped with energy-integrating detectors, not photon-counting detectors. However, photon-counting models are good approximations of quantum noise in CT scanners with energy-integrating detectors and have been widely used for CT noise modeling (as discussed in Section 3.2.1). The general idea is to convert the measured energies to their equivalent number of photons and then consider the system as a photon-counting CT. For example, the incident X-ray intensities are represented as an equivalent number of photons despite the fact that energy-integrating systems were used in this study. Here "equivalent" implies that the Poisson noise on that photon number equals the quantum noise on the X-ray measurement.

Each experiment begins with performing several blank scans (without any attenuating object in the field of view) using different tube loads. These blank scans will be used to estimate the equivalent number of photons as a function of the incident X-ray intensity and also the crosstalk (correlation) between detector elements.

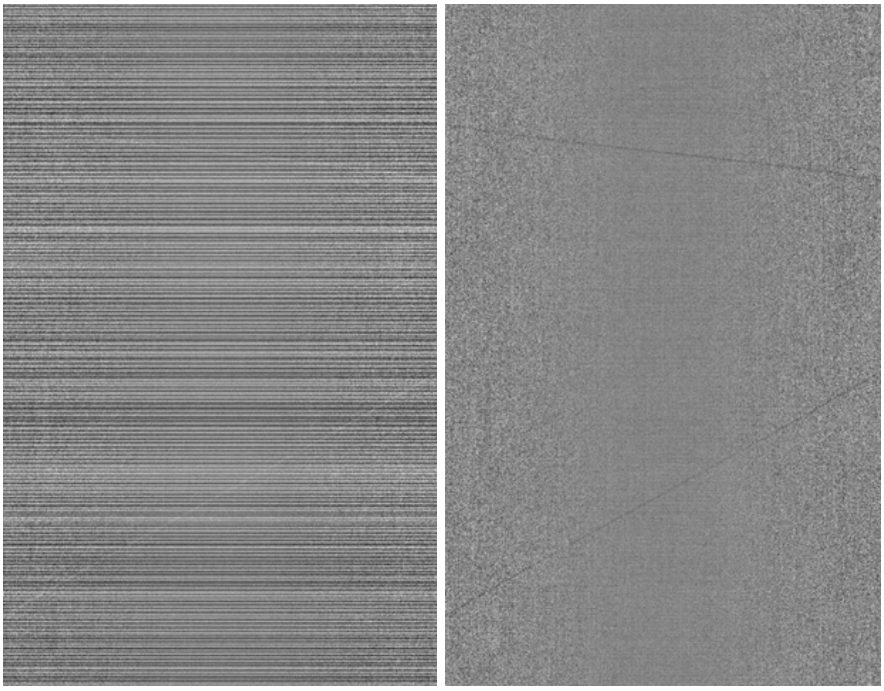

Figure B1: Representation of $\exp(-\rho)$ for one of the detector rows before (left) and after (right) normalization. Here ρ represents the log converted data.

After the acquisition of the blank scans, it is crucial to normalize them to make sure that the mean value of the transmitted signal is the same for every detector row. The need for this normalization is due to an arbitrary offset that was observed in the detector pixels. The calculation of the variance of transmission data in the blank scans can be severely affected by this offset. However, this offset does not have any impact on the reconstruction. In this study, the blank scans were normalized by dividing all the measurements ($\exp(-\rho)$) in one detector row by a constant value to make sure that the mean value of the $\exp(-\rho)$ is equal to one for that detector row (here ρ represents the log converted data). This normalization results in a smaller variance on $\exp(-\rho)$ and therefore in a larger equivalent number of photons for a unit tube load ($I_0^{(1)}$). Figure B1 illustrates $\exp(-\rho)$ of a blank scan before and after normalization.

Assuming that the transmitted signals at different views are independent noise realizations, the variance of the transmitted signal can be computed from all views for each detector element (there are usually more than 1000 views

Figure B2: The variance of the transmitted signals in every detector element for the Force scanner.

per rotation). If flying focal spot is used, the variance should be computed independently for each position of that flying focal spot. Figure B2 illustrates the variance of the transmitted signal for a black scan (tube load = 20 mAs). The lower variance in the center of the detector is due to the bowtie filter. The number of photons for a unit tube load ($I_0^{(1)}$) and the variance of the electronic noise (σ_e^2) can then be estimated by Equation 3.9.

The crosstalk between detector elements can be estimated by calculating the correlation between noise in neighboring detector elements from a large number of locations. The correlation matrix (r) for the FORCE scanner is shown in Figure B3(a) where the yellow square shows the central element. As explained in section 3.2.4, the convolution mask w should satisfy Equation 3.17 ($[w \otimes w]_{i-j} = r_{ij}$). The convolution can be written as the multiplication of two circulant matrices. To do this, the convolution masks r and w were first converted to circulant matrices R and W. Therefore, the convolution of the mask w with itself corresponds to the multiplication of the matrix W with itself. Matrix W can then be computed as the square root of the circulant matrix R. Finally, the mask w can be extracted from W.

The square root of a scalar A can be calculated using an iterative approach as follows:

$$x^{(n+1)} = x^{(n)} + \frac{A - x^2}{2x} \quad \text{with} \quad x^{(0)} > 0 \tag{B.1}$$

where x represents the square root of A and the superscript (n) denotes the iteration number. The matrix equivalent of this equation can be written as:

$$W^{(n+1)} = W^{(n)} + \frac{1}{2}\left(R - W^{(n)}W^{(n)}\right)\left(W^{(n)}\right)^{-1} \quad \text{with} \quad W^{(0)} \text{ invertible.} \tag{B.2}$$

Here R and W represent the circulant matrices acquired from r and w. The coefficients of w are the values along a single row in W. Figure B3(b) shows the estimated correlation mask w. Convolving the thinning noise with the correlation mask w can be seen as computing weighted averages of the noise over neighboring pixels to introduce the correlation between them. Averaging usually smooths the signal, consequently, the variance of the thinning noise is expected to be lower after applying the correlation mask. The sum of the

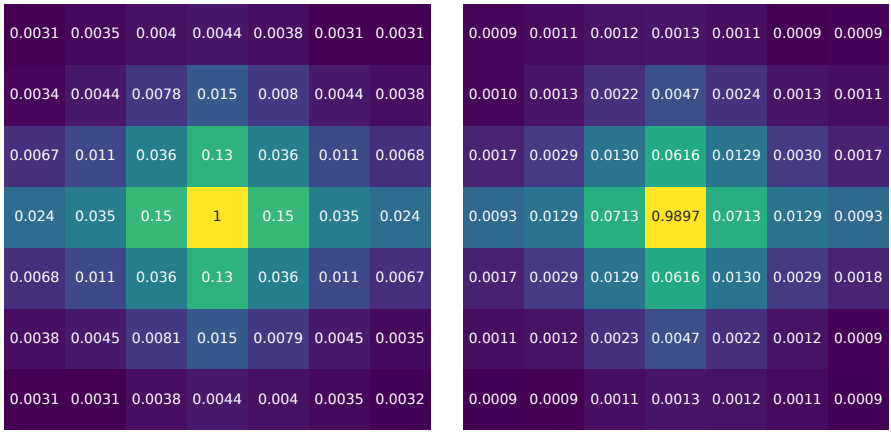

(a) Correlation matrix r (b) Convolution mask w

Figure B3: Illustration of the correlation matrix (r) and the estimated correlation mask (w) for the FORCE scanner.

weights in the convolution mask should therefore be larger than 1 to maintain the same noise variance after applying the convolution mask.

As discussed in Chapter 3, modern CT scanners usually smooth the transmitted signals if the number of detected photons (or measured energy in energy-integrating CTs) is below a specific threshold (T). The so-called signal dependent filter (SDF) aims to keep the SNR at a fixed level when the detected signal is smaller than T. The SDF smooths the transmitted signal using local information. In the presence of the SDF, the correlation between neighboring detector elements is expected to increase when the number of detected photons is smaller than the threshold T.

To determine the threshold T, a uniform cylinder, such as a water phantom, with sufficient attenuation should be scanned. The phantom needs to be circularly symmetrical since the same projections in every view are required to analyze the correlations, by looking at a particular pixel and its neighbors over all views. In addition, it is crucial to place the phantom in the center of the scanner to ensure that the observed correlation is only due to (smoothed) noise correlations, and not due to the data correlations. The smoothing threshold can be obtained by analyzing the correlation between detector elements for different equivalent photon numbers. To this end, the equivalent number of photons and the corresponding correlation between neighboring detector elements should be calculated for several locations. The blue curve in Figure B4 represents the correlation between neighboring detector elements as a function of the equivalent number of photons. It can

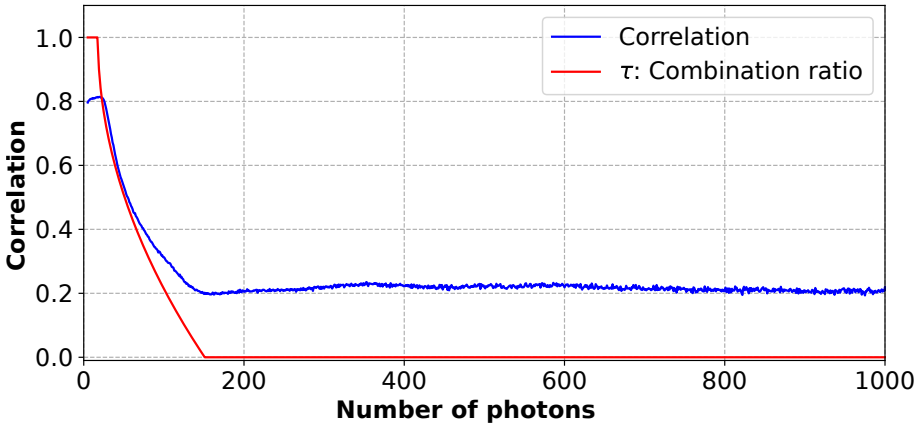

Figure B4: The representation of the correlation between neighboring detector elements (blue curve) and the predicted value for the combination coefficient τ (red curve) as a function of the number of photons.

be seen that the correlation increases abruptly when the equivalent number of photons is lower than 160 photons. The combination ratio τ can be calculated by combining Equation 3.19 and 3.21. The red curve in Figure B4 shows the theoretical value of τ as a function of the equivalent number of photons.

In order to estimate the beam hardening scaling factor, the knowledge of low-energy filters, the width of bowtie filter, and the energy spectrum[1] are required. For the FORCE scanner, the low-energy filter consists of 3 mm of Aluminium plus 1.2 mm of Titanium. In addition, the bowtie filter is made of Teflon (CF–2 with a density of 2.225 g/cm3). This information is usually provided by vendors and can be used to estimate the spectrum of the incident X-ray intensity. The scaling factor can then be estimated as discussed in Section 3.2.5.

After estimating the required parameters, LdCTs can be simulated as described in Algorithm 1. The LdCT simulator can be evaluated by comparing the noise in the simulated and measured LdCTs, preferably in both the image and sinogram domains. It is recommended to perform several water phantom studies to evaluate the accuracy of the LdCT simulator for different acquisition protocols. In order to see the effect of SDF, a phantom with enough attenuation should be used and the tube load should be reduced dramatically to make sure that at least along the lines with maximum attenuation, the number of detected photons is smaller than the threshold T.

Image reconstruction can be performed in several ways. In the early

[1]The energy spectrum for Siemens CT scanners (Tungsten, 30-140 kV) can be found at: `https://bps.healthcare.siemens-healthineers.com/booneweb/index.html`

stages, in-house image reconstruction was employed. Later on, the simulated scans were imported into the scanner and then reconstructed with the scanner's software to increase the clinical relevance of the study. Converting the simulated scan to the appropriate format (.ptr for Siemens scanners) was performed with a script that was provided by the vendor. Finally, Siemens offline reconstruction software, ReconCT[2] Version 14.2, was employed for image reconstruction. ReconCT produces images that are of the same quality as clinical images but can only be used for research purposes. It should be noted that ReconCT also offers LdCT simulation which may be useful for optimizing image acquisition protocols.

The LdCT simulator was successfully calibrated for Siemens SOMATOM FORCE, DRIVE, and Definition EDGE scanners at the radiation oncology and radiology departments of the University Hospital of Leuven in Belgium.

[2]Detailed information about ReconCT can be found at `https://ipipe.azurewebsites.net/prototypes/ReconCT`.

Scientific acknowledgments, personal contribution, conflicts of interest, and ethical statement

Scientific acknowledgments

Scientific acknowledgments are stated in each chapter.

Personal contribution

I hereby assert that the personal contributions to this thesis included but were not limited to:

- Definition, conceptualization, and design;
- Data acquisition;
- Implementation and calibration of the LdCT simulator is Chapter 3;
- Implementation of the frameworks in Chapter 4 and 5;
- Implementation and training of the CNN-based CT denoiser in Chapter 6;
- Writing of the papers included in this thesis and the remaining chapters.

Conflicts of interest

This project is funded by Fonds Baillet Latour. Gilles Defraene is postdoctoral fellow of the Research Foundation Flanders (FWO, project 1292021). Siri Willems is supported by a PhD fellowship of the Research Foundation Flanders (FWO). There are no other conflicts of interest.

Ethical statement

The ethics committee research of University Hospital Leuven (UZ Leuven) has approved the research (Reference Number: S66614, S65639, and S59667).

The research was conducted in accordance with the principles embodied in the Declaration of Helsinki and in accordance with local statutory requirements. All participants (or their parent or legal guardian in the case of children under 16) gave written informed consent to participate in the study.

List of Publications

Peer-Reviewed Journal Papers

- **M. Elhamiasl**, P. Populaire, D. Callens, V. Badiu, G. Defraene, M. Lambrecht, X. Geets, E. Sterpin, and J. Nuyts. "Low-dose 4DCT for proton therapy treatment planning of esophageal and lung cancer patients", In-preparation.

- **M. Elhamiasl**, G. Defraene, M. Lambrecht, X. Geets, E. Sterpin, and J. Nuyts. "Suppressing the (already small) effects of CT dose reduction with a convolutional neural network for different tasks in proton therapy", In-preparation.

- **M. Elhamiasl**, K. Salvo, K. Poels, G. Defraene, M. Lambrecht, X. Geets, E. Sterpin, and J. Nuyts. "Low-dose CT allows for accurate proton therapy dose calculation and plan optimization", Physics in Medicine & Biology, vol. 67, no. 19, p. 195015, 2022. https://doi.org/10.1088/1361-6560/ac8dde

- **M. Elhamiasl** and J. Nuyts. "Low-dose x-ray CT simulation from an available higher-dose scan", Physics in Medicine & Biology, vol. 65, no. 13, p. 135010, Jul. 2020. https://doi.org/10.1088/1361-6560/ab8953

Peer-Reviewed Conference Proceedings

- **M. Elhamiasl**, S. Willems, G. Schramm, G. Defraene, M. Lambrecht, X. Geets, E. Sterpin, and J. Nuyts. "The effect of reducing CT dose on delineation of organs at risk in proton therapy", IEEE Nuclear Science Symposium and Medical Imaging Conference (NSS/MIC), 2022.

- **M. Elhamiasl**, K. Salvo, E. Sterpin, and J. Nuyts. "The effect of CT dose reduction on proton therapy dose calculation and plan optimization: A phantom study", IEEE Nuclear Science Symposium and Medical Imaging Conference (NSS/MIC), 2021. https://doi.org/10.1109/NSS/MIC44867.2021.9875714

- **M. Elhamiasl**, S. Teruel Rivas, K. Salvo, E. Sterpin, and J. Nuyts. "The effect of CT dose reduction on proton therapy dose calculation", 6th International Conference on Image Formation in X-Ray Computed Tomography (CT Meeting), 2020.

- **M. Elhamiasl**, K. Salvo, W. Coudyzer, and J. Nuyts. "Low-dose CT simulation from an available higher dose CT scan," IEEE Nuclear Science Symposium and Medical Imaging Conference (NSS/MIC) (pp. 1-3). 2019. https://doi.org/10.1109/nss/mic42101.2019.9059917

- **M. Elhamiasl** and J. Nuyts. "Simulating lower-dose scans from an available CT scan," 15th International Meeting on Fully Three-Dimensional Image Reconstruction in Radiology and Nuclear Medicine, 2019. https://doi.org/10.1117/12.2534746

Peer-Reviewed Conference Abstracts

- **M. Elhamiasl**, G. Defraene, K. Salvo, E. Sterpin, and J. Nuyts. "Low dose CT allows for accurate proton dose calculation in esophageal cancer", in 2022 European Society for Radiotherapy and Oncology (ESTRO) Annual Meeting, 2022.

- **M. Elhamiasl**, K. Salvo, E. Sterpin, and J. Nuyts. "The effect of reducing CT dose on proton therapy dose calculation - phantom study, in 2021 European Society for Radiotherapy and Oncology (ESTRO) Annual Meeting, 2021.

- **M. Elhamiasl** and J. Nuyts. "Simulating lower-dose scans from an available high dose CT scan," Belgian Molecular Imaging Congress, 2019.

MASOUD ELHAMIASL

BIOMEDICAL ENGINEER
PROTON THERAPY | AI | CT

masoud.elhamiasl@kuleuven.be | @masoudelhamiasl | Leuven, Belgium

PROFILE

My research focuses on low-dose CT simulation, proton therapy, and CT denoising. I have 2+ years' experience in the medical device industry. My greatest passion in life is using my technical know-how to improve the patient's quality of life.

WORK EXPERIENCE

PhD Researcher
KU Leuven, Belgium
Sep 2017 - Apr 2023

- Low-dose CT simulation and reconstruction
- Low-dose CT for accurate proton dose estimation
- CNN-based low-dose CT image denoising

Visiting Researcher
NTNU, Norway
Jan 2017 - Aug 2017

- Dermoscopy image analysis
- Deep vs handcrafted features
- Radiomics in medical imaging

R&D Researcher
Saadat Co., Iran
Sep 2014 - Dec 2016

- Design and fabrication of a Tele-electrocardiograph
- ECG signal processing and Interpretation
- Medical device risk analysis

EDUCATION HISTORY

KU Leuven | PhD in Biomedical Sciences
Sep 2017 - April 2023
Thesis: Low-Dose CT Protocols for Accurate Proton Therapy Treatment Planning.

Tarbiat Modares University | M.Sc. in Biomedical Engineering
Sep 2012 – Jan 2015
Thesis: Blood Vessel Tracking using Gaussian Process and Radon Transform.

Sahand University of Technology | B.Sc. in Biomedical Engineering
Jan 2008 – Jan 2012
Final project: Design and Fabrication a Syringe Pump using AVR Microcontroller.

TEACHING AND SUPERVISION EXPERIENCE

Teacher Assistant

- Biomedical Image Processing, assistant for Dr. Sebelan Danishvar, University of Tabriz [2015].

Supervision Experience

- Master thesis supervision on CT denoising using deep residual U-Net architecture [2021].
- Master thesis supervision on joint tracking and bifurcation detection in retinal images [2015].
- Master thesis supervision on 3D lumen segmentation using Gaussian process [2015].

SELECTED PUBLICATIONS

Peer-reviewed Journal Articles

- Low-dose CT allows for accurate proton therapy dose calculation and plan optimization [PMB, 2022]
- Low-dose X-ray CT simulation from an available higher-dose scan [PMB, 2020].
- Tracking and diameter estimation of retinal vessels using Gaussian process and Radon transform [JMI, 2017].

Selected Conference Proceedings/Abstracts

- The Effect of Reducing CT Dose on Delineation of Organs at Risk in Proton Therapy [MIC, 2022].
- Low-dose CT allows for accurate proton dose calculation in esophageal cancer [ESTRO, 2022].
- The effect of reducing CT dose on proton therapy dose calculation - phantom study [ESTRO, 2021].
- The effect of CT dose reduction on proton therapy dose calculation [CTmeeting, 2020].
- Low-dose CT simulation from an available CT scan [MIC, 2019].
- Simulating lower-dose scans from an available CT scan [Fully3D, 2019].

INVITED TALKS

- Low-dose CT protocols for proton therapy treatment planning [Maastro Clinic, 2023].

RELEVANT TRAINING AND SUMMER SCHOOLS

- Real-world implementation of adaptive radiotherapy in clinical practice [2022].
- Exploitation of Research: Acoustic markers for enhanced remote sensing of radiation doses [2022].
- Technology and techniques in nuclear medicine [2021].
- Medical image reconstruction using deep learning [2021].
- RayStation proton/carbon treatment planning training [2020].
- ESTRO course on particle therapy [2020].
- Synergistic reconstruction symposium [2019].
- ATTIRE2019: Algorithms and theory in tomographic image reconstruction [2019].
- Medical image reconstruction: from foundations to AI [2019].
- Advanced reconstruction methods in tomography [2018].
- Advanced computed tomography imaging technologies [2018].
- Deep learning, University of Deusto and Rovira i Virgili University [2017].
- BIOMAT: Mathematical models in biomedical imaging, University of Granada [2017].

MY AWARD

- IEEE NSS/MIC Trainee Grant [2022].
- IEEE NSS/MIC Trainee Grant [2021].
- IEEE NSS/MIC Trainee Grant [2019].
- Fonds Baillet Latour PhD scholarship to conduct medical research in Belgium [2017].
- The Research Council of Norway Research Fellowship Grant [2017].
- Ranked 1st among graduate students of Biomedical Engineering [2015].
- Best Paper Award, 17th Iranian Student Conference on Electrical Engineering [2014].
- Best Paper Award, 2nd Computer Science Conference on Computer and Information Technology [2014].
- Honor Student Awards, Tarbiat Modares University [2014].
- Honor Student Awards, Sahand University of Technology [2014].
- Ranked 1st in Harkat Festival, Student Journals Section, Editorial Board of the Bioelectric Journal [2009].

INTEREST

- In my free time, I enjoy running, playing football, solving puzzles, travelling, and photography.

KU LEUVEN